



**UNIVERSIDAD NACIONAL AUTÓNOMA DE MÉXICO
POSGRADO EN CIENCIAS FÍSICAS**

**OPTICAL RESPONSE OF PARTIALLY EMBEDDED
NANOSPHERES**

**TESIS
QUE PARA OPTAR POR EL GRADO DE:
MAESTRO EN CIENCIAS (FÍSICA)**

PRESENTA:

JONATHAN ALEXIS URRUTIA ANGUIANO

TUTOR:

**DR. ALEJANDRO REYES CORONADO
FACULTAD DE CIENCIAS, UNAM**

MIEMBROS DEL COMITÉ TUTOR

**DRA. CITLALI SÁNCHEZ-AKÉ
INSTITUTO DE CIENCIAS APLICADAS Y TECNOLOGÍA, UNAM**

**DR. GIUSEPPE PIRRUCCIO
INSTITUTO DE FÍSICA, UNAM**

CIUDAD DE MÉXICO, MÉXICO, 2022

Agradecimientos

Agradezco al CONACyT por la beca de estudios de posgrado que me otorgó por dos años, así como el apoyo por parte del proyecto de investigación DGAPA-UNAM PAPIIT IN107122.

*„Wo es viel Licht ist, ist auch viel Schatten.“
“Donde hay mucha luz, la sombra es profunda.”*

Götz von Berlichingen, primer acto.

J. W. von Goethe

Abstract/Resumen

Plasmonic metasurfaces, metallic nanostructures supported on a substrate, have been used as alternatives for biosensing due to their low-cost and easy-to-use features, and due to their light enhancement and confinement capacity. In common biosensing techniques, a liquid flows over the substrate, where the nanostructure is located, so there is a detachment risk. Therefore, a partial embedding of the nanostructure in the substrate is desirable, which modifies its optical response under ideal conditions. In this thesis, we study the optical response of a single spherical gold nanoparticle of 12.5 nm radius, suited for biosensing-aimed-metasurfaces, when the nanosphere is partially embedded in a flat glass substrate with an air matrix, and illuminated by an electromagnetic plane wave with wavelengths in the optical range, considering two states of polarization as well as different angles of incidence. The scattering, absorption and extinction cross sections, as well as the electric field induced by the nanosphere in the near and far-field regimes, are calculated with the Finite Element Method and compared with the analytical solutions of two limiting cases: a nanosphere embedded in an infinite matrix of air, and in an infinite matrix of glass. Based on the obtained numerical results, it was determined optimal configurations for biosensing with a disordered metasurface of partially embedded nanosphere of radius 12.5 nm in the diluted regime.

Las metasuperficies plasmónicas, nanoestructuras metálicas soportadas por un sustrato, han sido utilizadas como alternativas para el biosensado por su bajo costo de fabricación y fácil uso, debido a su capacidad de realce y confinamiento de la luz. En el proceso de biosensado, es común que un líquido fluya por encima del sustrato donde se encuentra la nanoestructura, por lo que existe un riesgo de desprendimiento de la misma. Por tanto, es deseable una incrustación parcial de la nanoestructura en el sustrato, lo que modifica su respuesta óptica en condiciones ideales. En esta tesis, se estudia la respuesta óptica de una sola nanopartícula esférica de oro de 12.5 nm de radio, adecuada para metasuperficies de biosensado, cuando la nanoesfera se incrusta parcialmente en una sustrato plano de vidrio con una matriz de aire, e iluminada por una onda plana electromagnética con longitudes de onda en el rango óptico, considerando los dos estados de polarización así como diferentes ángulos de incidencia. Las secciones transversales de esparcimiento, absorción y extinción, así como el campo eléctrico inducido por la nanoesfera en los regímenes de campo cercano y lejano, se calculan con el método de elementos finitos y se comparan con las soluciones analíticas en dos casos límite: una nanoesfera embebida en una matriz infinita de aire, y en una matriz infinita de vidrio. Con base en los resultados numéricos obtenidos, se encontraron configuraciones óptimas para el biosensado considerando una metasuperficie desordenada conformada por nanoesferas de oro de 12.5 nm de radio en el régimen diluido.

Contents

Acknowledgements	iii
Abstract	vii
Background and Motivation	1
1 Scattering Theory of a Single Spherical Particle	5
1.1 The Optical Theorem: Amplitude Matrix and Cross Sections	5
1.2 Mie Scattering	9
1.2.1 Vector Spherical Harmonics	9
1.2.2 Incident, Scattered, and Internal Electric Fields	12
1.2.3 Optical Properties of a Single Spherical (Gold) Particle	16
1.2.3.1 Localized Surface Plasmons	16
1.2.3.2 Far-Field Optical Properties	19
2 The Finite Element Method	23
2.1 Fundamentals	23
2.1.1 The Galerkin Method	24
2.1.2 The Finite Element Approximation	26
2.2 Numerical Approach to the Light Scattering Problem	29
2.2.1 Strong and Weak Formulations	30
2.2.2 The Nédélec Finite Element Family	32
2.2.3 Open Boundary Conditions	33
2.2.3.1 Sommerfeld's Radiation Condition	34
2.2.3.2 Perfectly Matching Layer	36
2.3 Finite Element Method and Analytical Solutions	39
3 Results and Discussion	47
3.1 Supported and Totally Embedded Spherical Particles	47
3.1.1 Normal Incidence	49
3.1.2 Supported Spherical Particle in Total Internal Reflection	55
3.2 Partially Embedded Spherical Particle	61
3.2.1 Normal Incidence	62
3.2.2 Partially Embedded Spherical Particle in Total Internal Reflection	66
Conclusions	79
Future Work: Application on Metasurfaces	80
A Mie Theory (Conventions)	83
B Size Correction to the Dielectric Function	87
C Brief COMSOL Implementation of the Scattering Problem	91
Index	101

Background and Motivation

Optical metasurfaces are bidimensional arrays of metallic/dielectric nanostructures —known as meta-atoms— specifically tailored to behave in a way no found in nature when illuminated at a specific wavelength [1, 2]. Depending on the physical properties of the meta-atoms, that is, their material, size, shape, and orientation and distribution within the bidimensional array [1, 3], metasurfaces allow to shape at will the spatial optical response of the system [4], thus suiting them for a variety of applications in fields such as spectroscopy [1], color structuration [2], communications [4], and sensing [1, 3–6]. In the last decades, the interest in optical metasurfaces for medical applications has increased due to the need for sensitive, fast, low-cost and easy-to-use technologies [3, 5], like metasurfaces with plasmonic (metallic) meta-atoms used as contrasting agents for bioimaging [3], and as free-label biosensors returning real-time measurements [1, 5, 7].

Metasurfaces designed for biosensing typically consist of a nanostructured substrate with compatible microfluidics illuminated with a white light source and a light recollection system, allowing for scattering or extinction measurements, followed by a spectrometer [5, 8]. One particular kind of biosensing-aimed metasurfaces consists in plasmonic meta-atoms, exploiting their property of high confinement of light at nanometric scales, yielding an improvement in the sensitivity of various detection techniques [1]. The light confinement is the result of the meta-atom’s Localized Surface Plasmon Resonances (LSPRs) being excited at the meta-atom’s interface with its surroundings, which occurs when the electromagnetic fields couple to the free electrons of the plasmonic structure [3–5]. Since the LSPR is material and geometry dependent, a variety of plasmonic metasurfaces have been designed [7–10] —each with its own benefits and disadvantages [4, 5]— as those shown in Fig. 1, all of which are plasmonic metasurfaces consisting of gold (Au) meta-atoms on a glass substrate but with different geometries and distributions within the metasurface. For example, Feuz et al. [8] employed a short-range ordered metasurface of nanoholes to sense protein binding events in real-time [Fig. 1a)], while Kabashin et al. [7] measured changes in the refractive index of the media embedding an ordered metasurface of plasmonic nanorods [Fig. 1b)]. Metasurfaces with simpler geometries and distributions can be used for biosensing as well, as shown Qiu et al. [9], who employed a disordered metasurface of nanospheres to detect selected DNA sequences from Severe Acute Respiratory Syndrome Coronavirus 2 (SARS-CoV-2) [Fig. 1c)], or by Svedendahl et al. [10], who sensed protein binding events with a short-range ordered metasurface of nanospheres [Fig. 1d)].

The design of plasmonic metasurfaces undergo several stages, but it can be roughly divided in two: its fabrication process and its theoretical behavior. On the one hand, the fabrication process relies on a variety of methods depending on the desired meta-atom’s physical

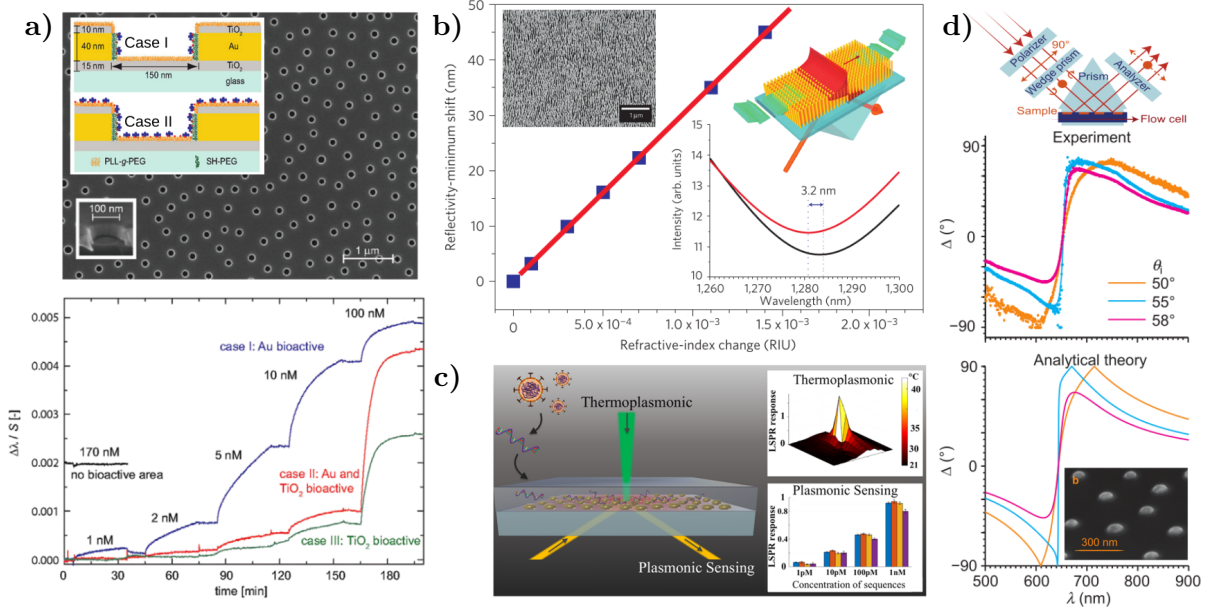


Fig. 1: Examples of biosensing-aimed plasmonic metasurfaces. **a)** Short-range ordered metasurface of nanoholes in a Au film [Scanning Electron Microscopy (SEM) image and meta-atom scheme] and real-time measurements of the LSPR redshift due to protein binding events; images extracted and adapted from [8]. **b)** Reflectivity minimum shift of an ordered metasurface of Au nanorods (SEM image and scheme in the inset) as a function of the refractive index change of the media embedding the metasurface; images extracted and adapted from [7]. **c)** Schematics of a disordered metasurface of Au nanospheres designed for SARS-CoV-2 detection and the LSPR response of its meta-atom: Thermoplasmonic and plasmonic sensing; image extracted from [9]. **d)** Experimental and theoretical results for the ellipsometric parameter Δ as a function of the incident wavelength, when a short-ranged ordered metasurface of Au nanospheres (SEM image) is illuminated by a non-polarized white light as shown in the setup diagram; extracted and adapted from [10].

properties and distribution. For example, metasurfaces suited for biosensing are commonly fabricated by lithography techniques, like electron beam lithography (ordered array) or hole-mask colloidal lithography (ordered and disordered arrays) [5], thermal annealing of thin metallic films (disordered arrays) by dewet [9] or laser ablation [11], and chemical growth-methods [5, 7]. On the other hand, the theoretical behavior estimates the optical response of the metasurface either by numerical methods, like the Finite Element Method (FEM) [8], the Finite Differences Time Domain (FDTD) [12], and the Discrete Dipole Approximation (DDA) [11], or by analytical models, like the Thin Island Theory [10, 13], the Dipolar Model [14] —both developed for disordered bidimensional arrays of nanospheres on a substrate— or the Maxwell Garnett Model —originally developed for 3D colloidal systems of spheres [15]— modified to describe bidimensional systems of non-spherical meta-atoms [7, 16, 17]. It is stressed that such calculations returns the optical response of the metasurface under ideal conditions as, for example, perfect geometrical shapes of the meta-atoms, perfect periodicity or even perfect deposition on the substrate supporting the meta-atoms.

Biosensing-aimed metasurfaces are supported on a substrate and immersed in an aqueous superstate [5], and its theoretical behavior is usually analyzed under the assumption that the meta-atoms are perfectly supported on the substrate and perfectly embedded in the superstate

[7, 10, 12–14]. Nevertheless, a partial embedding of the meta-atoms into the substrate may arise experimentally depending on the parameters of the fabrication process [11, 17]. The partial embedding of the meta-atoms is inversely related to the sensing area of the metasurface in the superstrate, thus limiting its performance, but it is also directly related to the washability of its meta-atoms due to the coupled microfluidics. Therefore, the partial embedding of the meta-atoms is a physical feature that can be optimized to design a long-lasting and sensitive metasurface for biosensing, yet, few publications on partially embedded nanostructures can be found even for simple geometries. Two examples of studies on partially embedded nanospheres are the results of Meng et al. [11] and of Moirangthem et al. [17], who respectively compared the experimental optical response of disordered bidimensional arrays of Au nanospheres with different incrustation degrees [see for example Fig. 2a)] employing DDA calculations of a single Au nanospheroid partially embedded and illuminated at normal incidence [Fig. 2b)], and by substituting the partial embedded Au nanospheres by two thin films described optically with the Maxwell Garnett Model with fitting parameters [Fig. 2c)] and a FDTD analysis for the spatial distribution of the electric near-field (not shown). While both publications mentioned before studied partially embedded meta-atoms (Au nanospheroids) neither of them focuses on their overall optical response, on its comparison with perfectly deposited meta-atoms nor on the effects the partial embedding may have on a metasurfaces for biosensing.

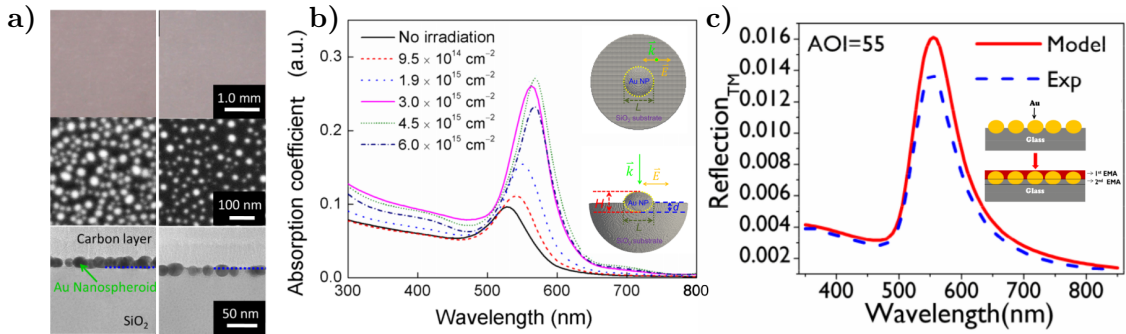


Fig. 2: Previous works on partially embedded Au nanospheroids. **a)** Optical image and Transmission Electron Microscopy (TEM) images in an aerial and transversal view of disordered bidimensional arrays of nanospheres supported on silica (SiO_2), with two different incrustation degrees, fabricated by laser ablation of a Au thin film; image extracted and adapted from [11]. **b)** Absorption coefficient of a single Au nanospheroid —with a depolarization factor L — when illuminated at normal incidence by a plane wave, calculated with DDA (see inset) considering the measured dimensions and incrustation degree of the Au nanospheres; images extracted and adapted from [11]. **c)** Experimental and theoretical reflectivity, as a function of the wavelength, of a disordered bidimensional array of partially embedded Au nanospheres illuminated at an angle of incidence of 55° with a transverse magnetic (TM) polarization state; the employed model consisted on substituting the partially embedded Au nanospheres by two layers whose optical response is described by the Maxwell Garnet Model with fitting parameters; images extracted and adapted from [17].

In this thesis, the optical properties of a single Au nanosphere partially embedded in a substrate —a potential meta-atom for biosensing-aimed metasurfaces— are studied when illuminated by a monochromatic plane wave at an oblique incidence with a defined polarization state. The system of interests consists in a spherical Au nanoparticle of radius 12.5 nm located at the planar interface between an air matrix and a glass substrate, whose embedding (including the perfectly supported and totally incrusted nanosphere) is characterized by the incrustation

parameter: the height of the center of the nanosphere relative to the interface divided by its radius. To determine the optical response of the system, the scattering and absorption efficiencies, the radiation pattern and the spatial distribution of induced electric field of the partially embedded nanosphere are calculated by means of the FEM —implemented in the commercial software COMSOL Multiphysics™ Ver. 5.4 (COMSOL)— and they are compared with the results obtained with the Mie Theory —the analytical solution of the limiting case of a single nanosphere embedded in a infinite medium—, which allows to estimate the performance of partially embedded nanospheres in metasurfaces tailored for biosensing.

The structure of this thesis divides its contents in three main chapters as follows: the scattering theory of single spherical particles is presented in Chapter 1, beginning with the general case of arbitrary particles in Section 1.1 and followed by the particular case of spherical scatterers, giving rise to the development of the Mie Theory in Section 1.2, which includes the derivation of the Vector Spherical Harmonics (Section 1.2.1) and the explicit solution to the scattered and internal electromagnetic fields (Section 1.2.2); in Section 1.2.3 the optical properties of a Au nanosphere of radius 12.5 nm embedded in air, and in glass, are calculated as the Mie-limiting case to the system of interest. Chapter 2 aims at providing the fundamentals of the FEM in Section 2.1, including the Galerkin Method in Section 2.1 and the characteristics of the Finite Element Approximation to a problem of partial differential equations in Section 2.1.2, and how the light scattering problem is addressed in the FEM in Section 2.2, which yields its Strong and Weak formulations (Section 2.2.1), the kind of finite element suited for the light scattering problem —the Nédélec Finite Element— (Section 2.2.2), and the so-called Open Boundary Conditions (Section 2.2.3) that allows to calculate optical properties for infinite non-periodic systems, as that of a single partially embedded nanosphere; after the theory of the FEM is presented, a convergence analysis is presented in Section 2.3 for the FEM implementation in COMSOL where its results are compared against the analytical solutions calculated by the Mie Theory. Then, the obtained results and their discussion are presented in Chapter 3, which corresponds to the scattering and absorption efficiencies, the radiation patterns and the spatial distribution of the induced electric field of a Au nanosphere of radius 12.5 nm under the following conditions: perfect support and total embedding in the substrate in Section 3.1, and partial embedding in Section 3.2; the first considers normal incidence illumination in both an internal and external illumination schema in Section 3.1.1 and in a Total Internal Reflection Configuration (TIR) in Section 3.1.2, while the second addresses the normal illumination case only in internal illumination and the TIR configuration in Sections 3.2.1 and 3.2.2, respectively. Lastly, the **Conclusions** of this work and its **future application on Metasurfaces** are located after the three main chapters.

As a complementary material, there are included three appendices describing the conventions employed for the calculations with the Mie Theory (Appendix A), the size correction to the dielectric function for small spherical nanoparticles (Appendix B) —both available in the public GitHub repository [jaurrutia/Mie-Theory-Mathematica](#)— and a brief guide of how the performed calculations were implemented in COMSOL (Appendix C).

Chapter 1

Scattering Theory of a Single Spherical Particle

The problem addressed in this thesis corresponds to the numerical analysis of the Localized Surface Plasmon Resonances (LSPR) excited on plasmonic spherical nanoparticles (NPs) when these are under realistic experimental conditions, such as those found in plasmonic biosensors, where the NPs are partially embedded in a substrate [17]. The performed analysis consists on the numerical calculation of the absorption, scattering and extinction cross sections of a partially embedded metal NP, employing the Finite Element Method (FEM). To verify the validity of the obtained numerical results, the problem of the absorption and scattering of light by a single free-standing spherical particle is considered. In this chapter, we revisit the general solution of the light absorption and scattering by both an arbitrary particle and a spherical particle, given by the Mie Theory¹ [20].

1.1 The Optical Theorem: Amplitude Matrix and Cross Sections

Let $\mathbf{E}^i = \mathbf{E}_0^i \exp(i\mathbf{k}^i \cdot \mathbf{r})$ be the electric field of an incident monochromatic plane wave with constant amplitude \mathbf{E}_0^i traveling through a non absorbing medium with refractive index n_{mat} , denominated as the matrix, in the direction $\mathbf{k}^i = k\hat{\mathbf{k}}^i$, with $k = (\omega/c)n_{\text{mat}}$ the wave number of the plane wave in the matrix, and let \mathbf{E}^{sca} be the scattered electric field due to a particle with arbitrary shape embedded in the matrix. In general, the scattered electric field propagates in all directions but for an observation point $\mathbf{r} = r\hat{\mathbf{e}}_r$, the traveling direction is defined by the vector $\mathbf{k}^{\text{sca}} = k\hat{\mathbf{k}}^{\text{sca}} = k\hat{\mathbf{e}}_r$. Due to the linearity of the Maxwell's equations, the incident and scattered electric fields in the far-field regime are related by the following linear relation [21]:

$$\mathbf{E}^{\text{sca}} = \frac{\exp(i\mathbf{k}^{\text{sca}} \cdot \mathbf{r})}{r} \mathbb{F}(\hat{\mathbf{k}}^{\text{sca}}, \hat{\mathbf{k}}^i) \mathbf{E}^i, \quad (1.1)$$

¹The term *Mie Theory* refers rather to a solution set to Maxwell's equations for the scattering of an electromagnetic plane wave due to a spherical particle, developed by Gustav Mie and published on 1907 [18]. Ludvig Lorenz published beforehand an equivalent solution to the same scattering problem nevertheless, Mie's solution consists in an iterative method suited for easier computations, which boosted its spread [19].

where $\mathbb{F}(\hat{\mathbf{k}}^{\text{sca}}, \hat{\mathbf{k}}^{\text{i}})$ is the scattering amplitude matrix from direction $\hat{\mathbf{k}}^{\text{i}}$ into $\hat{\mathbf{k}}^{\text{sca}}$. Since only the far-field is considered, both the incident and the scattered electric fields can be decomposed into two linearly independent components perpendicular to \mathbf{k}^{i} and \mathbf{k}^{sca} , respectively, each forming a right-handed orthonormal system. If the particle acting as a scatterer has a symmetric shape, it is convenient to define an orthonormal system relative to the scattering plane, which is the plane containing \mathbf{k}^{i} and \mathbf{k}^{sca} , since the elements of $\mathbb{F}(\hat{\mathbf{k}}^{\text{sca}}, \hat{\mathbf{k}}^{\text{i}})$ are simplified when represented in these bases [21]. In Fig. 1.1 a plane wave traveling in the z direction illuminates an arbitrary particle centered at the origin of the coordinate system and the scattering plane is depicted in green. By defining the directions perpendicular (\perp) and parallel (\parallel) to the scattering plane, the incident and scattered electric fields can be written as

$$\mathbf{E}^{\text{i}} = (E_{\parallel}^{\text{i}} \hat{\mathbf{e}}_{\parallel}^{\text{i}} + E_{\perp}^{\text{i}} \hat{\mathbf{e}}_{\perp}^{\text{i}}) \exp(i \mathbf{k}^{\text{i}} \cdot \mathbf{r}), \quad (1.2)$$

$$\mathbf{E}^{\text{sca}} = (E_{\parallel}^{\text{sca}} \hat{\mathbf{e}}_{\parallel}^{\text{sca}} + E_{\perp}^{\text{sca}} \hat{\mathbf{e}}_{\perp}^{\text{sca}}) \frac{\exp(i \mathbf{k}^{\text{sca}} \cdot \mathbf{r})}{r}, \quad (1.3)$$

where a harmonic time dependence $\exp(-i\omega t)$ has been omitted, and it has been assumed that the scattered field is described by a spherical wave; the superscript ‘i’ (‘sca’) denotes the orthonormal system defined by the incident plane wave (scattered fields). Since $\{\hat{\mathbf{e}}_{\perp}^{\text{i}}, \hat{\mathbf{e}}_{\parallel}^{\text{i}}, \hat{\mathbf{k}}^{\text{i}}\}$ and $\{\hat{\mathbf{e}}_{\perp}^{\text{sca}}, \hat{\mathbf{e}}_{\parallel}^{\text{sca}}, \hat{\mathbf{k}}^{\text{sca}}\}$ —shown in purple in Fig. 1.1 along with the Cartesian (blue) and spherical (black) unit vector bases— are right-handed orthonormal systems, they are related as follows

$$\hat{\mathbf{e}}_{\perp}^{\text{i}} = \hat{\mathbf{e}}_{\perp}^{\text{sca}} = \hat{\mathbf{k}}^{\text{sca}} \times \hat{\mathbf{k}}^{\text{i}}, \quad \hat{\mathbf{e}}_{\parallel}^{\text{i}} = \hat{\mathbf{k}}^{\text{i}} \times \hat{\mathbf{e}}_{\perp}^{\text{i}}, \quad \text{and} \quad \hat{\mathbf{e}}_{\parallel}^{\text{sca}} = \hat{\mathbf{k}}^{\text{sca}} \times \hat{\mathbf{e}}_{\perp}^{\text{sca}}. \quad (1.4)$$

As Eqs. (1.4) suggest, the unit vector bases of the orthonormal systems relative to the scattering plane depend on the scattering direction. For example, if the incident plane wave travels along the z axis (Fig. 1.1), then $\hat{\mathbf{k}}^{\text{i}} = \hat{\mathbf{e}}_z$ and $\hat{\mathbf{k}}^{\text{sca}} = \hat{\mathbf{e}}_r$. Thus the unit vector bases of the systems relative to the scattering plane are $\hat{\mathbf{e}}_{\parallel}^{\text{i}} = \cos \varphi \hat{\mathbf{e}}_x + \sin \varphi \hat{\mathbf{e}}_y$, $\hat{\mathbf{e}}_{\parallel}^{\text{sca}} = \hat{\mathbf{e}}_{\theta}$ and $\hat{\mathbf{e}}_{\perp}^{\text{i}} = \hat{\mathbf{e}}_{\perp}^{\text{sca}} = -\hat{\mathbf{e}}_{\varphi}$, with θ the polar angle and φ the azimuthal angle.

When an incident plane wave interacts with a particle with a complex refractive index $n_p(\omega)$, the total electric field outside the particle is given by the sum of the incident and the scattered fields. Therefore, the time averaged Poynting vector $\langle \mathbf{S} \rangle_t$, denoting the power flow per unit area, of the total field is given by

$$\langle \mathbf{S} \rangle_t = \underbrace{\frac{1}{2} \operatorname{Re} (\mathbf{E}^{\text{i}} \times \mathbf{H}^{\text{i}*})}_{\langle \mathbf{S}^{\text{i}} \rangle_t} + \underbrace{\frac{1}{2} \operatorname{Re} (\mathbf{E}^{\text{sca}} \times \mathbf{H}^{\text{sca}*})}_{\langle \mathbf{S}^{\text{sca}} \rangle_t} + \underbrace{\frac{1}{2} \operatorname{Re} (\mathbf{E}^{\text{i}} \times \mathbf{H}^{\text{sca}*} + \mathbf{E}^{\text{sca}} \times \mathbf{H}^{\text{i}*})}_{\langle \mathbf{S}^{\text{ext}} \rangle_t}, \quad (1.5)$$

with $*$ the complex conjugate operation and where the total Poynting vector is separated in three terms: the contribution from the incident field $\langle \mathbf{S}^{\text{i}} \rangle_t$, from the scattered field $\langle \mathbf{S}^{\text{sca}} \rangle_t$ and from their cross product denoted by $\langle \mathbf{S}^{\text{ext}} \rangle_t$. By means of the Faraday-Lenz’s law and Eqs. (1.1)–(1.3), the contribution to the Poynting vector from the incident and the scattered fields can be rewritten as

$$\langle \mathbf{S}^{\text{i}} \rangle_t = \frac{\|\mathbf{E}_0^{\text{i}}\|^2}{2Z_{\text{mat}}} \hat{\mathbf{k}}^{\text{i}}, \quad \text{and} \quad \langle \mathbf{S}^{\text{sca}} \rangle_t = \frac{\|\mathbf{E}^{\text{sca}}\|^2}{2Z_{\text{mat}}} \hat{\mathbf{k}}^{\text{sca}} = \frac{\|\mathbb{F}(\hat{\mathbf{k}}^{\text{sca}}, \hat{\mathbf{k}}^{\text{i}}) \mathbf{E}^{\text{i}}\|^2}{2Z_{\text{mat}} r^2} \hat{\mathbf{k}}^{\text{sca}}, \quad (1.6)$$

with $Z_{\text{mat}} = \sqrt{\mu_{\text{mat}}/\varepsilon_{\text{mat}}}$ the impedance of the non-absorbing matrix, while the crossed contri-

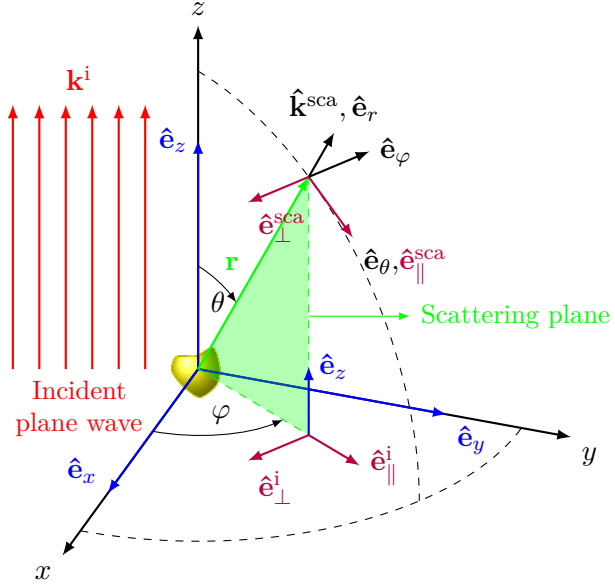


Fig. 1.1: The scattering plane (green) is defined by the vector $\hat{\mathbf{k}}^i$ (red) parallel to $\hat{\mathbf{e}}_z$ —the direction of the incident plane wave—and the vector $\hat{\mathbf{k}}^{sca}$ —the direction of the scattered field in a given point \vec{r} . The parallel and perpendicular components of the incident field relative to the scattering plane are $\hat{\mathbf{e}}_{\parallel}^i = \cos \varphi \hat{\mathbf{e}}_x + \sin \varphi \hat{\mathbf{e}}_y$ and $\hat{\mathbf{e}}_{\perp}^i = -\hat{\mathbf{e}}_{\varphi}$, while the components of the scattering field relative to the scattering plane are $\hat{\mathbf{e}}_{\parallel}^{sca} = \hat{\mathbf{e}}_{\theta}$, $\hat{\mathbf{e}}_{\perp}^{sca} = -\hat{\mathbf{e}}_{\varphi}$. The Cartesian unit vector basis is shown in blue, the spherical unit vector basis in black, while the basis of the orthonormal systems relative to the scattering plane are shown in purple.

bution is given by

$$\langle \mathbf{S}^{ext} \rangle_t = \text{Re} \left\{ \frac{\exp[-i(\mathbf{k}^{sca} - \mathbf{k}^i) \cdot \mathbf{r}]}{2Z_{\text{mat}} r^2} \left[\hat{\mathbf{k}}^{sca} (\mathbf{E}_0^i \cdot \mathbb{F}^* \mathbf{E}^{i*}) - \mathbb{F}^* \mathbf{E}^{i*} (\mathbf{E}_0^i \cdot \hat{\mathbf{k}}^{sca}) \right] \right. \\ \left. + \frac{\exp[i(\mathbf{k}^{sca} - \mathbf{k}^i) \cdot \mathbf{r}]}{2Z_{\text{mat}} r^2} \left[\hat{\mathbf{k}}^i (\mathbb{F} \mathbf{E}^i \cdot \mathbf{E}_0^{i*}) - \mathbf{E}_0^{i*} (\mathbb{F} \mathbf{E}^i \cdot \hat{\mathbf{k}}^i) \right] \right\}, \quad (1.7)$$

where the scattering amplitude matrix is evaluated as $\mathbb{F}(\hat{\mathbf{k}}^{sca}, \hat{\mathbf{k}}^i)$.

The power scattered by the particle can be calculated by integrating $\langle \mathbf{S}^{sca} \rangle_t$ in a closed surface surrounding the particle; if the scattered power is normalized by the irradiance of the incident field $\|\langle \mathbf{S}^i \rangle_t\|$, it is obtained a quantity with units of area, known as the scattering cross section C_{sca} , given by [20]

Scattering Cross Section

$$C_{\text{sca}} = \frac{2Z_{\text{mat}}}{\|\mathbf{E}_0\|^2} \oint_S \langle \mathbf{S}^{sca} \rangle_t \cdot d\mathbf{a} = \oint_S \frac{\|\mathbb{F}(\hat{\mathbf{k}}^{sca}, \hat{\mathbf{k}}^i) \mathbf{E}^i\|^2}{\|\mathbf{E}_0^i\|^2} d\Omega, \quad (1.8)$$

where $d\Omega$ is the differential solid angle.

Similarly, an absorption cross section C_{abs} can be defined as well. On the one side, the absorption cross section is given by the integral on a closed surface of $\langle -\mathbf{S} \rangle_t$ [Eq. (1.5)] divided by the irradiance of the incident field, where the minus sign is chosen so that $C_{\text{abs}} > 0$ if the particle absorbs energy [20]. On the other side, if an Ohmic material with conductivity $\sigma(\omega) = i\omega n_p^2(\omega)$ [22] for the particle is assumed, through Joule's heating law [21], the absorption cross section can be computed as

Ohmic Particle - Absorption Cross Section

$$C_{\text{abs}} = \frac{1}{2} \int_V \frac{\text{Re}(\mathbf{J} \cdot \mathbf{E}^{\text{int}*})}{\|\mathbf{E}_0^i\|^2 / 2Z_{\text{mat}}} dV = \int_V \omega Z_{\text{mat}} \text{Im}(n_p^2) \frac{\|\mathbf{E}^{\text{int}}\|^2}{\|\mathbf{E}_0^i\|^2} dV, \quad (1.9)$$

where the integration is performed inside the particle, and \mathbf{J} and \mathbf{E}^{int} are the volumetric electric current density and the total electric field in this region, respectively. Both the scattering and the absorption cross sections are quantities related to the optical signature of a particle [23], and their relation can be made explicit by performing the surface integral representation of C_{abs} and defining C_{ext} , that is,

$$\begin{aligned} C_{\text{abs}} &= - \frac{2Z_{\text{mat}}}{\|\mathbf{E}_0^i\|^2} \int_S (\langle \mathbf{S}^i \rangle_t + \langle \mathbf{S}^{\text{sca}} \rangle_t + \langle \mathbf{S}^{\text{ext}} \rangle_t) \cdot d\mathbf{a} \\ &= -C_{\text{sca}} - \frac{2Z_{\text{mat}}}{\|\mathbf{E}_0^i\|^2} \int_S \langle \mathbf{S}^{\text{ext}} \rangle_t \cdot \hat{\mathbf{e}}_r d\Omega \\ &= -C_{\text{sca}} + C_{\text{ext}}, \end{aligned} \quad (1.10)$$

where the contribution of $\langle \mathbf{S}^i \rangle_t$ to the integral is zero since a non-absorbing matrix was assumed. From Eq. (1.10) it can be seen that C_{ext} takes into account both mechanisms for energy losses (scattering and absorption), thus it is called the extinction cross section. To solve the integral in Eq. (1.10) let us define θ as the angle between $\hat{\mathbf{k}}^{\text{sca}}$ and $\hat{\mathbf{k}}^i$ as the polar angle and φ as the azimuthal angle, as shown in Fig 1.1. With this choice of coordinates, the extinction cross section can be computed as

$$\begin{aligned} C_{\text{ext}} &= -\text{Re} \left\{ \frac{\exp(-ikr)}{\|\mathbf{E}_0^i\|^2} \oint_S \exp(ikr \cos \theta) (\mathbf{E}^i \cdot \mathbb{F}^* \mathbf{E}^{i*}) d\Omega \right. \\ &\quad + \frac{\exp(ikr)}{\|\mathbf{E}_0^i\|^2} \oint_S \exp(-ikr \cos \theta) \cos \theta (\mathbf{E}^{i*} \cdot \mathbb{F} \mathbf{E}^i) d\Omega \\ &\quad \left. + \frac{\exp(ikr)}{\|\mathbf{E}_0^i\|^2} \oint_S \exp(-ikr \cos \theta) \sin \theta (E_{0,x}^i \cos \varphi + E_{0,y}^i \sin \varphi) (\mathbb{F} \mathbf{E}^i \cdot \mathbf{k}^i) d\Omega \right\}, \end{aligned} \quad (1.11)$$

using that $\hat{\mathbf{k}}^{\text{sca}} \cdot \hat{\mathbf{e}}_r = 1$, $\hat{\mathbf{k}}^i \cdot \hat{\mathbf{e}}_r = \cos \theta$ and $\mathbf{E}^{\text{sca}} \cdot \hat{\mathbf{e}}_r = 0$. The integrals in Eq. (1.11) can be solved by a twofold integration by parts in the polar angle θ and by neglecting terms proportional to r^{-2} . This process leads to a zero contribution from the integrand proportional to $\sin \theta$ in Eq. (1.11) and, after rearranging the other terms in their real and imaginary parts, it follows that C_{ext} depends only on the forward direction $\hat{\mathbf{k}}^{\text{sca}} = \hat{\mathbf{k}}^i$ ($\theta = 0$). This result is known as the Optical Theorem whose mathematical expression is given by [21, 23, 24]:

Optical Theorem - Extinction Cross Section

$$C_{\text{ext}} = C_{\text{abs}} + C_{\text{sca}} = \frac{4\pi}{k\|\mathbf{E}_0^i\|^2} \text{Im} \left[\mathbf{E}_0^i \cdot \mathbb{F}^*(\hat{\mathbf{k}}^i, \hat{\mathbf{k}}^i) \mathbf{E}^{i*} \right]. \quad (1.12)$$

The Optical Theorem is a general result applicable to general scattering phenomena, both quantum and classical [20, 24], and its derivation rely in the incident field being a plane wave [see Eq. (1.11)] and more precisely, in the lack of longitudinal components of the incident field [25, 26].

From Eqs. (1.5) and (1.12) it can be seen that the extinction of light, the combined result of scattering and absorption as energy loss mechanisms, is also a manifestation of the interference between the incident and the scattered fields and, remarkably, that the overall effect of the light extinction can be fully understood by analyzing the amplitude of the scattering field in the forward direction. It is worth noting that Eq. (1.12) is an exact relation but its usefulness is bond to the correct evaluation of the scattering amplitude matrix \mathbb{F} [21]. Thus, in the following Sections a scattering problem with spherical symmetry will be assumed, so that the exact solution to the scattering amplitude matrix can be developed; this solution is known as the *Mie Theory*.

1.2 Mie Scattering

In the previous Section, it was concluded that the extinction of light due to the interaction between a particle and a monochromatic plane wave can be determined through the amplitude of the scattered field in the forward direction. This is stated in the Optical Theorem, which is an exact relation, but inaccuracies may arise when either the scattering amplitude matrix or the extinction cross section are approximated². A particular case in which the scattering amplitude matrix can be exactly calculated is when the scatterer has spherical symmetry. In order to address this special case, it will be introduced a vectorial basis with spherical symmetry, known as the Vector Spherical Harmonics (VSH). Once the VSH are defined, they will be used to write a monochromatic plane wave in terms of the VSH. By imposing the continuity of the tangential components of the electric and magnetic fields, the scattered field can be also written in terms of the VSH. As a particular example of interest, shown in the last Section, the optical properties of a gold nanoparticle with radius of 12.5 nm are calculated.

1.2.1 Vector Spherical Harmonics

The electric and magnetic fields, denoted as \mathbf{E} and \mathbf{B} , respectively, correspond to a solution to the homogeneous vectorial Helmholtz equation when a harmonic time dependence and a spatial domain with no external charge nor current densities is assumed, that is,

²See for example Section 2.4 from Ref. [21] on the Rayleigh Scattering, and Section 21.7 from Ref. [27] on Thompson scattering.

Vectorial Helmholtz Equation

$$\nabla^2 \mathbf{E}(\mathbf{r}, \omega) + k^2 \mathbf{E}(\mathbf{r}, \omega) = \mathbf{0}, \quad \nabla^2 \mathbf{B}(\mathbf{r}, \omega) + k^2 \mathbf{B}(\mathbf{r}, \omega) = \mathbf{0}, \quad (1.13)$$

where the vectorial operator ∇^2 must be understood as $\nabla^2 = \nabla(\nabla \cdot) - \nabla \times \nabla \times$, and k is the wave number in the matrix, which follows the dispersion relation $k = (\omega/c)n_{\text{mat}}$, with $n_{\text{mat}} = \sqrt{\mu_{\text{mat}}\varepsilon_{\text{mat}}/\mu_0\varepsilon_0}$ the refractive index of the matrix, μ_{mat} its magnetic permeability and ε_{mat} its dielectric function. It is possible to build a basis set for the electric and magnetic fields as long as the elements of this basis are also solution to Eq. (1.13). One alternative is to employ the following set of vector functions [28]

$$\mathbf{L} = \nabla \psi, \quad (1.14a)$$

$$\mathbf{M} = \nabla \times (\mathbf{r}\psi), \quad (1.14b)$$

$$\mathbf{N} = \frac{1}{k} \nabla \times \mathbf{M}, \quad (1.14c)$$

that are solution to the homogeneous vectorial Helmholtz equation as long as the scalar function ψ is solution to the scalar Helmholtz equation³

$$\nabla^2 \psi + k^2 \psi = 0. \quad (1.15)$$

The triad $\{\mathbf{L}, \mathbf{M}, \mathbf{N}\}$ is a set of vectors⁴ that obey Helmholtz equation, *i.e.*, they can be directly identified as electric or magnetic fields. The elements of the vector basis from Eq. (1.14) are known as the Vector Spherical Harmonics and are defined as Stratton [28], or by Bohren and Huffman [20], and the scalar function ψ is known as the generating function of the VSH. From the definition of the VSH in Eqs. (1.14) it can be seen that \mathbf{L} has only a longitudinal component, while \mathbf{M} has only transversal components —specifically \mathbf{M} is tangential to any sphere of radius $\|\mathbf{r}\|$, and \mathbf{N} have both longitudinal and transversal components.

If spherical coordinates are chosen, and it is assumed that $\psi(r, \theta, \varphi) = R(r)\Theta(\theta)\Phi(\varphi)$, then Eq. (1.15) can be decoupled into three ordinary differential equations:

$$\frac{d^2 \Phi}{d\varphi^2} + m^2 \Phi = 0, \quad (1.16)$$

$$\frac{1}{\sin \theta} \frac{d}{d\theta} \left(\sin \theta \frac{d\Theta}{d\theta} \right) + \left[\ell(\ell+1) - \frac{m^2}{\sin^2 \theta} \right] \Theta = 0, \quad (1.17)$$

$$\frac{d}{dr} \left(r^2 \frac{dR}{dr} \right) + \left[(kr)^2 - \ell(\ell+1) \right] R = 0, \quad (1.18)$$

where ℓ takes natural values and zero, and $|m| \leq \ell$ so that Φ and Θ are uni-valued and finite on

³This result can be proved by considering the following: Let f be \mathcal{C}^3 and \mathbf{F} a \mathcal{C}^2 . Then, it is true that $\nabla^2(\nabla f) = \nabla(\nabla^2 f)$, and $\nabla \times (\nabla^2 \mathbf{F}) = \nabla^2(\nabla \times \mathbf{F})$.

⁴Using the Einstein sum convention with ϵ_{ijk} the Levi-Civita symbol, Eq. (1.14b) can be written as follows: $M_i = [\nabla \times (\mathbf{r}\psi)]_i = \epsilon_{ijk} \partial_j (r_k \psi) = \psi \epsilon_{ijk} \partial_j (r_k) - \epsilon_{ikj} r_k \partial_j \psi = \psi [\nabla \times \mathbf{r}]_i - [\mathbf{r} \times \nabla \psi]_i = -[\mathbf{r} \times \nabla \psi]_i = [\mathbf{L} \times \mathbf{r}]_i$, therefore \mathbf{M} is orthogonal to \mathbf{L} and \mathbf{r} . From Eq. (1.14c) $\mathbf{M} \cdot \mathbf{N} = 0$, so \mathbf{M} is orthogonal to \mathbf{N} . As it will be shown in Eq. (1.22), not necessarily \mathbf{L} is orthogonal to \mathbf{N} in a geometrical sense.

a sphere. The Eqs. (1.17) and (1.18) can be rewritten as

$$(1 - \mu^2) \frac{d^2\Theta}{d\mu^2} - 2\mu \frac{d\Theta}{d\mu} + \left[\ell(\ell + 1) - \frac{m^2}{1 - \mu^2} \right] \Theta = 0, \quad \text{with } \mu = \cos\theta, \quad (1.19)$$

$$\rho \frac{d}{d\rho} \left(\rho \frac{dZ}{d\rho} \right) + \left[\rho^2 - \left(\ell + \frac{1}{2} \right)^2 \right] Z = 0, \quad \text{with } Z = R\sqrt{\rho} \text{ and } \rho = kr. \quad (1.20)$$

The solution to Eq. (1.19) are the associated Legendre functions $P_\ell^m(\mu)$ and to Eq. (1.20) the spherical Bessel functions of the first (j_ℓ) and second (y_ℓ) kind, or the spherical Hankel functions of first ($h_\ell^{(1)} = j_\ell + iy_\ell$) and second ($h_\ell^{(2)} = j_\ell - iy_\ell$) kind. Following the convention from most Mie Scattering literature [27], the solution to Eq. (1.16) can be decomposed into an odd ('o') and an even ('e') solutions, that is, as sine and cosine functions, thus restricting the values of m to non negative integers. After this, the generating function of the VSH is given by

ψ : Generating function of the vectorial spherical harmonics

$$\psi_{\text{o}\ell m}(r, \theta, \varphi) = \frac{\sin(m\varphi)}{\cos(m\varphi)} P_\ell^m(\cos\theta) z_\ell(kr), \quad (1.21)$$

where z_ℓ stands for any of the four solutions to the radial equation [Eq. (1.20)]. Substituting Eq. (1.21) in Eqs. (1.14a)–(1.14c) one finds the VSH:

Vectorial Spherical Harmonics

$$\begin{aligned} \mathbf{L}_{\text{o}\ell m} &= \frac{\cos(m\varphi)}{\sin(m\varphi)} k P_\ell^m(\cos\theta) \frac{dz_\ell(kr)}{d(kr)} \hat{\mathbf{e}}_r + \frac{\cos(m\varphi)}{\sin(m\varphi)} k \frac{z_\ell(kr)}{kr} \frac{dP_\ell^m(\cos\theta)}{d\theta} \hat{\mathbf{e}}_\theta + \\ &\quad - \frac{\sin(m\varphi)}{\cos(m\varphi)} km \frac{P_\ell^m(\cos\theta)}{\sin\theta} \frac{z_\ell(kr)}{kr} \hat{\mathbf{e}}_\varphi \end{aligned} \quad (1.22a)$$

$$\mathbf{M}_{\text{o}\ell m} = \frac{-\sin(m\varphi)}{+\cos(m\varphi)} m z_\ell(kr) \frac{P_\ell^m(\cos\theta)}{\sin\theta} \hat{\mathbf{e}}_\theta - \frac{\cos(m\varphi)}{\sin(m\varphi)} z_\ell(kr) \frac{dP_\ell^m(\cos\theta)}{d\theta} \hat{\mathbf{e}}_\varphi, \quad (1.22b)$$

$$\begin{aligned} \mathbf{N}_{\text{o}\ell m} &= \frac{\cos(m\varphi)}{\sin(m\varphi)} \frac{z_\ell(kr)}{kr} \ell(\ell + 1) P_\ell^m(\cos\theta) \hat{\mathbf{e}}_r + \frac{\cos(m\varphi)}{\sin(m\varphi)} \frac{1}{kr} \frac{d[kr z_\ell(kr)]}{d(kr)} \frac{dP_\ell^m(\cos\theta)}{d\theta} \hat{\mathbf{e}}_\theta + \\ &\quad - \frac{\sin(m\varphi)}{\cos(m\varphi)} m \frac{1}{kr} \frac{d[kr z_\ell(kr)]}{d(kr)} \frac{P_\ell^m(\cos\theta)}{\sin\theta} \hat{\mathbf{e}}_\varphi, \end{aligned} \quad (1.22c)$$

where the term $\ell(\ell + 1)P_\ell^m$ arises since the associated Legendre functions obeys Eq. (1.19).

The choice at z_ℓ in Eqs. (1.22) is due to the physical constraints of the scattering problem. On the one hand, the spherical Bessel function of first kind, unlike the other three proposed solutions to the radial equation, is finite at $r = 0$, thus it is appropriate for the internal electric field and plane waves. This choice at z_ℓ will be denoted in the VSH with the superscript (1). On the other hand, the asymptotic behavior ($\ell \ll \rho$) of the Hankel function of first kind $h_\ell^{(1)} = j_\ell + iy_\ell$ and its derivative represent outgoing spherical waves [20]

$$h_\ell^{(1)}(\rho) \approx (-i)^\ell \frac{\exp(i\rho)}{i\rho} \quad \text{and} \quad \frac{dh_\ell^{(1)}(\rho)}{d\rho} \approx (-i)^\ell \frac{\exp(i\rho)}{\rho}, \quad (1.23)$$

which are well suited for the scattered field; the VSH with $z_\ell = h_\ell^{(1)}$ will be denoted with the superscript (3).

From here on, the VSH will be those defined in Eq. (1.14) under the condition of being a solution to the vectorial Helmholtz equation, which lead to the generating function ψ to be a solution to the scalar Helmholtz equation. Nevertheless, there are other definitions for the VSH as discussed by Barrera, Estevez, and Giraldo [29]. The chosen definition of the VSH allows the VSH to be interpreted directly as electric and magnetic fields, specifically identifying \mathbf{N} with the electric contribution and \mathbf{M} with the magnetic due to its behavior in the far-field regime⁵, as it will be shown in Section 1.2.3.1.

1.2.2 Incident, Scattered, and Internal Electric Fields

Let \mathbf{E}^i be an x -polarized plane wave traveling in the \mathbf{e}_z direction; its representation in the spherical unit vector basis is

$$\mathbf{E}^i(\mathbf{r}) = E_0(\sin \theta \cos \varphi \hat{\mathbf{e}}_r + \cos \theta \cos \varphi \hat{\mathbf{e}}_\theta - \sin \varphi \hat{\mathbf{e}}_\varphi) \exp(ikr \cos \theta). \quad (1.24)$$

The monochromatic plane wave is a transversal wave, thus it can be written in terms of only $\mathbf{M}^{(1)}$ and $\mathbf{N}^{(1)}$, where the radial dependency is given by j_ℓ since the monochromatic plane wave is finite everywhere. Even more, due to the dependence on φ , it is only restricted to values of $m = 1$. By inspection on the radial component of \mathbf{E}^i , proportional to $\cos \varphi$, it depends only on $\mathbf{N}_{e1\ell}^{(1)}$, and on the azimuthal component, proportional to $\sin \varphi$, it depends only on $\mathbf{M}_{o1\ell}^{(1)}$. Thus, Eq. (1.24) can be written as a linear combination of $\mathbf{N}_{e1\ell}^{(1)}$ and $\mathbf{M}_{o1\ell}^{(1)}$. Through the orthogonality relations of the VSH [see Eqs. (A.22)–(A.25) from Appendix A], the x -polarized plane wave can be written as [28]

$$\mathbf{E}^i(\mathbf{r}) = E_0 \sum_{\ell=1}^{\infty} \frac{i^\ell (2\ell+1)}{\ell(\ell+1)} (\mathbf{M}_{o1\ell}^{(1)} - i\mathbf{N}_{e1\ell}^{(1)}), \quad (1.25a)$$

$$\mathbf{H}^i(\mathbf{r}) = \frac{-kE_0}{\mu\omega} \sum_{\ell=1}^{\infty} \frac{i^\ell (2\ell+1)}{\ell(\ell+1)} (\mathbf{M}_{e1\ell}^{(1)} + i\mathbf{N}_{o1\ell}^{(1)}). \quad (1.25b)$$

In the problem of scattering due to a spherical particle of radius a , the continuity conditions on the tangential components of the electric and magnetic fields are written as

$$(\mathbf{E}^i + \mathbf{E}^{\text{sca}} - \mathbf{E}^{\text{int}}) \Big|_{r=a} \times \hat{\mathbf{e}}_r = (\mathbf{H}^i + \mathbf{H}^{\text{sca}} - \mathbf{H}^{\text{int}}) \Big|_{r=a} \times \hat{\mathbf{e}}_r = 0, \quad (1.26)$$

with \mathbf{E}^{sca} (\mathbf{E}^{int}) the scattered (internal) electric field and \mathbf{H}^{sca} (\mathbf{H}^{int}) the scattered (internal) magnetic field. If the incident field \mathbf{E}^i is given by an x -polarized plane wave [Eq. (1.24)] then the scattered and internal fields can be written also as a linear combination of $\mathbf{M}_{o1\ell}$ and $\mathbf{N}_{e1\ell}$. The internal field is finite inside the particle, thus the radial dependence is given by the function $j_\ell(k_p a)$, with k_p the wave number inside the particle. For the scattered fields, it is chosen the

⁵The VSH \mathbf{L} is left out from the identification of either an electric or magnetic contribution since it is purely longitudinal and thus not suitable for the far-field.

spherical Hankel function of first kind $h^{(1)}(ka)$ due to its asymptotic behavior of a spherical outgoing wave. Such a choice for the radial dependence is denoted by the superscript (3) over the VSH. To simplify the following steps, the scattered and the internal electric fields are written as

$$\mathbf{E}^{\text{sca}}(\mathbf{r}) = E_0 \sum_{\ell=1}^{\infty} \frac{i^\ell(2\ell+1)}{\ell(\ell+1)} (ia_\ell \mathbf{N}_{e1\ell}^{(3)} - b_\ell \mathbf{M}_{o1\ell}^{(3)}), \quad (1.27a)$$

$$\mathbf{E}^{\text{int}}(\mathbf{r}) = E_0 \sum_{\ell=1}^{\infty} \frac{i^\ell(2\ell+1)}{\ell(\ell+1)} (c_\ell \mathbf{M}_{o1\ell}^{(1)} - id_\ell \mathbf{N}_{e1\ell}^{(1)}), \quad (1.27b)$$

with the respective magnetic fields

$$\mathbf{H}^{\text{sca}}(\mathbf{r}) = \frac{-kE_0}{\mu\omega} \sum_{\ell=1}^{\infty} \frac{i^\ell(2\ell+1)}{\ell(\ell+1)} (ib_\ell \mathbf{N}_{o1\ell}^{(3)} + a_\ell \mathbf{M}_{e1\ell}^{(3)}), \quad (1.28a)$$

$$\mathbf{H}^{\text{int}}(\mathbf{r}) = \frac{-kE_0}{\mu_p\omega} \sum_{\ell=1}^{\infty} \frac{i^\ell(2\ell+1)}{\ell(\ell+1)} (d_\ell \mathbf{M}_{e1\ell}^{(1)} + ic_\ell \mathbf{N}_{o1\ell}^{(1)}). \quad (1.28b)$$

Since only the term $m = 1$ is taken into account, it is convenient to define the angular functions

$$\pi_\ell(\cos\theta) = \frac{P_\ell^1(\cos\theta)}{\sin\theta} \quad \text{and} \quad \tau_\ell(\cos\theta) = \frac{dP_\ell^1(\cos\theta)}{d\theta}, \quad (1.29)$$

which are not orthogonal but their addition and subtraction are, that is $\pi_\ell \pm \tau_\ell$ are orthogonal functions [20]; see Eq. (A.20) in Appendix A. After substitution of Eqs. (1.25), (1.27) and (1.28) into Eq. (1.26) and considering the orthogonality between \mathbf{M} and \mathbf{N} , between even and odd VSH, and between $\pi_\ell \pm \tau_\ell$, it is shown that the coefficients a_ℓ , b_ℓ , c_ℓ and d_ℓ are given by two decoupled equation systems

$$\begin{pmatrix} [xh_\ell^{(1)}(x)] & (\mu/\mu_p)[(mx)j_\ell(mx)] \\ m[xh_\ell^{(1)}(x)]' & [(mx)j_\ell(mx)]' \end{pmatrix} \begin{pmatrix} a_\ell \\ d_\ell \end{pmatrix} = \begin{pmatrix} [xj_\ell(x)] \\ m[xj_\ell(x)]' \end{pmatrix}, \quad (1.30)$$

and

$$\begin{pmatrix} m[xh_\ell^{(1)}(x)] & [(mx)j_\ell(mx)] \\ [xh_\ell^{(1)}(x)]' & (\mu/\mu_p)[(mx)j_\ell(mx)]' \end{pmatrix} \begin{pmatrix} b_\ell \\ c_\ell \end{pmatrix} = \begin{pmatrix} m[xj_\ell(x)] \\ [xj_\ell(x)]' \end{pmatrix}, \quad (1.31)$$

where $m = k_p/k = n_p/n_{\text{mat}}$ is the contrast between the sphere and the matrix, $x = ka = 2\pi n_{\text{mat}}(a/\lambda)$ is the size parameter and ' denotes derivative with respect to the argument of the spherical Bessel or Hankel functions; the size parameter compares the size of the scatterer with the incident wavelength in the matrix: the larger the value of x , the bigger the scatterer can be considered inside such a matrix. Equations (1.30) and (1.31) are simplified when the Riccati-Bessel functions $\psi_\ell(\rho) = \rho j_\ell(\rho)$ and $\xi(\rho) = \rho h_\ell^{(1)}(\rho)$ are introduced.

When a non-magnetic particle nor matrix are assumed ($\mu_p = \mu = \mu_0$), the coefficients a_ℓ and b_ℓ are known as the Mie coefficients, whose expressions are calculated by inverting Eqs. (1.30) and (1.31), yielding

Mie Coefficients

$$a_\ell = \frac{\psi_\ell(x)\psi'_\ell(mx) - m\psi_\ell(mx)\psi'_\ell(x)}{\xi_\ell(x)\psi'_\ell(mx) - m\psi_\ell(mx)\xi'_\ell(x)}, \quad (1.32a)$$

$$b_\ell = \frac{m\psi_\ell(x)\psi'_\ell(mx) - \psi_\ell(mx)\psi'_\ell(x)}{m\xi_\ell(x)\psi'_\ell(mx) - \psi_\ell(mx)\xi'_\ell(x)}. \quad (1.32b)$$

Likewise, the coefficients c_ℓ and d_ℓ are given by

$$c_\ell = \frac{-m\xi'_\ell(x)\psi_\ell(x) + m\xi_\ell(x)\psi'_\ell(x)}{m\xi_\ell(x)\psi'_\ell(mx) - \psi_\ell(mx)\xi'_\ell(x)}, \quad (1.33a)$$

$$d_\ell = \frac{-m\xi'_\ell(x)\psi_\ell(x) + m\psi'_\ell(mx)\psi'_\ell(x)}{\xi_\ell(x)\psi'_\ell(mx) - m\psi_\ell(mx)\xi'_\ell(x)}. \quad (1.33b)$$

Even though the coefficients of the linear combination for the scattered and internal fields were obtained assuming an x -polarized incident field, due to the spherical symmetry of the problem, by applying the transformation $\varphi \rightarrow \varphi + \pi/2$ the same procedure is valid for a y -polarized incident field [20], therefore all quantities related to the scattered and the internal field can be expressed in terms of Eqs. (1.32) and (1.33).

As discussed in Section 1.1, the optical properties of a particle are encoded into the scattering, absorption, and extinction cross sections. These quantities can be calculated by means of the scattering amplitude matrix [Eq. (1.1)] and the Optical Theorem [Eq. (1.12)]. Since the particle is spherical, it is convenient to exploit the symmetry of the problem by decomposing the scattered electric field [Eq. (1.27a)] into components parallel and perpendicular to the scattering plane. To obtain the scattering amplitude matrix expressed in an orthogonal base relative to the scattering plane ($\hat{\mathbf{e}}_s^s = \hat{\mathbf{e}}_\theta$ and $\hat{\mathbf{e}}_s^s = -\hat{\mathbf{e}}_\varphi$) let us substitute the Mie coefficients [Eqs. (1.32)] into Eq. (1.27a) while rewriting the VSH $\mathbf{M}_{o1\ell}^{(3)}$ and $\mathbf{N}_{e1\ell}^{(3)}$ [Eqs. (1.22)] in terms of the Riccati-Bessel function ξ and its derivative:

$$\mathbf{E}^{sca} \cdot \hat{\mathbf{e}}_r = \frac{\cos \varphi}{(kr)^2} \sum_{\ell=1}^{\infty} E_0 i^\ell (2\ell + 1) i a_\ell \xi(kr) \pi_\ell(\cos \theta) \sin \theta, \quad (1.34a)$$

$$\mathbf{E}^{sca} \cdot \hat{\mathbf{e}}_\parallel^{sca} = \frac{\cos \varphi}{kr} \sum_{\ell=1}^{\infty} E_0 i^\ell \frac{2\ell + 1}{\ell(\ell + 1)} [i a_\ell \xi'_\ell(kr) \tau_\ell(\cos \theta) - b_\ell \xi_\ell(kr) \pi_\ell(\cos \theta)], \quad (1.34b)$$

$$\mathbf{E}^{sca} \cdot \hat{\mathbf{e}}_\perp^{sca} = \frac{\sin \varphi}{-kr} \sum_{\ell=1}^{\infty} E_0 i^\ell \frac{2\ell + 1}{\ell(\ell + 1)} [i a_\ell \xi'_\ell(kr) \pi_\ell(\cos \theta) - b_\ell \xi_\ell(kr) \tau_\ell(\cos \theta)]. \quad (1.34c)$$

Following a similar procedure but substituting Eq. (1.33) into Eq. (1.27b), the internal electric field \mathbf{E}^{int} can be rewritten also in terms of the Riccati-Bessel functions as

$$\mathbf{E}^{int} \cdot \hat{\mathbf{e}}_r = -\frac{\cos \varphi}{(k_p r)^2} \sum_{\ell=1}^{\infty} E_0 i^\ell (2\ell + 1) i d_\ell \psi(k_p r) \pi_\ell(\cos \theta) \sin \theta, \quad (1.35a)$$

$$\mathbf{E}^{int} \cdot \hat{\mathbf{e}}_\parallel^{sca} = \frac{\cos \varphi}{k_p r} \sum_{\ell=1}^{\infty} E_0 i^\ell \frac{2\ell + 1}{\ell(\ell + 1)} [-i d_\ell \psi'_\ell(k_p r) \tau_\ell(\cos \theta) + c_\ell \psi_\ell(k_p r) \pi_\ell(\cos \theta)], \quad (1.35b)$$

$$\mathbf{E}^{\text{int}} \cdot \hat{\mathbf{e}}_{\perp}^{\text{sca}} = \frac{\sin \varphi}{-k_p r} \sum_{\ell=1}^{\infty} E_0 i^{\ell} \frac{2\ell+1}{\ell(\ell+1)} [-id_{\ell} \psi'_{\ell}(k_p r) \pi_{\ell}(\cos \theta) + c_{\ell} \psi_{\ell}(k_p r) \tau_{\ell}(\cos \theta)]. \quad (1.35c)$$

The scattering amplitude matrix relates the incident electric field to the scattered electric field in the far-field regime, that is when $kr \gg 1$. Considering that the series of Eqs. (1.34a)-(1.34c) converge uniformly, so all contributions after the sufficiently large term ℓ_c of the sum can be neglected for all values of kr , the asymptotic expressions for the ξ Riccati-Bessel function and its derivative can be employed, which are given by [20]

$$\xi(kr) \approx (-i)^{\ell} \frac{\exp(ikr)}{i}, \quad \text{and} \quad \frac{d\xi(kr)}{d(kr)} = (-i)^{\ell} \exp(ikr) \left(\frac{1}{ikr} + 1 \right), \quad \text{when } \ell_c^2 \ll kr. \quad (1.36)$$

Substituting Eq. (1.36) into Eqs. (1.34a)-(1.34c) and neglecting terms proportional to $(kr)^{-2}$, it yields a zero radial electric field, while

$$\mathbf{E}^{\text{sca}} \cdot \hat{\mathbf{e}}_{\parallel}^{\text{sca}} \approx \frac{\exp(ikr)}{r} \left\{ \frac{i}{k} \sum_{\ell=1}^{\infty} \frac{2\ell+1}{\ell(\ell+1)} [a_{\ell} \tau_{\ell}(\cos \theta) + b_{\ell} \pi_{\ell}(\cos \theta)] \right\} E_0 \cos \varphi, \quad (1.37a)$$

$$\mathbf{E}^{\text{sca}} \cdot \hat{\mathbf{e}}_{\perp}^{\text{sca}} \approx \frac{\exp(ikr)}{r} \left\{ \frac{i}{k} \sum_{\ell=1}^{\infty} \frac{2\ell+1}{\ell(\ell+1)} [a_{\ell} \pi_{\ell}(\cos \theta) + b_{\ell} \tau_{\ell}(\cos \theta)] \right\} E_0 (-\sin \varphi), \quad (1.37b)$$

where it can be identified that $\mathbf{E}^i \cdot \hat{\mathbf{e}}_{\parallel}^i = E_0 \cos \varphi$ and $\mathbf{E}^i \cdot \hat{\mathbf{e}}_{\perp}^i = -E_0 \sin \varphi$ for \mathbf{E}^i a plane wave traveling along the z direction with an arbitrary polarization. Finally, the scattering amplitude matrix for a spherical particle can be obtained by comparing Eqs. (1.37a) and (1.37b) with Eq. (1.1), yielding

Scattering Amplitude Matrix for Spherical Particles

$$\mathbb{F}(\hat{\mathbf{k}}^{\text{sca}}, \hat{\mathbf{k}}^i) = \begin{pmatrix} \frac{i}{k} S_2(\theta) & 0 \\ 0 & \frac{i}{k} S_1(\theta) \end{pmatrix}, \quad (1.38a)$$

with $\hat{\mathbf{k}}^{\text{sca}} = \hat{\mathbf{e}}_r$, $\hat{\mathbf{k}}^i = \hat{\mathbf{e}}_z$, $\cos \theta = \hat{\mathbf{k}}^{\text{sca}} \cdot \hat{\mathbf{k}}^i$ and

$$S_1(\theta) = \sum_{\ell=1}^{\infty} \frac{2\ell+1}{\ell(\ell+1)} [a_{\ell} \tau_{\ell}(\cos \theta) + b_{\ell} \pi_{\ell}(\cos \theta)], \quad (1.38b)$$

$$S_2(\theta) = \sum_{\ell=1}^{\infty} \frac{2\ell+1}{\ell(\ell+1)} [a_{\ell} \pi_{\ell}(\cos \theta) + b_{\ell} \tau_{\ell}(\cos \theta)], \quad (1.38c)$$

which depend entirely on the angular functions $\pi_{\ell}(\cos \theta)$ and $\tau_{\ell}(\cos \theta)$ modulated by the Mie coefficients a_{ℓ} and b_{ℓ} . The scattering amplitude matrix \mathbb{F} shows the symmetry of the system when it is written in a base relative to the scattering plane, as stated in Section 1.1. Since the scatterer is a spherical isotropic NP, \mathbb{F} is a diagonal matrix in the base $\{\hat{\mathbf{e}}_{\parallel}^{\text{sca}}, \hat{\mathbf{e}}_{\perp}^{\text{sca}}\}$, that is, that the scattered electric field \mathbf{E}^{sca} maintains the same polarization degree relative to the scattering plane than the incident electric field \mathbf{E}^i that illuminates the spherical particle.

1.2.3 Optical Properties of a Single Spherical (Gold) Particle

In previous Sections, the general theory for the light scattering was developed, introducing the scattering amplitude matrix \mathbb{F} [Eq. (1.1)]. Then, the particular problem of a spherical scatterer was addressed and explicit expressions for the scattered electric field [Eq. (1.37)] and for \mathbb{F} were obtained [Eq. (1.38a)] in terms of the Mie coefficients a_ℓ and b_ℓ [Eqs. (1.32)], as well as the internal electric field inside the scatterer [Eq. (1.35)] in terms of the coefficients c_ℓ and d_ℓ [Eqs. (1.33)]. The optical properties of a particle is related to the electric field outside the scatterer, and can be studied within two different spatial regions: the near-field and the far-field regimes. The near-field region consists in the complete analytical solution of the scattered electric field [Eq. (1.27a)], while the far-field regime considers only the contributions proportional to r^{-1} , with r the distance between the center of the scatterer and the measurement point; the optical properties in the far-field regime can be determined by the scattering amplitude matrix \mathbb{F} itself. In this last Section, the previous results are employed to calculate the optical properties of a spherical gold nanoparticle (AuNP) with a radius of 12.5 nm, either embedded in an air or in a glass matrix, when it is illuminated by an incident plane wave with a wavelength λ .

1.2.3.1 Localized Surface Plasmons

The optical properties of a particle, either in the near or the far-field regime, are determined by the Mie coefficients a_ℓ and b_ℓ [Eqs. (1.32)] since the exact solution to the scattered electric field \mathbf{E}^{sca} [Eq. (1.27a)] is a linear combination of the vector spherical harmonics $\mathbf{N}_{\text{e}\ell}^{(3)}$ and $\mathbf{M}_{\text{o}\ell}^{(3)}$, modulated by a_ℓ and b_ℓ , respectively. Thus, the physical interpretation of each term ℓ in the linear combination, as well as of $\mathbf{N}_{\text{e}\ell}^{(3)}$ and $\mathbf{M}_{\text{o}\ell}^{(3)}$, can be determined by plotting each term independently. By understanding each contribution, the optical response of a particle illuminated by a plane wave can be studied both in the near and far regimes.

Figure 1.2 shows a decomposition of the scattered electric field \mathbf{E}^{sca} of a spherical particle into its contributions proportional to a_1 [Fig. 1.2a)], b_1 [Fig. 1.2b)], a_2 [Fig. 1.2c)] and b_2 [Fig. 1.2d)], when the particle is illuminated by an x -polarized plane wave traveling in the z direction. The vectorial behavior of the a_ℓ contributions to \mathbf{E}^{sca} are given by the VSH $\mathbf{N}_{\text{e}\ell}^{(3)}$ and by $\mathbf{M}_{\text{o}\ell}^{(3)}$ for the b_ℓ contributions. The scattered electric field is evaluated at a spherical surface (gray sphere) with radius larger than that of the scatterer. The arrow stream on the spherical surface corresponds to the pointing direction of each contribution to \mathbf{E}^{sca} parallel to the evaluation sphere, while the color code corresponds to the magnitude of the scattered electric field at each point; the solid shape at the center of the coordinate system corresponds to a contour surface $\|\mathbf{E}^{\text{sca}}\|$.

The general effect of each contribution to the scattered electric field \mathbf{E}^{sca} can be understood by analyzing their behavior around the points where the scattered electric field drops to zero; such points are called nodes and are shown in dark bluish colors in Fig. 1.2. The number of nodes over the evaluation sphere (gray surface) is proportional to the chosen value of ℓ . For example, if $\ell = 1$ [Figs. 1.2a) and 1.2b)] there is a pair of such nodes and if $\ell = 2$ [Figs. 1.2c) and 1.2d)] there are two pairs, where each pair consists of two nodes at opposite sides of the evaluation sphere. When comparing the contributions proportional to a_1 and a_2 [Figs. 1.2a) and

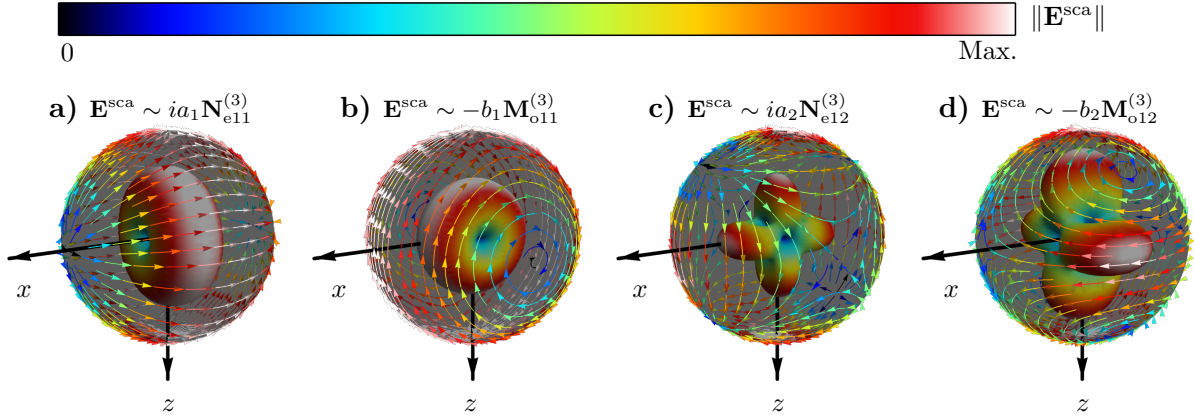


Fig. 1.2: Decomposition of the scattered electric field \mathbf{E}^{sca} into its contributions proportional to **a**) a_1 , **b**) b_1 , **c**) a_2 and **d**) b_2 [see Eq. (1.27a)] when a spherical particle (not shown) is illuminated by an x -polarized plane wave traveling in the z direction. The scattered electric field \mathbf{E}^{sca} is evaluated at a sphere larger than the particle: the arrow stream corresponds to the projection parallel to the evaluation sphere of \mathbf{E}^{sca} and the color code corresponds to the magnitude of \mathbf{E}^{sca} . A contour surface of the magnitude of \mathbf{E}^{sca} is located at the center of each coordinate system.

[1.2c)] with contributions from b_1 and b_2 [Figs. 1.2b) and 1.2d)], one notices a difference in the location of the pairs of nodes for a fixed value of ℓ , which differ spatially by a rotation around the z axis of an angle $\varphi = \pi/2$. Another difference between the contributions of a_ℓ and b_ℓ to \mathbf{E}^{sca} are the trajectories they performed around each pair of nodes: In the a_ℓ contributions the scattered electric field flows from one node to its pair, thus following an open path, while the scattered electric field for the b_ℓ contributions circulates around the nodes forming a closed path. Taking into account such behaviors, it can be seen that the a_ℓ (b_ℓ) contribution describes the electric field of an electric (magnetic) dipole when $\ell = 1$ and of an electric (magnetic) quadrupole when $\ell = 2$. Extrapolating such behavior for an arbitrary ℓ , it can be concluded that the a_ℓ contributions to the scattered electric field, described by the VSH $\mathbf{N}_{e\ell 1}^{(3)}$, correspond to the electric field of an electric multipole of order ℓ , while the b_ℓ contribution, described by the VSH $\mathbf{M}_{o\ell 1}^{(3)}$, correspond to the electric field of a magnetic multipole of order ℓ .

The scattered electric field \mathbf{E}^{sca} of a spherical particle can be written, according to Eq. (1.27a), as a linear contribution of electric fields associated to electric and magnetic multipoles, as shown in Fig. 1.2, modulated by the Mie coefficients a_ℓ and b_ℓ , respectively. Thus, the field \mathbf{E}^{sca} reproduces the pattern of a pure electric or magnetic multipole of order ℓ if a_ℓ or b_ℓ are maximized, accordingly. Since the Mie coefficients [Eqs. (1.32)] depend on the material and size of the spherical scatter, on the wavelength and traveling media of the incident plane wave, and on the order ℓ , the values of a_ℓ and b_ℓ are maximized when there is a coupling between the scatterer and the plane wave for a fixed ℓ , which yields a Localized Surface Plasmon Resonance (LSPR). The condition to obtain a LSPR is given by the limit when the denominators of the Eqs. (1.32) tend to zero, that is

$$\xi_\ell(x)\psi'_\ell(mx) - m\psi_\ell(mx)\xi'_\ell(x) \rightarrow 0, \quad (\text{Electric LSPR}), \quad (1.39)$$

$$m\xi_\ell(x)\psi'_\ell(mx) - \psi_\ell(mx)\xi'_\ell(x) \rightarrow 0, \quad (\text{Magnetic LSPR}), \quad (1.40)$$

where $\psi_\ell(\rho) = \rho j_\ell(\rho)$ and $\xi(\rho) = \rho h_\ell^{(1)}(\rho)$ are the Riccati-Bessel functions, the operator $'$ denotes the derivative with respect to their argument, $x = 2\pi n_m(a/\lambda)$ is the size parameter, with a the radius of the particle and λ the wavelength of the incident plane wave, and $m = n_p/n_{\text{mat}}$ is the contrast between the refractive indices of the particle (n_p) and the matrix (n_m), both of which are in general wavelength dependent. A simplified condition for the LSPR can be obtained by employing the Drude Model —see Eq. (B.1) in Appendix B— for the refractive index of the particle [30]. Nevertheless, the roots in Eqs. (1.39) and (1.40) can be found numerically and yield, in general, different solutions.

The system of interest in this work consists of a spherical gold nanoparticle (AuNP) of radius $a = 12.5$ nm, characterized by the dielectric function reported by Johnson and Christy [31]. However, this experimental data corresponds to a bulk sample, meaning that it may not reproduce the optical behavior of a NP since surface effects cannot be neglected due to its size [32]. In order to study the optical properties of AuNP, for example to determine the conditions for its LSPRs from Eqs. (1.39) and (1.40), while considering surface effects, a size correction to the dielectric function of the AuNP was performed as described in Appendix B. A more detailed discussion on such size effects is performed by analyzing the far-field regime in the next section.

The induced electric field \mathbf{E}^{ind} , inside the NP (internal electric field) and outside of it (scattered electric field), of a spherical AuNP of radius $a = 12.5$ nm were calculated at the wavelength of the dipolar ($\ell = 1$) LSPR when the AuNP is embedded in an air matrix ($n_{\text{mat}} = 1$) and when it is illuminated by an x -polarized electric field \mathbf{E}^i traveling in the z direction. In Fig. 1.3 the normalized magnitude of \mathbf{E}^{ind} is evaluated at the plane $y = 0$ [Fig. 1.3a)] where the incident electric field is parallel (\parallel) to the scattering plane, and at the plane $x = 0$ [Fig. 1.3b)] where the incident electric field is perpendicular (\perp) to the scattering plane; in both figures the dashed lines correspond to the surface of the AuNP. The excitation wavelength λ of the LSPR for the described system was calculated by employing the size corrected dielectric function for the AuNP in Eq. (1.39).

By comparing the magnitude of the induced electric \mathbf{E}^{ind} field in Fig. 1.3 outside the AuNP, which was calculated up to the multipolar contribution of $\ell = 7$ accordingly with the Wacombe criteria for convergence [20], with the electric dipolar contribution of the scattered electric field in Fig. 1.2a), the same contour pattern is found. The norm of \mathbf{E}^{ind} evaluated at a plane parallel to the scattering plane ($y = 0$) shows a contour pattern of two lobes, which is characteristic of an electric dipole. When the induced electric field is evaluated at a perpendicular plane relative to the scattering plane ($x = 0$), the pattern observed corresponds to the azimuthal symmetry of the dipolar electric field. Lastly, it can be seen that there is an enhancement of twofold the induced electric field relative to the incident electric field [reddish zones in Fig. 1.3a)]; such enhancement corresponds to the LSPR.

From the analysis of the electric field scattered by the particle in the near-field regime, the LSPR can be visualized on the surface of the particle at the conditions imposed by Eq. (1.39) for the electric multipoles. The conditions to excite the LSPR are dictated by the Mie coefficients, therefore the LSPR can also be identified in the far-field regime since the amplitude scattering matrix, from which any optical properties in the far-field regime can be calculated, is written according to Eq. (1.38a) in terms of a_ℓ and b_ℓ . In the following section, the optical properties in the far-field regime are calculated and their relation to the LSPR is established, yielding to the

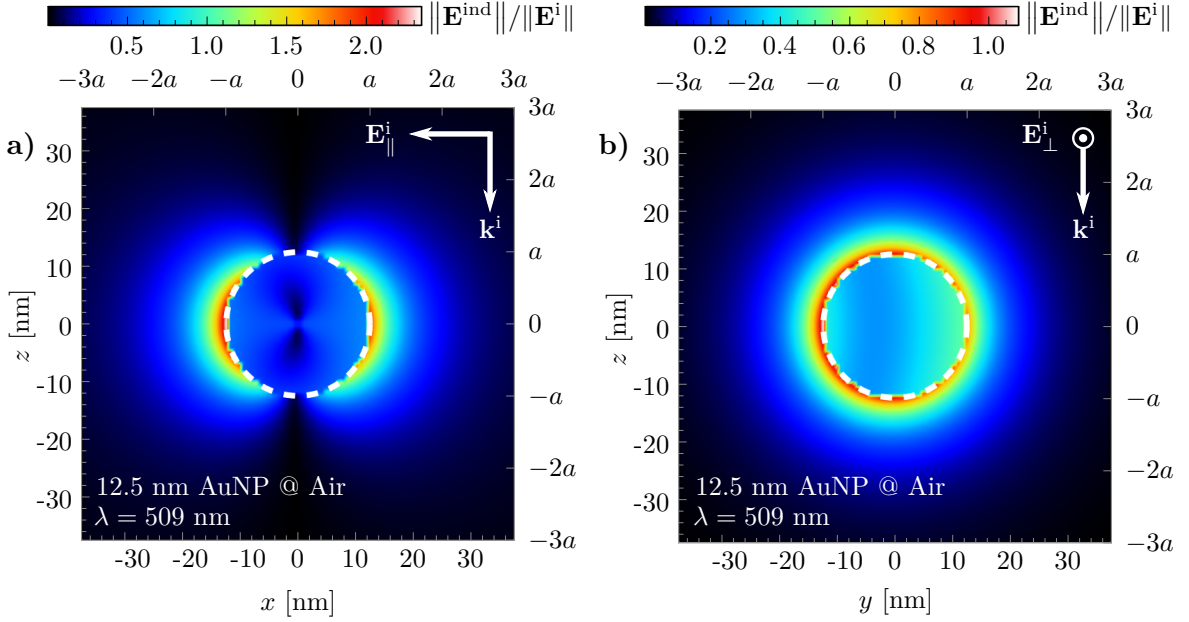


Fig. 1.3: Induced electric field \mathbf{E}^{int} evaluated at the planes **a)** $y = 0$ and **b)** $x = 0$ of a 12.5 nm Au spherical NP (dashed lines) embedded in an air ($n_{\text{mat}} = 1$) when illuminated by an incident plane wave with an x -polarized electric field \mathbf{E}^{i} traveling in the direction \mathbf{k}^i along the z axis with an excitation wavelength $\lambda = 509 \text{ nm}$ of the LSPR. At the plane $x = 0$, the incident electric field is parallel to the scattering plane, while it is perpendicular to it at $x = 0$. The optical response of the 12.5 nm AuNP was modeled using a size correction to the experimental data reported by Johnson and Christy [31].

observation of the LSPR in the far-field.

1.2.3.2 Far-Field Optical Properties

The Localized Surface Plasmon Resonance (LSPR) occurs when an electric plane wave illuminating a particle couples with scattered electric field giving rise to a standing wave on the surface of the particle with a specific spatial distribution depending on its geometry, size and material [33]. For a spherical particle, the LSPR occurs when the conditions in Eqs. (1.39) and (1.40) are met, which maximize the Mie coefficients a_ℓ and b_ℓ [Eq. (1.32)], respectively. The Mie coefficients do not only relate to the electric field in the near-field but also to quantities in the far-field regime, such as to the scattering amplitude matrix \mathbb{F} [Eq. (1.38a)]. Therefore, the LSPR can also be identified by analyzing experimental or theoretical results of optical properties such as the scattering C_{sca} and extinction C_{ext} cross sections, which are related to \mathbb{F} . Hereby, explicit expressions for the optical properties in the far-field regime, for a scattering sphere, are obtained.

By substituting the scattering amplitude matrix for a spherical particle [Eq. (1.38a)] into Eqs. (1.8) and (1.12) the scattering C_{sca} and extinction C_{ext} cross sections are obtained, respectively; the absorption cross section C_{abs} can be calculated by calculating $C_{\text{ext}} - C_{\text{sca}}$. Assuming an incident plane wave with an x -polarized electric field \mathbf{E}^{i} , and evaluating the scattering amplitude matrix in the forward direction $\theta = 0$, equivalent to $\cos\theta = 1$, the

extinction cross section C_{ext} is given by

$$C_{\text{ext}} = \frac{4\pi}{k\|\mathbf{E}^i\|^2} \text{Im}\left[\frac{i}{k} S_2(\theta=0) \mathbf{E}^i \cdot \mathbf{E}^{i*}\right] = \frac{2\pi}{k^2} \sum_{\ell=1}^{\infty} (2\ell+1) \text{Re}(a_\ell + b_\ell), \quad (1.41)$$

where the Eq. (A.16) in Appendix A was employed to evaluate the angular functions $\pi_\ell(\cos\theta)$ and $\tau_\ell(\cos\theta)$. In a similar manner, the scattering cross section C_{sca} can be written as

$$C_{\text{sca}} = \int_0^{2\pi} \int_0^\pi \frac{(iS_2(\theta)\mathbf{E}^i)^*(iS_2(\theta)\mathbf{E}^i)}{k^2 \mathbf{E}^i} \sin\theta d\varphi d\theta = \frac{2\pi}{k^2} \sum_{\ell=1}^{\infty} (2\ell+1)(|a_\ell|^2 + |b_\ell|^2), \quad (1.42)$$

where the orthogonality relations of $\pi_\ell(\cos\theta) \pm \tau_\ell(\cos\theta)$ [Eq. (A.20) in Appendix A] were used. In order to compare absorption, scattering and extinction of light by a spherical particle, independently of its radius a , it is convenient to define the efficiencies of absorption Q_{abs} , scattering Q_{sca} and extinction Q_{ext} by normalizing the absorption, scattering and extinction cross sections by the geometrical cross section of the spherical particle, yielding the dimensionless expressions

$$\frac{C_{\text{ext}}}{\pi a^2} = \frac{C_{\text{abs}}}{\pi a^2} + \frac{C_{\text{sca}}}{\pi a^2} \quad \rightarrow \quad Q_{\text{ext}} = Q_{\text{abs}} + Q_{\text{sca}}. \quad (1.43)$$

The Eq. (1.43), along with the optical theorem [Eq. (1.12)], states that the extinction of light considers the combination of both absorption and scattering mechanisms. Since the analytical expression of C_{ext} for a spherical particle [Eq. (1.41)] is proportional to the real part of the sum of the Mie coefficients a_ℓ and b_ℓ , then it is also maximized at the LSPR. Therefore, the LSPR can be observed in the far-field by calculating or measuring the extinction cross section.

In order to study the LSPR of a spherical AuNP of radius $a = 12.5$ nm, the extinction Q_{ext} and the scattering Q_{sca} efficiencies are shown in Fig. 1.4, as a function of the wavelength λ of the incident plane wave illuminating the NP. Two different matrices were considered: a matrix of air with a refractive index of $n_{\text{mat}} = 1$ (black lines) and of glass with $n_{\text{mat}} = 1.5$ (orange lines). The optical response of the AuNP was modeled by a dielectric function considering the raw data (solid lines) from Johnson and Christy [31], and a size correction to it (dashed lines). In all cases, the LSPR wavelength is indicated in the figure at the maximum of the extinction efficiencies.

By comparing Figs. 1.4a) and 1.4b), it is determined that the main loss mechanism in the system is absorption since Q_{sca} is two orders of magnitude smaller than Q_{ext} for all λ in the visible spectrum. Yet, another difference between Q_{sca} and Q_{ext} is the value of λ that maximizes them: for a 12.5 nm AuNP the wavelength of maximum scattering is redshifted ~ 12 nm from LSPR excitation wavelength for both matrices. An effect common for both the scattering and the extinction efficiencies is an overall enhancement when the refractive index of the matrix increases, as well as a redshift of ~ 25 nm of the LSPR excitation wavelength and the wavelength of maximum scattering—compare the black curves ($n_{\text{mat}} = 1$, air) with the orange ones ($n_{\text{mat}} = 1.5$, glass)—, which can be understood by analyzing the size parameter $x = (2\pi/\lambda)an_{\text{mat}}$. Since x is a linear function of n_{mat} , the AuNP embedded in glass optically responds like a larger NP compared with the same NP in air, thus having a more significant contribution from the scattering to the light extinction mechanism inside glass, as well as an increase in the absorption.

1.2 Mie Scattering

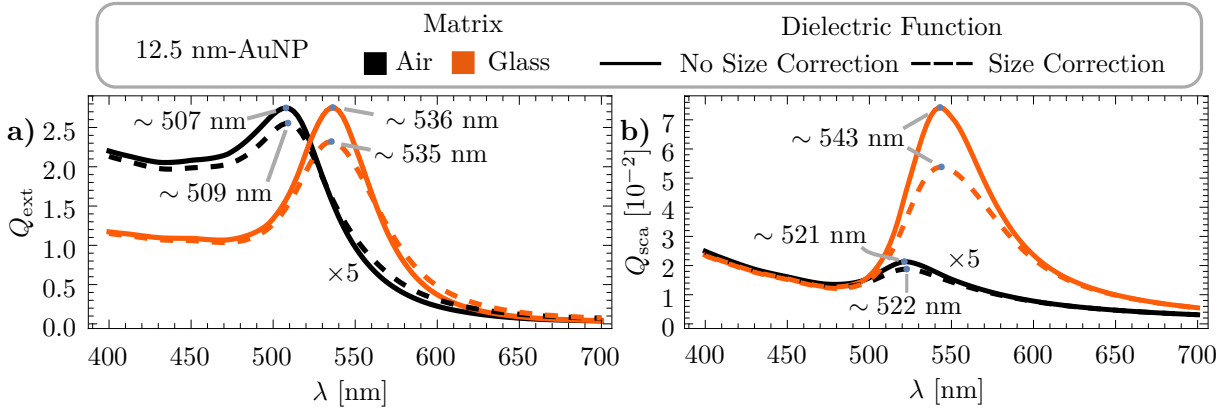


Fig. 1.4: a) Extinction Q_{ext} and b) scattering Q_{sca} efficiencies of a 12.5 nm Au spherical NP embedded in air (black, $n_{\text{mat}} = 1$) and in glass (orange, $n_{\text{mat}} = 1.33$), as a function of the wavelength λ of the incident plane wave. The solid curves were calculated by considering no size effects on the dielectric function of the AuNP, while the dashed curves consider a size correction; in all cases the experimental data of Johnson and Christy [31] was employed.

The effect of the size correction to the dielectric function of the AuNP can be seen directly by comparing the solid and dashed lines in Fig. 1.4. On the one hand, there is a spectral shift of the LSPR excitation wavelength of ~ 2 nm. On the other hand, the value of the efficiencies around the wavelength where the extinction and the scattering is maximized decreases in all cases. This behavior can be explained by how the size correction is performed: as explained in Appendix B, the surface effects are taken into account by introducing a smaller mean free path for the free electrons inside the AuNP, therefore increasing the value of the damping constant and thus leading to a larger imaginary part for the dielectric functions employed, which is related to the absorption mechanisms [34]. The decrease in the efficiencies due to a size corrected dielectric function is more evident for a matrix of glass than of air, since the AuNP is optically larger in such matrix as explained above. From this analysis it can be concluded that the most notable effect of a size correction to the dielectric function of a NP is the decrease in the extinction and scattering efficiencies, while there is still a spectral shift of the LSPR, whose effect is less relevant the larger the size parameter is.

While the scattering efficiency Q_{sca} is an integral quantity, that is, it describes the scattering in all directions of a plane wave traveling in the direction \mathbf{k}^i due to the interaction with a NP, the scattering amplitude matrix elements $S_1(\theta)$, given for a spherical NP by Eq. (1.38b), and $S_2(\theta)$, by Eq. (1.38c), depict the electric field \mathbf{E}^{sca} , at a measurement angle θ , scattered by a NP polarized in a direction perpendicular (\perp) to the scattering plane and parallel (\parallel) to it, respectively. A radiation pattern helps to visualize the behavior of $S_{1,2}(\theta)$, a dimensionless parameter such as the scattering efficiency, by plotting their squared modulus as a function of θ , as it is shown in for a 12.5 nm AuNP in Fig. 1.5, where $|S_1(\theta)|^2$ (solid lines) and $|S_2(\theta)|^2$ (dashed lines) are shown for two different scenarios: a AuNP embedded in air [Fig. 1.5a), black curves] illuminated at a wavelength $\lambda = 522$ nm and a AuNP embedded in glass [Fig. 1.5b), orange curves] illuminated at $\lambda = 543$ nm. The values for the wavelength of the incident plane wave corresponds to the value of λ where Q_{sca} is maximized for each matrix as shown in Fig. 1.4.

The quantities $|S_{1,2}(\theta)|^2$ for a 12.5 nm AuNP embedded in air ($n_{\text{mat}} = 1$, black curves) are one order of magnitude smaller than into glass ($n_{\text{mat}} = 1.5$, orange curves), meaning that the AuNP scatters light less efficiently in air than in glass, which is consistent with the results

1. SCATTERING THEORY OF A SINGLE SPHERICAL PARTICLE

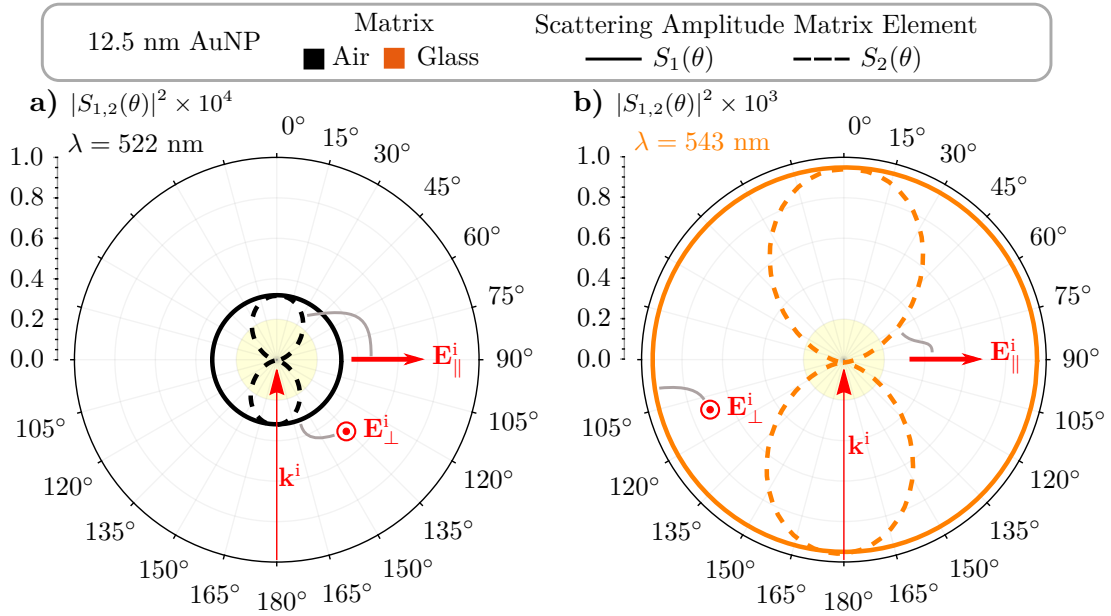


Fig. 1.5: Radiation pattern of a 12.5 nm Au spherical NP (yellow) embedded **a)** in air illuminated by a plane wave at a wavelength of $\lambda = 522$ nm and **b)** in glass illuminated at $\lambda = 543$ nm; the wavelength in each case corresponds to the wavelength of maximum scattering (see Fig. 1.4). The solid (dashed) lines corresponds to the scattering matrix element S_1 (S_2) related to an incident electric field \mathbf{E}^i traveling in the \mathbf{k}^i direction and polarized perpendicularly (parallel) to the page. It was considered for both matrices a size correction to the experimental data of Johnson and Christy [31] for the electromagnetic response of the AuNP.

obtained for the scattering efficiency Q_{sca} in Fig. 1.4. On the angular dependency, the radiation pattern of the AuNP in both matrices follow the same tendency: a homogeneous scattered electric field when the AuNP scatters the perpendicularly polarized incident electric field \mathbf{E}_\perp^i (continuous lines), and a two-lobe pattern when illuminated with a parallel polarized \mathbf{E}_\parallel^i . The observed radiation pattern can be identified in the near-field regime, see Fig. 1.3, nevertheless within the radiation pattern analysis, the presence of the LSPR is lost, unlike within an analysis of the extinction cross section.

Chapter 2

The Finite Element Method

Several physical problems are described by systems of partial differential equations (PDE) alongside boundary or initial conditions, whose analytical solution can be achieved only in some cases. For example, the scattering of light due to an arbitrary spherical particle, described by the vectorial Helmholtz equation [Eq. (1.13)] with the boundary conditions at the surface of the spherical particle given by Eq. (1.26), is one of the few physical problems with an analytical solution. Nevertheless, it is set in an ideal scenario where the particle is a perfect sphere, it is isolated and embedded in a non-absorbing matrix. Any of these conditions on the geometry and physical properties of the described system were to change, the scattering problem may not have an analytical solution; for such cases one alternative is to employ a numerical approach to find an approximated solution. Among the numerical methods employed in Electrodynamics, one of them is the Finite Element Method (FEM).

In this Chapter the theory behind the FEM is presented with its implementation on the light scattering problem. In Section 2.1 fundamentals of the FEM are explained: the Galerkin method and the concept of the finite element. In Section 2.2, the light scattering problem is revisited so it can be approached through an integral formulation, allowing the use of the FEM since a generalization of the concepts seen in Section 2.1 into vectorial quantities is needed, as well as the introduction of boundary conditions in open regions so an infinite medium problem, such as the light scattering, can be approached numerically. In the last section, the scattering problem of an isolated spherical particle, addressed in Chapter 1, is solved analytically and numerically—employing the commercial software COMSOL Multiphysics™ Ver. 5.4—and their results are contrasted.

2.1 Fundamentals

Any system of PDE that characterizes a physical system in either equilibrium or in a steady-state, with a set of boundary conditions, can be described by [35]

$$\mathcal{L}[\mathbf{u}(\mathbf{r})] - \mathbf{f}_\Omega = 0, \quad \mathcal{C}[\mathbf{u}(\mathbf{r})] = \mathbf{f}_{\partial\Omega}, \quad (2.1)$$

where \mathcal{L} and \mathcal{C} are differential operators applied on the unknown functions \mathbf{u} —a D dimensional quantity—evaluated at a point \mathbf{r} in a domain Ω and its boundary $\partial\Omega$, respectively; \mathbf{f}_Ω and $\mathbf{f}_{\partial\Omega}$

are known functions related to the sources of \mathbf{u} and to its boundary conditions. The description of the physical system as stated by Eq. (2.1) is known as its strong formulation since \mathbf{u} must be m -times differentiable on Ω if \mathcal{L} is a differential operator of order m [35, 36]. It is possible to relax such differentiability condition on \mathbf{u} by employing the weak formulation of the PDE system, which is an integral representation of Eq. (2.1) obtained by multiplying it by a trial function ψ and integrating on Ω [35–37]

$$W(u) = \int_{\Omega} \psi(\mathbf{r}) \{ \mathcal{L}[\mathbf{u}(\mathbf{r})] - \mathbf{f}_{\Omega} \} d\Omega = \mathbf{0}. \quad (2.2)$$

The weak formulation of the PDE system yields a weak solution to \mathbf{u} since Eq. (2.2) can be rewritten by performing s -fold integration by parts and then employing Gauss's Theorem or by employing Green's first identity [36]:

$$\int_{\Omega} \psi \nabla \cdot \mathbf{u} d\Omega = - \int_{\Omega} \nabla \psi \cdot \mathbf{u} d\Omega + \oint_{\partial\Omega} \psi \mathbf{u} \cdot \hat{\mathbf{n}} d(\partial\Omega), \quad (\text{with Gauss's Theorem}), \quad (2.3)$$

$$\int_{\Omega} \mathbf{u} \cdot \nabla \psi d\Omega = - \int_{\Omega} \psi \nabla \cdot \mathbf{u} d\Omega + \int_{\partial\Omega} \psi \mathbf{u} \cdot \hat{\mathbf{n}} d(\partial\Omega), \quad (\text{with Green's first identity}). \quad (2.4)$$

If either Eq. (2.3) or Eq. (2.4) are used s -fold on Eq. (2.2) then \mathbf{u} must be differentiable $m-s$ times instead of m , while ψ must be s times differentiable. More over, the boundary conditions imposed on \mathbf{u} must be satisfied only if they contain derivatives up to order $m-s-1$ since the conditions with derivatives of order bigger than $m-s$ are taken into account in the integrals of Eqs. (2.3) and (2.4)—and on such boundary conditions ψ must equal zero—. Thus, any solution \mathbf{u} to Eq. (2.2) is known as a weak solution since it does not holds the differentiability condition as it is required by the equivalent strong formulation [35].

Among the several methods to find an approximated solution to Eq. (2.2), the Galerkin method is one of the most common and implemented methods alongside the finite element approximation, which together form the finite element method. To ease the key ideas of the Galerkin method and the finite element approximation, the unknown function \mathbf{u} is assumed to be a scalar quantity u in the following section.

2.1.1 The Galerkin Method

To find an approximated solution to u , one option is to employ the weighted residual method, which changes the PDE system into an algebraic equation system by proposing an approximation \tilde{u} as a linear combination of N known functions ϕ_i , which differs from the exact solution u by an error e_u , that is [35–37]

$$u(\mathbf{r}) = \tilde{u}(\mathbf{r}) + e_u(\mathbf{r}), \quad \text{with} \quad \tilde{u}(\mathbf{r}) = \sum_{i=1}^N a_i \phi_i(\mathbf{r}), \quad (2.5)$$

where \tilde{u} fulfills the same boundary conditions as u at $\partial\Omega$ and a_i are N parameters to be determined¹. The values of a_i are chosen so that $e_u \ll \tilde{u}$, which may be achieved by increasing

¹The N parameters a_i are constants for equilibrium and steady-state problems while they may depend on time for transport problems [35].

N or by choosing a_i that match the exact value of u at determined points.

One particular form to the approximated solution \tilde{u} in Eq. (2.5) is known as the nodal approximation [35, 37]:

$$\tilde{u}(\mathbf{r}) = \sum_{i=1}^N u_i \phi_i(\mathbf{r}), \quad \text{with} \quad u_i = u(\mathbf{r}_i), \quad (2.6)$$

where ϕ_i are the so called interpolating—or shape—functions and u_i are coefficients that equals the exact value of the function u at N points $\mathbf{r}_j \in \Omega$, called the nodal points. From Eq. (2.6) it can be seen that the error e_u between the exact and the approximated solutions vanishes at the nodes \mathbf{r}_j and thus $\phi_i(\mathbf{r}_j) = \delta_{ij}$, with δ_{ij} the Kronecker delta.

Since \tilde{u} is an approximated solution, the evaluation of Eq. (2.6) into Eq. (2.1) equals to a residual $R_{\tilde{u}}(\mathbf{r}, \{u_i\}_{i \leq N})$ which in general is different from zero [36, 37], that is,

$$\mathcal{L}[\tilde{u}(\mathbf{r})] - f_\Omega = R_{\tilde{u}}(\mathbf{r}, \{u_i\}_{i \leq N}) \neq 0. \quad (2.7)$$

To determine the coefficients u_i , the residual $R_{\tilde{u}}$ is multiplied by a weighting—or trial—function ψ_j and integrated over Ω imposing that the integral goes to zero, that is

$$W(\tilde{u}) = \int_{\Omega} \psi_j(\mathbf{r}) R_{\tilde{u}}(\mathbf{r}, \{u_i\}_{i \leq N}) d\Omega = 0. \quad \text{with} \quad \psi_j \in \{\psi_j\}_{j \leq N}, \quad (2.8)$$

which is a set of N independent algebraic equations with N variables. It is worth noting that if the trial functions are elements of an infinite set, that is, $N \rightarrow \infty$, then Eq. (2.8) equals Eq. (2.2), and thus $u = \tilde{u}$, [35].

The weighted residual method is a family of numerical methods defined by the election of the trial functions set $\{\psi_j\}_{j \leq N}$. Some of the most common choice for the trial functions set yield the collocation method, the least-squares method, the method of moments, or the Galerkin method, given by [35, 37]:

$$\{\psi_j\}_{j \leq N} = \{\delta(\mathbf{r} - \mathbf{r}_j)\}_{j \leq N}, \quad (\text{Collocation method}), \quad (2.9a)$$

$$\{\psi_j\}_{j \leq N} = \{\partial R_{\tilde{u}} / \partial u_j\}_{j \leq N}, \quad (\text{Least-squares method}), \quad (2.9b)$$

$$\{\psi_j\}_{j \leq N} = \{x^j\}_{j \leq N}, \quad (\text{Moments method}), \quad (2.9c)$$

$$\{\psi_j\}_{j \leq N} = \{\phi_j\}_{j \leq N}, \quad (\text{Galerkin method}), \quad (2.9d)$$

where the Galerkin method sets the trial functions equal to the interpolating functions. Comparing the methods shown in Eqs. (2.9), the Galerkin method returns an approximated solution with the highest accuracy while having a moderated ease to implementation [37]. Yet, another advantage of the Galerkin method is that, for an eigenvalue problem, it guarantees real eigenvalues if the PDE system in Eq. (2.1) describes a self-adjoint operator [35, 38]. By substituting Eq. (2.9d) into Eq. (2.8), and exploiting the linearity of the differential operator \mathcal{L} , the PDE system is transformed into an algebraic problem as follows:

The Galerkin Method

$$\mathbb{A}\mathbf{u} = \mathbf{f} \quad (2.10a)$$

where the entries of the matrix \mathbb{A} , and vectors \mathbf{u} and \mathbf{f} , are

$$A_{ij} = \int \phi_i(\mathbf{r}) \mathcal{L}[\phi_j(\mathbf{r})] d\Omega, \quad u_i = u(\mathbf{r}_i), \quad \text{and} \quad f_j = \int f_\Omega \phi_j(\mathbf{r}) d\Omega. \quad (2.10b)$$

The Galerkin method is defined by the choice of trial functions according to Eq. (2.9d), which are assumed to be linearly independent so Eq. (2.10) is a solvable system of algebraic equations for the nodes u_j [37]. Additionally, for a better performance, it is recommended to choose the set of trial functions as the first N elements of a complete set of functions in the domain Ω and to meet the boundary conditions on Eq. (2.1) as exactly as possible [37]. It is also recommended for the functions ϕ_i to increase their polynomial order as the size of Ω grows since the integral in Eq. (2.10b) can be calculated with higher accuracy if methods as quadratures are employed [37].

The Galerkin method returns an approximated solution \tilde{u} to u , in the weak sense, as a linear combination of the interpolating functions $\{\phi_i\}_{i \leq N}$ so long the error e_u can be neglected for all points in the domain Ω . Such solution is determined by inverting the matrix \mathbb{A} in Eq. (2.10) thus, a crucial step is to find the set $\{\phi_i\}_{i \leq N}$ of functions to solve the problem in Ω that follows the boundary conditions on $\partial\Omega$. From a computational approach, the required computing time and resources increase as Ω does, therefore requiring the cardinality of the sets $\{\psi_j\}_{j \leq N}$ and $\{\phi_i\}_{i \leq N}$ to increase as well [35]. To overcome this, one alternative is to divide Ω into M smaller subdomains allowing for low cardinality interpolating functions to solve Eq. (2.8) in each subdomain. This method is known as the finite element approximation and it is discussed in the following Section.

2.1.2 The Finite Element Approximation

The finite element approximation allows the use of low order interpolating functions by defining the subdomains Ω_k such that

$$\bigcup_{k=1}^M \Omega_k = \Omega \quad \text{and} \quad \bigcap_{k=1}^M \Omega_k = \emptyset, \quad (2.11)$$

that is that all Ω_k together represent the original domain Ω and that they do not overlap nevertheless, the boundaries of the finite elements are shared by neighboring elements [35]. Then, the finite element approximation restricts \tilde{u}_k —the nodal approximation on each subdomain— to depend only on the nodal points on Ω_k and on its boundary $\partial\Omega_k$, while all \tilde{u}_k must be continuous across $\partial\Omega_k$ and obey the differentiability condition they are bound to, whether the strong or weak formulation is employed [35].

A finite element Ω_k is a subdomain of Ω following Eq. (2.11) but its formal definition requires Ω_k to be a manifold embedded in Ω , as well as to chose a polynomial functions space on

Ω_k , and to define a collection of N_k linear functionals \mathcal{F}_{ℓ_k} on Ω_k [36]. The description of Ω_k as a manifold determines its geometrical properties such as dimensionality, shape and curvature, while the polynomial functions space sets the order of the interpolating functions $\{\phi_{i_k}\}_{i_k \leq N_k}$. By applying ϕ_{i_k} to \mathcal{F}_{ℓ_k} , a system of N_k algebraic equations is obtained:

$$\mathcal{F}_{\ell_k}[\phi_{i_k}] = \delta_{\ell_k i_k}, \quad (2.12)$$

from which the interpolating functions are determined. Since the N_k linear functional imposes conditions on the interpolating functions, the N_k corresponds to the number of degrees of freedom of the finite element [36].

The finite element corresponds to a particular way of discretization of the domain Ω and thus it is convenient to define the manifold Ω_k by its geometrical nodes \mathbf{r}_{m_k} , which are a finite collection of points in Ω_k . In Fig. 2.1 examples² of common finite elements in one, two and three dimensions are shown: a straight line segment, a triangular surface and a tetrahedron [35]. The markers correspond to the geometrical nodes in Ω_k , from which the red markers correspond to the geometrical nodes that define the shape of Ω_k , since the lines joining two of them are the edges of the finite elements in two and three dimensions. The finite elements in Fig. 2.1a) are known as reference elements since they have boundaries with no curvature and their geometrical nodes on its edges are equally spaced [35, 36]. Even so, the finite elements are, in general, curvilinear in shape, as shown in Fig. 2.1b), which may be preferred over the reference elements for Ω with no Cartesian symmetries. It is possible to perform a transformation $T : T(\xi) \rightarrow \mathbf{r}$ on the reference elements (ξ) to reshape it into the so-called real-space elements (\mathbf{r}), which correspond to the physical space where the Eq. (2.8) is to be solved [35, 37]. Let us recall that the choice of finite elements with straight or curvilinear boundaries is related to the discretization method of the domain Ω . For example, were Ω a cylinder in 3D, the use of finite elements with straight boundaries arises an error due to truncation of Ω at its boundary, which can be minimized by increasing the number of finite elements, while curvilinear finite elements may fill such space without increasing the number of finite elements.

The transformation T is a change of coordinates from the coordinate system ξ of the reference finite element into the real-space system \mathbf{r} . The use of Eq. (2.12) in the reference elements yields different kind of interpolating functions, which can be employed to solve the weak formulation of a PDE system [Eq. (2.8)] by transforming the derivatives in the real space coordinate system by means of the Jacobian matrix \mathbb{J} , whose elements are $J_{ij} = \partial \xi_i / \partial r_j$, and its determinant, the Jacobian, that is [35, 37]:

$$\frac{\partial}{\partial r_i} = \frac{\partial \xi_i}{\partial r_j} \frac{\partial}{\partial \xi_j} \quad \text{and} \quad d\Omega_k \rightarrow \det[\mathbb{J}] d\xi_k. \quad (2.13)$$

Equation (2.13) sets a constriction into the discretization of the original domain Ω and its partition into finite elements, since the Jacobian must be non singular —different from zero— in all points in Ω_k , meaning that the transformation T of the reference element into the real-space finite element is bijective [35, 37]. To avoid singular points in Ω_k , the real-space finite element must not be deformed considerably when transformed into the reference element [35].

²Even though the elements shown in Fig. 2.1 are triangles (2D) and triangular pyramids (3D), their shape can also be composed by squares and prisms; see [35] for a more detailed list.

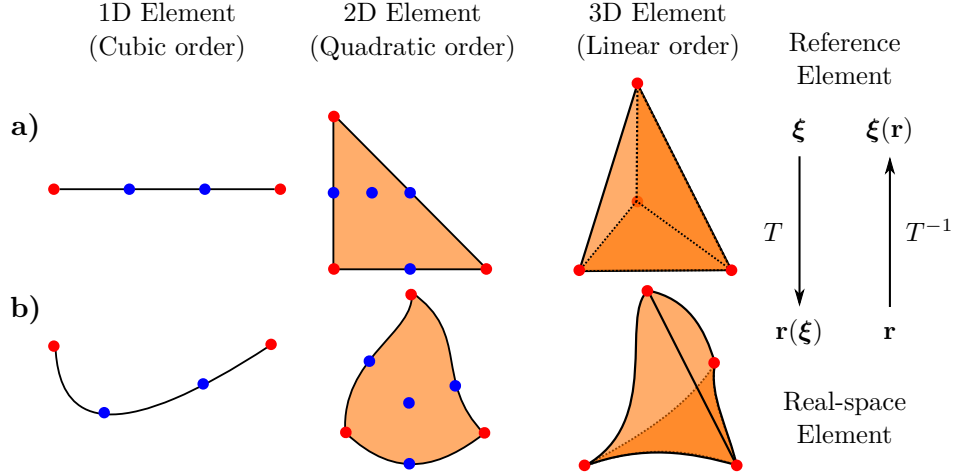


Fig. 2.1: **a)** Reference and **b)** real-space finite elements for one (line segment), two (triangular surface) and three (tetrahedron) dimensional domains. The geometrical nodes on each element are signalized by the blue markers and their edges correspond to the lines between the red markers; the number of nodes along each edge defines the order of the element. The transformation T reshapes the reference finite element from its coordinate system ξ into a real-space element r .

To build the interpolating functions $\phi_{i_k}(\xi)$ in the reference finite element, the polynomial functions space on Ω_k must be chosen by selecting the number of geometrical nodes found along the edges [36], so that the boundary conditions are met. If there are m geometrical nodes on each edge, the finite element is said to be of order $m - 1$ since a polynomial of order $m - 1$ is guaranteed to pass through the values given the m nodes. For example, the reference finite elements in Fig. 2.1a) correspond to a cubic order 1D finite element (three geometrical nodes along the edges), a quadratic order triangular finite element (2D shape with three nodes along the edges), and a linear tetrahedral finite element (3D volume with four triangular faces and two nodes at each edge).

Once the polynomial functions space on the manifold Ω_k is set, this can be spanned by the set of interpolating functions $\phi_{i_k}(\xi)$, that are determined by means of the N_k linear functionals \mathcal{F}_ℓ [36]. The choice of the linear functionals gives rise to different sets of interpolating functions and thus different families of finite elements. For example, the linear functional given by

$$\mathcal{F}_{\ell_k}^L[f(\xi)] = f(\xi_{\ell_k}), \quad (2.14)$$

with ξ_{ℓ_k} the ℓ_k -th geometrical node from a collection of n_k in the reference finite element, defines the Lagrange finite element family since the interpolating functions obtained by employing Eqs. (2.12) and (2.14) are the Lagrange polynomials [35–37]. The functional $\mathcal{F}_{\ell_k}^L$ is a point evaluation in the $N_k = n_k$ geometrical nodes, which imposes no condition on the derivatives of ϕ_{i_k} at the boundary of Ω_k , therefore the Lagrange finite element family returns a set of $N_k = n_k$ interpolating functions with no continuous first derivative between finite elements. One linear functional which does return interpolating functions with continuous first derivatives is the following:

$$\mathcal{F}_\ell^H[f(\xi)] = f(\xi_{\ell_k}) \quad \text{and} \quad \mathcal{F}_{\ell'_k}^H[f(\xi)] = \hat{\mathbf{t}} \cdot \nabla f(\xi_{\ell'_k}) = 0, \quad (2.15)$$

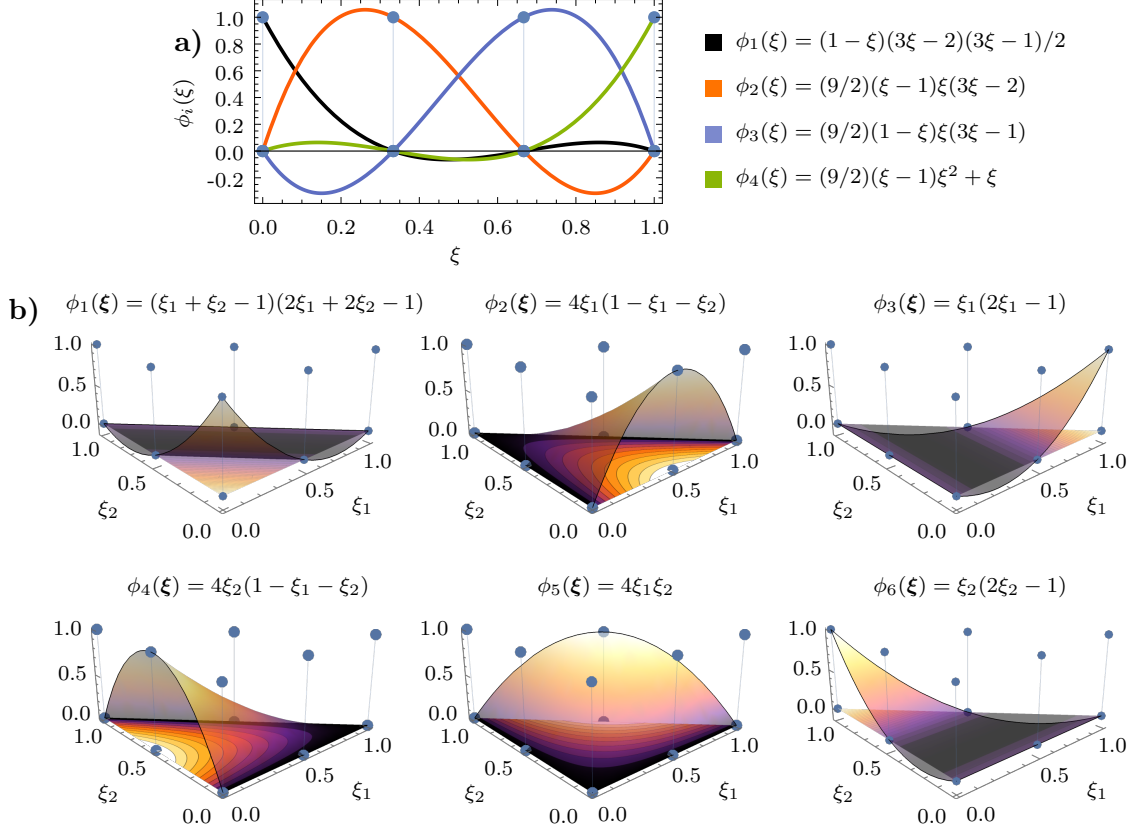


Fig. 2.2: Interpolating functions of **a)** a Lagrange cubic 1D reference finite element and **b)** a serendipity Lagrange quadratic 2D triangular reference element. The markers corresponds to the evaluation of the linear functionals [Eqs. (2.12) and (2.14)] on the interpolating functions on each case.

with ξ_{ℓ_k} one of the n_k geometric nodes in Ω_k , $\xi_{\ell'_k}$ one of the n'_k geometric nodes at vertices of Ω_k , and $\hat{\mathbf{t}}$ is a unit vector parallel to its edges [36]. The functional in Eq. (2.15) gives rise to the Hermite finite element family since the resulting interpolating functions are the Hermite polynomials, which allow for a solution on Ω 1-differentiable due to its $N_k = n_k + n'_k$ degrees of freedom [35, 36]. The Lagrange and the Hermite finite element families are two of the most common and simple nevertheless, one can build yet another family known as the *serendipity* finite element family if the geometrical nodes outside the boundary of Ω_k are not considered in Eq. (2.14) [37]. In Fig. 2.2 the interpolating functions for one and two dimensional finite elements under the Lagrange linear functional [Eq. (2.14)] are shown: a one dimensional cubic finite element [Fig. 2.2a)] and a serendipity triangular reference finite element of quadratic order [Fig. 2.2b)].

2.2 Numerical Approach to the Light Scattering Problem

In Chapter 1 the general theory of isolated scatterers in a non-absorbing media was developed and the particular case of spherical scatterers was approached analytically. In order to solve the light

scattering problem through numerical methods and thus allowing for more complex geometries, the fundamentals of the Finite Element Method (FEM) were introduced in Section 2.1. Hereby, it is discussed the implementation of the FEM into the light scattering problem to find numerical approximations, in the weak sense, to the electric field $\mathbf{E}(\mathbf{r})$ in finite domain Ω . Due to the vectorial nature of the electric field, the interpolating—and trial—functions employed in the Galerkin method [Eq. (2.10)] are chosen to be vectorial functions instead of scalar functions, since a family of vectorial finite element can be chosen so the boundary conditions of the electric fields are easily met. In this Section, the strong and weak formulations of the scattering of light are developed by employing such vectorial interpolating functions, and the corresponding finite elements are introduced, as well as the matrix representation of the light scattering problem. Lastly, additional conditions are imposed into the light scattering problem in order to solve it numerically through the FEM.

2.2.1 Strong and Weak Formulations

The scattering light problem addressed in Chapter 1 corresponds to a steady-state problem in a domain Ω whose optical properties are characterized by its electric permittivity ε and magnetic permeability μ , which in general are complex functions of the angular frequency ω . To obtain the strong formulation of the light scattering problem, let us assume harmonic time dependent electric $\mathcal{E}(\mathbf{r}, t)$ and magnetic fields $\mathcal{H}(\mathbf{r}, t)$:

$$\mathcal{E}(\mathbf{r}, t) = \mathbf{E}(\mathbf{r}) \exp(-i\omega t) \quad \text{and} \quad \mathcal{H}(\mathbf{r}, t) = \mathbf{H}(\mathbf{r}) \exp(-i\omega t), \quad (2.16)$$

with $\mathbf{E}(\mathbf{r})$ and $\mathbf{H}(\mathbf{r})$ complex valued vectors. For harmonic time dependent EM fields in optical linear media, the Maxwell's equation are rewritten as [22]

$$\nabla \cdot (\varepsilon \mathbf{E}) = \rho_{\text{ext}}, \quad (\text{Electric Gauss's law}), \quad (2.17a)$$

$$\nabla \cdot \mathbf{B} = 0, \quad (\text{Magnetic Gauss's law}), \quad (2.17b)$$

$$\nabla \times \mathbf{E} = i\omega \mu \mathbf{H}, \quad (\text{Faraday-Lenz's law}), \quad (2.17c)$$

$$\nabla \times (\mu \mathbf{H}) = \mathbf{J} - i\omega \varepsilon \mathbf{E}, \quad (\text{Ampère-Maxwell's law}), \quad (2.17d)$$

where ρ_{ext} is the external volumetric charge density, \mathbf{J} is the volumetric current density, and $\mathbf{B} = \mu \mathbf{H}$. The volumetric current density is given by [22]

$$\mathbf{J}(\mathbf{r}, t) = \mathbf{J}_{\text{ext}}(\mathbf{r}) \exp(-i\omega t) + \sigma \mathbf{E}(\mathbf{r}) \exp(-i\omega t), \quad (2.18)$$

where \mathbf{J}_{ext} corresponds to the external current density, σ is the frequency dependent conductivity of the domain Ω and the term $\sigma \mathbf{E}(\mathbf{r}) \exp(-i\omega t)$ corresponds to the induced current density that arises from an Ohmic response of the domain Ω .

The Maxwell's equations can be decouple to avoid working with two unknown functions, yielding [22, 36, 38, 39]

$$\nabla \times [\mu^{-1} \nabla \times \mathbf{E}] - (i\omega \sigma + \omega^2 \varepsilon) \mathbf{E} = i\omega \mathbf{J}_{\text{ext}}, \quad (2.19)$$

which is another formulation of the vectorial Helmholtz equation [Eq. (1.13)]. In the absence of

an external current and charge densities, Eq. (2.19) becomes the Maxwell eigenvalue problem [36], which corresponds to the strong formulation of the light scattering problem alongside the boundary conditions stated by Maxwell's equations [Eqs. (2.17)]. Therefore, the strong formulation of the light scattering problem is given by [36, 38, 39]

Maxwell's Eigenvalue Problem and Boundary Conditions (Strong Formulation)

$$\nabla \times [\mu^{-1} \nabla \times \mathbf{E}] - \kappa^2 \mathbf{E} = \mathbf{0}, \quad \text{with } \kappa^2 = (i\omega\sigma + \omega^2 \epsilon), \quad (2.20a)$$

$$\hat{\mathbf{n}} \times \mathbf{E}(\mathbf{r}) \Big|_{\partial\Omega} = \mathbf{E}_D, \quad (\text{Dirichlet Boundary Condition}), \quad (2.20b)$$

$$\mu^{-1} \nabla \times \mathbf{E} \times \hat{\mathbf{n}} \Big|_{\partial\Omega} = \mathbf{E}_N, \quad (\text{Neumann Boundary Condition}), \quad (2.20c)$$

with $\partial\Omega$ the boundary of Ω and $\hat{\mathbf{n}}$ a normal vector to $\partial\Omega$. A Dirichlet type boundary condition is described in Eq. (2.20b) while the Eq. (2.20c) corresponds to Neumann type boundary condition. Both of such boundary conditions are equivalent to Eq. (1.26) in Section 1.2.2 when $\mathbf{E}_D = \mathbf{E}_N = \mathbf{0}$.

To build the weak formulation of the light scattering problem let us choose a set of N linearly independent vectorial interpolating functions $\{\boldsymbol{\eta}_j\}_{j \leq N}$. If the Eq. (2.20a) is projected onto one interpolating function $\boldsymbol{\eta}_j$ and the result is integrated in the domain Ω , one obtains

$$\int_{\Omega} \boldsymbol{\eta}_j \cdot \nabla \times [\mu^{-1} \nabla \times \mathbf{E}] d\Omega = \int_{\Omega} \kappa^2 \boldsymbol{\eta}_j \cdot \mathbf{E} d\Omega. \quad (2.21)$$

The left-hand side of Eq. (2.21) can be simplified by employing the vectorial identity $\nabla \cdot (\mathbf{A} \times \mathbf{B}) = \mathbf{B} \cdot \nabla \times \mathbf{A} - \mathbf{A} \cdot \nabla \times \mathbf{B}$, with $\mathbf{A} = \boldsymbol{\eta}_j$ and $\mathbf{B} = \mu^{-1} \nabla \times \mathbf{E}$, and performing a one-fold integration by parts, yielding

$$\begin{aligned} \int_{\Omega} \boldsymbol{\eta}_j \cdot \nabla \times [\mu^{-1} \nabla \times \mathbf{E}] d\Omega &= \int_{\Omega} (\mu^{-1} \nabla \times \mathbf{E}) \cdot (\nabla \times \boldsymbol{\eta}_j) d\Omega \\ &\quad - \oint_{\partial\Omega} [\boldsymbol{\eta}_j \times (\mu^{-1} \nabla \times \mathbf{E})] \cdot \hat{\mathbf{n}} d(\partial\Omega), \end{aligned} \quad (2.22)$$

where the last term in the right-hand side is obtained by the Gauss's Theorem. Substituting Eq. (2.22) into Eq. (2.21) and applying the boundary condition given by Eq. (2.20c), the Maxwell's eigenvalue problem in its weak formulation is obtained:

Maxwell's Eigenvalue Problem and Boundary Conditions (Weak Formulation)

$$\int_{\Omega} \{(\mu^{-1} \nabla \times \mathbf{E}) \cdot (\nabla \times \boldsymbol{\eta}_j) - \kappa^2 \cdot \mathbf{E} \cdot \boldsymbol{\eta}_j\} d\Omega - \oint_{\partial\Omega} (\boldsymbol{\eta}_j \times \mathbf{E}_N) \cdot \hat{\mathbf{n}} d(\partial\Omega) = 0, \quad (2.23a)$$

$$\hat{\mathbf{n}} \times \mathbf{E}(\mathbf{r}) \Big|_{\partial\Omega} = \mathbf{E}_D. \quad (2.23b)$$

The weak formulation problem of light scattering [Eq. (2.23a)] in the finite element approximation is reduced to the algebraic system of equations given by the Galerkin method in

each of the M subdomains Ω_k of Ω , given by [36, 38]

$$\mathbb{A}\mathbf{e} = \mathbf{0}, \quad (2.24a)$$

with

$$A_{ij} = \int_{\Omega_k} \left\{ (\mu^{-1} \nabla \times \boldsymbol{\eta}_i) \cdot (\nabla \times \boldsymbol{\eta}_j) - \kappa^2 \cdot \boldsymbol{\eta}_i \cdot \boldsymbol{\eta}_j \right\} d\Omega_k - \oint_{\partial\Omega} (\boldsymbol{\eta}_j \times \mathbf{E}_N) \cdot \hat{\mathbf{n}} d(\partial\Omega), \quad (2.24b)$$

where A_{ij} are the matrix elements of \mathbb{A} and \mathbf{e} is the vector containing the N coefficients of the linear combination of the interpolating function $\boldsymbol{\eta}_j$ that results into an approximated solution $\tilde{\mathbf{E}}(\mathbf{r}) = \sum_i e_i \boldsymbol{\eta}_j(\mathbf{r})$ to the electric field. The choice of the coefficients e_i , its physical interpretation, and the set of the vectorial interpolating functions is discussed in the next section.

2.2.2 The Nédélec Finite Element Family

In order to perform the vectorial finite element approximation in Eq. (2.24) equivalently to the scalar method in Eq. (2.10b), an approximation $\tilde{\mathbf{E}}$ to the electric field \mathbf{E} is proposed as a linear combination of the vectorial interpolating functions $\boldsymbol{\eta}_j$ with scalar coefficients e_i . If the nodal approximation [Eq. (2.6)] were used for the linear combination setting the coefficients e_i as the exact solution of each component of electric field at some nodal points into the finite element Ω_k , not only the boundary condition in Eq. (2.23b) might be difficult to meet [36, 38], but also non-physical solutions may arise [39]. Therefore, instead of employing the nodal approximation, the expression of $\tilde{\mathbf{E}}$ in a finite element Ω_k of Ω is given by [36]

$$\tilde{\mathbf{E}}(\mathbf{r}) = \sum_{i_k} e_{i_k} \boldsymbol{\eta}_{i_k}(\mathbf{r}), \quad \text{with} \quad e_i = \hat{\mathbf{t}}_{i_k} \cdot \mathbf{E}(\mathbf{r} \in E_{i_k}), \quad (2.25)$$

where E_{i_k} is the i_k -th edge in Ω_k , $\hat{\mathbf{t}}_{i_k}$ is a unitary vector parallel to E_{i_k} and e_{i_k} is the exact value of the tangential component of the electric field on it. If the interpolating functions $\boldsymbol{\eta}_{i_k}$ in the element Ω_k are to follow Eq. (2.20b), they must have a continuous tangential components across $\partial\Omega_k$, while no special requirement is asked for their normal component on $\partial\Omega_k$. A special family of vectorial—or edge—reference finite elements are given by the linear functional [36]

$$\mathcal{F}_{i_k}^N[\boldsymbol{\eta}_{\ell_k}(\xi)] = \frac{1}{|E_{i_k}|} \left(\int_{E_{i_k}} \hat{\mathbf{t}}_{i_k} \cdot \boldsymbol{\eta}_{\ell_k}(\xi) d(\partial\Omega_k) \right)^{1/2} = \delta_{i_k \ell_k}, \quad (2.26)$$

which is the square-root mean value of the interpolating function along the edge E_{i_k} . The reference finite elements obtained from Eq. (2.26) are known as the Nédélec finite element of lowest order since their only degree of freedom is on the edges of the finite element [40]. For triangular and tetrahedral finite elements, a closed formula for $\boldsymbol{\eta}_{i_k}$ is given by [36, 38, 39]

$$\boldsymbol{\eta}_{i_k} = |E_{i_k}| (\phi_{j_k} \nabla \phi_{\ell_k} - \phi_{\ell_k} \nabla \phi_{j_k}), \quad (2.27)$$

with cyclic permutation of the indices $\{i_k, j_k, \ell_k\}$, corresponding to the vertices of triangular surfaces forming the edges of the reference element. The scalar functions ϕ_{j_k} in Eq. (2.27) are the interpolating functions obtained with the Lagrange linear operator [Eq. (2.14)] applied on Ω_k at the vertices. Nédélec finite elements of higher orders can be obtained if, additionally, more degrees

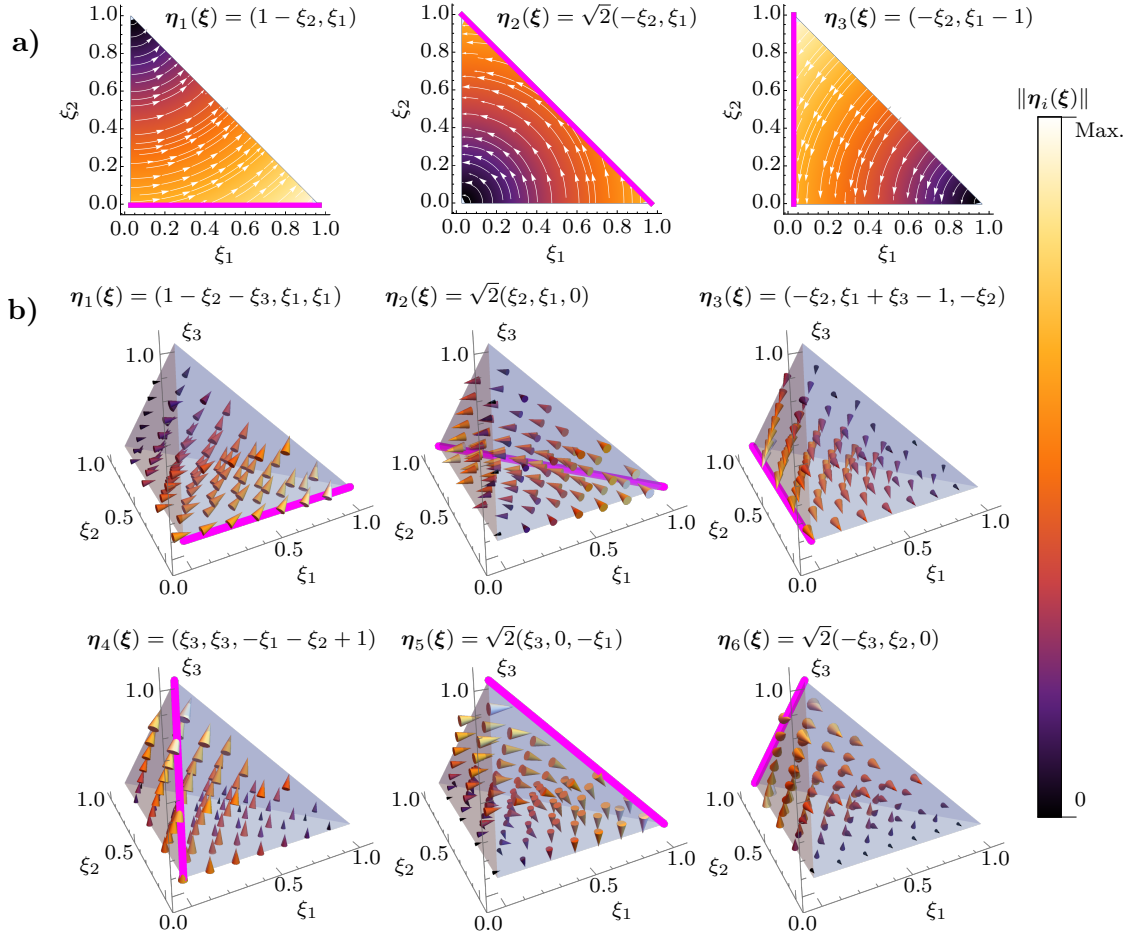


Fig. 2.3: Interpolating functions for the lowest order Nédélec **a)** pyramidal (2D) and **b)** tetrahedral (3D) reference finite elements. The thick magenta lines correspond to the edges where the linear functional of the Nédélec family [Eq. (2.26)] is evaluated.

of freedom are set to the faces and the volume of Ω_k [40] nevertheless, their implementation is of greater difficulty and thus, less common [36, 38]. An example of Nédélec finite elements of lowest order are shown in Fig. 2.3a) for a triangular finite element and in Fig. 2.3b) for a tetrahedral finite element; the edge where Eqs. (2.26) and (2.27) are applied to is shown with a thick magenta line in all cases. In all interpolating functions (2D and 3D) it can be seen that all functions η_i are divergenceless inside the finite elements and their components parallel to the edges are zero except at the associated i_k -th edge. Therefore, the Nédélec finite elements are suited to solve Eq. (2.23) by following an exact evaluation for a given boundary condition, and by following the electric Gauss's law with no sources.

2.2.3 Open Boundary Conditions

In the previous Sections the theory behind the FEM and how it is implemented into the light scattering problem [Eqs. (2.23)] was discussed. A special kind of boundary conditions, known as the Absorbing Boundary Conditions (ABC), are introduced in this Section since numerical methods, such as the FEM, require the domain Ω , where the electromagnetic fields are to be

solved, to be of finite size [38, 39] while in the scattering problem an infinite—or open—boundary is considered. The ABCs are required since they simulate an open domain with a finite domain Ω by imposing that there are no reflections back into the domain due to the interaction between its boundary $\partial\Omega$ and the scattered electric field [38, 39, 41]. Two of the most common ABCs are the Sommerfeld’s radiation condition—which describes the behavior of the electric field in the far-field at $\partial\Omega$ —and the Perfectly Matching Layer (PML)—which is a thin layer that covers Ω and acts as a non-reflective material—[38]. Both of the previous ABCs are preferred over other kinds of ABC since they do not need the domain Ω to grow considerably and thus are optimized for the FEM while its implementation faces no extra difficulties [38].

2.2.3.1 Sommerfeld’s Radiation Condition

In 1912 Arnold Sommerfeld first stated its radiation condition in order to guarantee the uniqueness of the solution to the scalar Helmholtz equation [Eq. (1.15)] applied to the scalar potential $\phi = \phi(\mathbf{r})$ [42]. Its condition for uniqueness can be found by substituting the scalar potential, generated by bounded sources, and the Green’s function to the scalar Helmholtz equation in a 3D domain Ω , given by [22, 27]

$$(\nabla^2 + k^2)g(\mathbf{r}|\mathbf{r}') = \delta(\mathbf{r} - \mathbf{r}') \iff g(\mathbf{r}|\mathbf{r}') = \frac{\exp[i\mathbf{k} \cdot (\mathbf{r} - \mathbf{r}')] }{\|\mathbf{r} - \mathbf{r}'\|}, \quad (2.28)$$

into Green’s second identity³, leading to

$$4\pi\phi(\mathbf{r}) = \oint_{\partial\Omega} \frac{\exp[i\mathbf{k} \cdot (\mathbf{r} - \mathbf{r}')] }{\|\mathbf{r} - \mathbf{r}'\|^2} \phi(\mathbf{r}') d^2r + \oint_{\partial\Omega} \frac{d^2r}{\|\mathbf{r} - \mathbf{r}'\|^2} \left[\|\mathbf{r} - \mathbf{r}'\| \left(\frac{\partial\phi(\mathbf{r})}{\partial r} - ik \cdot \hat{\mathbf{e}}_r \phi(\mathbf{r}) \right) \right]. \quad (2.29)$$

The boundary condition that the potential ϕ must decay to zero as $r \rightarrow \infty$ sets Eq. (2.29) equal to zero, which is hold immediately by the left hand side of Eq. (2.29). The first integral in the right hand side of Eq. (2.29) equals zero since $\phi(r \rightarrow 0) = 0$ while $d^2r/\|\mathbf{r} - \mathbf{r}'\| \approx d^2r/r^2$ remains bounded, thus the term between brackets in the second integral must equal to zero in the far-field regime [42], that is

$$\lim_{r \rightarrow \infty} r \left(\frac{\partial\phi(\mathbf{r})}{\partial r} - ik\phi(\mathbf{r}) \right) = 0, \quad (2.30)$$

where $\|\mathbf{r} - \mathbf{r}'\| \approx r$ and $\mathbf{k} = k\hat{\mathbf{e}}_r$. The Eq. (2.30) is known as the Sommerfeld’s radiation condition since it states that in the far-field there can only be outgoing waves that decay uniformly in all directions [38, 39, 42].

A generalization of the Eq. (2.30) to the electric field \mathbf{E} and the \mathbf{H} field, both of which are solution to the vectorial Helmholtz equation [Eq. (1.13)], can be obtained by substituting into the Green’s second identity for vector fields⁴ the electric field \mathbf{E} —or magnetic field \mathbf{H} —and the vectorial Green’s function [42, 44, 45]. Yet, an equivalent derivation is achieved by separating the

³Let ψ and ϕ be C^2 in Ω , then $\int_{\Omega} (\psi \nabla^2 \psi - \phi \nabla^2 \phi) d^3r = \oint_{\partial\Omega} \hat{\mathbf{n}} \cdot (\psi \nabla \phi - \phi \nabla \psi) d^2r$, with $\hat{\mathbf{n}}$ a normal vector to the boundary $\partial\Omega$ [27].

⁴This can be obtained if Eq. (2.19) is subtracted by itself interchanging $\boldsymbol{\eta}_j$ and \mathbf{E} and setting $\boldsymbol{\eta}_i(\mathbf{r}) = \mathbf{n}g(\mathbf{r}|\mathbf{r}')$ as explained by Stratton and Chu [43].

electromagnetic fields into two contributions and introducing two vectorial potentials according to the origin of their sources: magnetic and electric charges and currents induced into a bounded volume [38, 39]. Under such considerations, the electromagnetic fields can be written as:

$$\mathbf{E} = \mathbf{E}_e + \mathbf{E}_m \quad \text{and} \quad \mathbf{H} = \mathbf{H}_e + \mathbf{H}_m, \quad (2.31)$$

where the subscript ‘e’ (‘m’) stands for the electric (magnetic) sources [38]. Substitution of Eqs. (2.31) into the time harmonic Maxwell’s equations [Eqs. (2.17)] leads to

$$\nabla \cdot (\varepsilon \mathbf{E}_e) = \rho_{\text{ext}}, \quad (2.32a)$$

$$\nabla \cdot (\mu \mathbf{H}_e) = 0, \quad (2.32b)$$

$$\nabla \times \mathbf{E}_e = i\omega \mu \mathbf{H}_e, \quad (2.32c)$$

$$\nabla \times \mathbf{H}_e = \mathbf{J}_{\text{ext}} - i\omega \varepsilon \mathbf{E}_e, \quad (2.32d)$$

where ρ_m and \mathbf{J}_m are induced charge and current densities due to the magnetization of the sources [38]. From the magnetic Gauss’s law applied on $\mu \mathbf{H}_e$, it is defined the vector potential \mathbf{A} and, analogously, the vector potential \mathbf{F} arises from the electric Gauss’s law on $\varepsilon \mathbf{E}_m$ [38]. Then, scalar potentials ϕ_e and ϕ_m for \mathbf{E}_e and \mathbf{H}_m are obtained from the Faraday-Lenz’s law and the Ampère-Maxwell’s law applied on them, accordingly [38]. If the electric scalar and vector potentials are chosen so that they follow the Lorenz gauge, and the same is imposed for the magnetic scalar and vector potential, that is $\nabla \cdot \mathbf{A} = -i\omega \mu \varepsilon \phi_e$ and $\nabla \cdot \mathbf{F} = -i\omega \mu \varepsilon \phi_m$ [27], then the EM fields are given by

$$\mathbf{E} = -\frac{\nabla[\nabla \cdot \mathbf{A}]}{i\omega \varepsilon \mu} + i\omega \mathbf{A} + \frac{1}{\varepsilon} \nabla \times \mathbf{F} \quad \text{and} \quad \mathbf{H} = -\frac{\nabla[\nabla \cdot \mathbf{F}]}{i\omega \varepsilon \mu} + i\omega \mathbf{F} + \frac{1}{\mu} \nabla \times \mathbf{A}, \quad (2.33)$$

where the vectorial potentials \mathbf{A} and \mathbf{F} are also solution to Helmholtz equation on each component and thus can be expressed as [38]

$$\mathbf{A} = \frac{\mu}{4\pi} \int_{\Omega} \mathbf{J}_{\text{ext}} \frac{\exp[i\mathbf{k} \cdot (\mathbf{r} - \mathbf{r}')]}{\|\mathbf{r} - \mathbf{r}'\|} d\Omega' \quad \text{and} \quad \mathbf{F} = \frac{\varepsilon}{4\pi} \int_{\Omega} \mathbf{J}_m \frac{\exp[i\mathbf{k} \cdot (\mathbf{r} - \mathbf{r}')]}{\|\mathbf{r} - \mathbf{r}'\|} d\Omega'. \quad (2.34)$$

In the far-field regime it follows that $\|\mathbf{r} - \mathbf{r}'\|^{-1} \approx r^{-1}$ and $\mathbf{k} \cdot \mathbf{r} = kr$ [22, 27], therefore

$$\mathbf{A} = \frac{\mu \exp(ikr)}{4\pi r} \mathbf{N}, \quad \text{with} \quad \mathbf{N} = \int_{\Omega} \mathbf{J}_{\text{ext}} \exp(-i\mathbf{k} \cdot \mathbf{r}') d\Omega', \quad (2.35a)$$

$$\mathbf{F} = \frac{\varepsilon \exp(ikr)}{4\pi r} \mathbf{L}, \quad \text{with} \quad \mathbf{L} = \int_{\Omega} \mathbf{J}_m \exp(-i\mathbf{k} \cdot \mathbf{r}') d\Omega', \quad (2.35b)$$

and that also the operator ∇ acts as $\nabla \rightarrow i\mathbf{k} = i\mathbf{k}\mathbf{e}_r$ since the electric field can be written as a plane traveling in the \mathbf{k} direction [22, 38]. Substituting Eqs. (2.35) into Eq. (2.33) leads to the following expressions for the electromagnetic fields in the far-field regime [38]:

$$\lim_{r \rightarrow \infty} \mathbf{E} = -ik \frac{\exp(ikr)}{4\pi r} \left[\hat{\mathbf{e}}_r \times \mathbf{L} - \sqrt{\frac{\mu}{\varepsilon}} \left(\mathbf{N} - (\hat{\mathbf{e}}_r \cdot \mathbf{N}) \hat{\mathbf{e}}_r \right) \right], \quad (2.36a)$$

$$\lim_{r \rightarrow \infty} \mathbf{H} = ik \frac{\exp(ikr)}{4\pi r} \left[\sqrt{\frac{\varepsilon}{\mu}} \left(\mathbf{L} - (\hat{\mathbf{e}}_r \cdot \mathbf{L}) \hat{\mathbf{e}}_r + \hat{\mathbf{e}}_r \times \mathbf{N} \right) \right], \quad (2.36b)$$

where the dispersion relation $k^2 = \omega^2 \mu \varepsilon$ was employed. From Eq. (2.36) it can be seen that the

2. THE FINITE ELEMENT METHOD

EM fields in the far-field regime have no radial components and, by calculating the cross product $\hat{\mathbf{e}}_r \times \mathbf{E}$ in the far-field, and comparing with Eq. (2.36b), one obtains

$$\lim_{r \rightarrow \infty} \left(\hat{\mathbf{e}}_r \times \mathbf{E} - \sqrt{\frac{\mu}{\epsilon}} \mathbf{H} \right) = \mathbf{0}, \quad (2.37)$$

which states that the electric field is perpendicular to the direction of propagation and to the \mathbf{H} field in the far-field and that their amplitudes have a fixed ratio of $\sqrt{\mu/\epsilon}$, known as the impedance of the medium [38, 42]. Lastly, Eq. (2.37) can be rewritten in terms of only \mathbf{E} with aide of the Faraday-Lenz's law and the dispersion relation for a plane wave, which yields the generalization of the Eq. (2.30)

Generalized Sommerfeld or Silver-Müller Radiation Condition

$$\lim_{r \rightarrow \infty} r(\nabla \times \mathbf{E} - ik\hat{\mathbf{e}}_r \times \mathbf{E}) = \mathbf{0}, \quad (2.38)$$

which is also known as the Silver-Müller radiation condition [44, 45].

The implementation of the light scattering problem [Eq. (2.23)] into numerical methods, such as the FEM, has the disadvantage that it is a problem solved in an unbounded, or an open, domain. Nevertheless, the evaluation of Eq. (2.38) into $\partial\Omega$ guarantees that the obtained solution reproduces that of the light scattering [38, 39]. Since the Sommerfeld's radiation condition is a non-homogeneous Neumann boundary condition, it requires Eq. (2.38) to be evaluated at a surface, with a normal vector $\hat{\mathbf{n}}$. Due to its integration on $\partial\Omega$, Sommerfeld's radiation condition is mostly used when the scatterer is small relative to Ω and when the scattered electric field normally illuminates the boundary [38, 39]. Were any of these conditions are not met, another ABC must be implemented.

2.2.3.2 Perfectly Matching Layer

The Perfectly Matching Layer (PML) is an Absorbing Boundary Condition (ABC) described by a mathematical domain Ω_{PML} [38] that surrounds Ω , where Eq. (2.23) is to be solved, which has the property that any reflection on its boundary is damped [38, 39, 41]. The PML was originally developed by Berenger [46] in 1994 as a highly absorbing media for finite differences time domain simulations and then it was proposed as a *complex coordinate stretching* viewpoint⁵ [41], thus attributing the non-reflectivity of the PML to its geometric properties. The FEM solution to the scattering problem with time harmonic dependency, such as described in Eq. (2.23), exploits the later approach since the introduction of the PML does not modify the method [38].

To determine which conditions are needed for the PML to damp all reflections in Ω , let us use stretched coordinates on the PML domain Ω_{PML} where it is assumed that the far-field approximation of the electromagnetic fields is valid. Thus, the gradient in such coordinate system

⁵The complex coordinate stretching approach to the PML for FEM simulations employs a curvilinear system with complex evaluated scale factors to suppress any non-physical reflections.

can be written as

$$\nabla_s \equiv \left(\frac{\hat{\mathbf{e}}_x}{s_x} \frac{\partial}{\partial x} + \frac{\hat{\mathbf{e}}_y}{s_y} \frac{\partial}{\partial y} + \frac{\hat{\mathbf{e}}_z}{s_z} \frac{\partial}{\partial z} \right) \rightarrow \mathbf{k} = \frac{k_x}{s_x} \hat{\mathbf{e}}_x + \frac{k_y}{s_y} \hat{\mathbf{e}}_y + \frac{k_z}{s_z} \hat{\mathbf{e}}_z, \quad (2.39a)$$

where the subscript ‘s’ stands for stretched and \mathbf{k} is the wave vector of the traveling electric plane wave in the far-field. The stretching factors s_{x_i} , with $x_i \in \{x, y, z\}$, depend only on the coordinate of its stretching direction, that is, $s_{x_i} = s_{x_i}(x_i)$ and are, in general, complex quantities [38, 41]; on the domain Ω , outside the PML, the scale factors are equal to one. Additionally, the divergence and curl operators in the stretched coordinate system are [47]:

$$\nabla_s \cdot \mathbf{v} = \frac{1}{s_x s_y s_z} \nabla \cdot [\text{diag}(s_y s_z, s_x s_z, s_x s_y) \mathbf{v}], \quad (2.39b)$$

$$\nabla_s \times \mathbf{v} = \text{diag}\left(\frac{1}{s_y s_z}, \frac{1}{s_x s_z}, \frac{1}{s_x s_y}\right) \nabla \times [\text{diag}(s_x, s_y, s_z) \mathbf{v}], \quad (2.39c)$$

where $\mathbf{v} = v_x \hat{\mathbf{e}}_x + v_y \hat{\mathbf{e}}_y + v_z \hat{\mathbf{e}}_z$ is an arbitrary vector and $\text{diag}(a, b, c)$ is a matrix whose only non-zero elements are its arguments placed along its diagonal. From Eq. (2.39a), the dispersion relation of a plane wave is

$$\mathbf{k} \cdot \mathbf{k} = k^2 = \mu \epsilon \omega^2 = \left(\frac{k_x}{s_x} \right)^2 + \left(\frac{k_y}{s_y} \right)^2 + \left(\frac{k_z}{s_z} \right)^2, \quad (2.40)$$

whose solution is given by [38, 41]

$$k_x = k s_x \sin \theta \cos \varphi, \quad k_y = k s_y \sin \theta \sin \varphi, \quad \text{and} \quad k_z = k s_z \cos \theta, \quad (2.41)$$

with φ and θ the azimuthal and polar angles, respectively. If any of the stretching factors are chosen so that $\text{Im}[s_{x_i}] < 0$, then the EM fields in the PML decay exponentially in the x_i -direction.

In between the domains Ω and Ω_{PML} there is a boundary, which can be locally considered as a plane interface. The Fresnel’s reflection amplitude coefficients —for s- and p-polarization relative to the boundary between the domains— can be defined as usual since the ratio of the incident and the reflected electric field in the stretched coordinate system does not depend on any stretching coefficient s_{x_i} [38, 41]. From the continuity of the tangential component of the electric field, the reflection amplitude coefficients for both polarization states are [22]

$$r_s = \frac{k_z^{(\text{PML})} s_z^{(\text{PML})} \mu_{\text{PML}} - k_z^{(\Omega)} s_z^{(\Omega)} \mu_\Omega}{k_z^{(\text{PML})} s_z^{(\text{PML})} \mu_{\text{PML}} + k_z^{(\Omega)} s_z^{(\Omega)} \mu_\Omega} \quad \text{and} \quad r_p = \frac{k_z^{(\text{PML})} s_z^{(\text{PML})} \epsilon_{\text{PML}} - k_z^{(\Omega)} s_z^{(\Omega)} \epsilon_\Omega}{k_z^{(\text{PML})} s_z^{(\text{PML})} \epsilon_{\text{PML}} + k_z^{(\Omega)} s_z^{(\Omega)} \epsilon_\Omega}. \quad (2.42)$$

where the z component of the wave vector \mathbf{k} is perpendicular to the locally plane interface, and the superscripts denote whether the functions are evaluated at Ω or Ω_{PML} . In a similar manner, the phase matching condition of the reflected and incident wave at the interface between Ω and Ω_k states that [38]

$$k^{(\text{PML})} s_x^{(\text{PML})} \sin \theta_{\text{PML}} \cos \varphi_{\text{PML}} = k^{(\Omega)} s_x^{(\Omega)} \sin \theta_\Omega \cos \varphi_\Omega, \quad (2.43a)$$

$$k^{(\text{PML})} s_y^{(\text{PML})} \sin \theta_{\text{PML}} \sin \varphi_{\text{PML}} = k^{(\Omega)} s_y^{(\Omega)} \sin \theta_\Omega \sin \varphi_\Omega. \quad (2.43b)$$

From Eqs. (2.40)–(2.43) it can be seen that the reflection amplitude coefficient for both polarization states vanish if the magnetic permeability and the electric permittivity, as well as the stretch coefficient s_x and s_y , of the PML matches those of the domain Ω since such conditions leads to $\varphi_{\text{PML}} = \varphi_\Omega$ and $\theta_{\text{PML}} = \theta_\Omega$ [38]. Therefore, a prefect matching layer can be described as a thin film Ω_{PML} , surrounding Ω , with the following specifications

Perfectly Matching Layer Conditions

$$\left. \begin{aligned} \varepsilon_\Omega &= \varepsilon_{\text{PML}}, & \mu_\Omega &= \mu_{\text{PML}} \\ s_x^{(\Omega)} &= s_x^{(\text{PML})}, & s_y^{(\Omega)} &= s_y^{(\text{PML})} \end{aligned} \right\} \implies r_s = r_p = 0. \quad (2.44)$$

Let us note that no condition have been established to the stretching coefficient s_z and that Eq. (2.44) is valid for any frequency ω , any angle of incidence, and any value of the stretched coordinates in the parallel directions to the interface [38, 39]. The PML conditions allow non-zero transmission coefficients, thus incoming waves can arise due to the finite size of Ω_{PML} ; to avoid such non-physical incoming waves, s_z is chosen as a complex quantity with a negative imaginary part, so the waves vanish exponentially after entering the PML domain [38, 41].

In order to employ the PML conditions [Eq. (2.44)] in the domain Ω where the FEM is employed to solve the scattering problem [Eq. (2.23)], let us write the Maxwell's equations in the PML—with the complex stretched coordinate system [Eq. (2.39)]—in the stretched coordinate system employed in Ω . To do so, let us relate the EM fields in the PML, $\mathbf{E}^{(\text{PML})}$ and $\mathbf{H}^{(\text{PML})}$, with the EM fields in the domain Ω , $\mathbf{E}^{(\Omega)}$ and $\mathbf{H}^{(\Omega)}$, as [38]

$$\mathbf{E}^{(\Omega)} = \text{diag}(s_x, s_y, s_z) \mathbf{E}^{(\text{PML})} \iff \mathbf{E}^{(\text{PML})} = \text{diag}\left(\frac{1}{s_x}, \frac{1}{s_y}, \frac{1}{s_z}\right) \mathbf{E}^{(\Omega)}, \quad (2.45a)$$

$$\mathbf{H}^{(\Omega)} = \text{diag}(s_x, s_y, s_z) \mathbf{H}^{(\text{PML})} \iff \mathbf{H}^{(\text{PML})} = \text{diag}\left(\frac{1}{s_x}, \frac{1}{s_y}, \frac{1}{s_z}\right) \mathbf{H}^{(\Omega)}. \quad (2.45b)$$

The Maxwell's equations in the domain Ω_{PML} are written as in Eq. (2.17)—with no external sources—with the operators defined in Eq. (2.39) applied to $\mathbf{E}^{(\text{PML})}$ and $\mathbf{H}^{(\text{PML})}$ but they can be rewritten in the Ω domain by substituting Eqs. (2.45) into them and isolating the operators in the non-stretched coordinates applied to $\mathbf{E}^{(\Omega)}$ and $\mathbf{H}^{(\Omega)}$. This procedure yields [38]

$$\nabla_s \cdot (\varepsilon \mathbf{E}^{(\text{PML})}) = 0 \implies \nabla \cdot [\varepsilon \mathbb{A} \mathbf{E}^{(\Omega)}] = 0, \quad (2.46a)$$

$$\nabla_s \cdot (\mu \mathbf{H}^{(\text{PML})}) = 0 \implies \nabla \cdot [\mu \mathbb{A} \mathbf{H}^{(\Omega)}] = 0, \quad (2.46b)$$

$$\nabla_s \times \mathbf{E}^{(\text{PML})} = i\omega \mu \mathbf{H}^{(\text{PML})} \implies \nabla \times (\mathbf{E}^{(\Omega)}) = i\omega (\mu \mathbb{A}) \mathbf{H}^{(\Omega)}, \quad (2.46c)$$

$$\nabla_s \times (\mu \mathbf{H}^{(\text{PML})}) = -i\omega \varepsilon \mathbf{E}^{(\text{PML})} \implies \nabla \times (\mu \mathbb{A} \mathbf{H}^{(\Omega)}) = -i\omega (\varepsilon \mathbb{A}) \mathbf{E}^{(\Omega)}, \quad (2.46d)$$

where \mathbb{A} is given by

$$\mathbb{A} = \text{diag}\left(\frac{s_y s_z}{s_x}, \frac{s_x s_z}{s_y}, \frac{s_x s_y}{s_z}\right). \quad (2.47)$$

Within the approach in Eqs. (2.46), the PML can be implemented into the weak formulation of the scattering problem by introducing a homogeneous, but anisotropic, optical response to the material that embeds the scatterers, and thus simulate an infinite embedding media [38, 39, 41]. Comparing the Maxwell's equations representation in Eqs. (2.17) and (2.46), the anisotropy of the media is introduced into the weak formulation of the scattering problem [Eq. (2.23)] by replacing \mathbf{E} by $\mathbb{A}\mathbf{E}$ [38].

As stated in the PML conditions [Eq. (2.44)], the scalar values of ε and μ , and of s_x and s_y , must match in the medium surrounding the scatterers and in the PML domain. The anisotropy of the dielectric function sets $s_x = s_y = s_z = 1$ in Ω so the scattering problem is described exactly as in Eq. (2.23). In order to guarantee no incoming waves in the domain Ω due to the finite size of Ω_{PML} , let us choose s_z with a negative imaginary part in Ω_{PML} . Lastly, anisotropy is introduced into the finite element formulation of the scattering problem [Eqs. (2.24)] by including the matrix \mathbb{A} as discussed above. Therefore, the PML implementation into the FEM is summarized as follows:

Perfectly Matching Layer Implementation into Finite Element Method

$$\mathbb{A}\mathbf{e} = \mathbf{0} \quad \text{with} \quad \mathbb{A} \text{ and } \mathbf{e} \text{ as in Eqs. (2.24)}, \quad (2.48a)$$

$$\mathbb{A} = \text{diag}(s_z, s_z, s_z^{-1}), \quad \text{with} \quad s_z = 1 \text{ in } \Omega \text{ and } \text{Im}[s_z] < 0 \text{ in } \Omega_{\text{PML}}, \quad (2.48b)$$

$$(\mu^{-1}\nabla \times \boldsymbol{\eta}_i) \cdot (\nabla \times \boldsymbol{\eta}_j) \rightarrow (\mathbb{A}^{-1}\mu^{-1}\nabla \times \boldsymbol{\eta}_i) \cdot (\nabla \times \boldsymbol{\eta}_j), \quad (2.48c)$$

$$\boldsymbol{\eta}_i \cdot \boldsymbol{\eta}_j \rightarrow \boldsymbol{\eta}_i \cdot \mathbb{A}\boldsymbol{\eta}_j, \quad (2.48d)$$

which is valid for any angular frequency ω . As a last comment, Eq. (2.48) solves the scattering problem within the domain Ω but the obtained values of the scattered EM fields in Ω_{PML} have no physical meaning and are of no concern [38].

2.3 Finite Element Method and Analytical Solutions

The light scattering problem in its weak formulation, and assuming harmonic time dependency [Eqs. (2.23)], can be solved by means of the so-called FEM in the frequency domain, given by Eqs. (2.24). There are several software that allow the user to introduce the desired geometry, physical properties of the system, and boundary conditions in order to calculate the scattered electric field through the FEM. Examples of commercial FEM software with the capability to solve Eqs. (2.23) are Altair HyperWorks and CTS StudioSuite as well as open-source alternatives, such as Elmer, OpenFOAM and SCUFF-EM. Nevertheless in this work, the commercial software COMSOL Multiphysics™ Ver. 5.4 (COMSOL) was employed; for a more technical description of the performed COMSOL simulation see Appendix C.

The FEM implemented within COMSOL is based on the Galerkin Method [Eq. (2.10)] with a variety of finite element families, including, but not limited to, the Lagrange [Ec. (2.14)], the Hermite [Ec. (2.15)] and the lowest order Nédélec⁶ families [Ec. (2.26)] [48]; such finite

⁶Nédélec Elements of higher order are implemented in COMSOL for particular shapes only [48].

2. THE FINITE ELEMENT METHOD

element families are built within COMSOL for different shapes in 2D and 3D geometries: triangles, rectangles, pyramids, prisms, tetrahedrons, and more [48]. The core of COMSOL allows the user to set the desired geometry of the PDE problem to be solved, as well as the discretization method and the matrix inversion algorithms to solve Eq. (2.10) [48]. Additionally, the COMSOL's package Wave Optics implements the Maxwell's eigenvalue problem —considering harmonic time dependency as in Eqs. (2.23) [48]— alongside the physical characteristics of the system: the optical properties, encoded into the electric permittivity and magnetic permeability, of different materials and the several boundary conditions such like the generalized Sommerfeld's radiation condition [Eq. (2.38)] or the PML [Eq. (2.44)] [49]. The Wave Optics module returns the total electric field and the user can separate it into two contributions: the incident \mathbf{E}^i and the induced \mathbf{E}^{ind} electric fields; the later corresponds to the scattered (internal) electric field \mathbf{E}^{sca} (\mathbf{E}^{int}) outside (inside) any scatterer [49].

To minimize errors that may arise in simulations performed with COMSOL, the analytical solution given by the Mie Theory for the light scattering due to a spherical particle —introduced in Section 1.2— was contrasted against an approximated solution returned by COMSOL. Since COMSOL's Documentation [48] recommends to let the software to choose the kind of finite element⁷ to be used, the only numerical characteristics analyzed were the size of the domain Ω , its discretization into finite elements (mesh size)⁸, the discretization of the spherical scatterer, and the thickness of the PML used to simulate an open boundary. The geometry employed for the FEM approximated solution, built with COMSOL's internal tools, is shown in Fig. 2.4 where a single spherical NP (blue) is embedded in the middle of the box-shaped⁹ matrix (gray) and this last is covered by a PML (blue) which allows the system to be studied as an infinite non-absorbing medium; the generalized Sommerfeld's radiation condition [Eq. (2.38)] was set

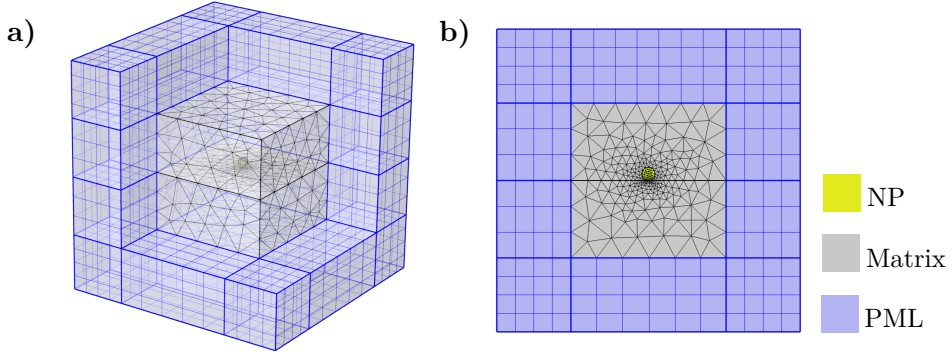


Fig. 2.4: a) Three dimensional view and b) cross section of the geometry employed to solve the light scattering due to a spherical NP (blue) embedded in a non-absorbing matrix (gray) illuminated by a plane wave in COMSOL; the system is totally covered by a PML (blue) with rectangular geometry. The upper layer of the PML in a) is hidden to allow a better view of the setup.

⁷The build geometries within COMSOL may require a transformation from the reference finite elements to the real finite elements but COMSOL's internal tools guarantee a non-vanishing Jacobian for such transformations since they are not highly deformed. See *Mesh Element Quality and size* in [48].

⁸COMSOL allows the user to set a minimum and a maximum size of the employed finite elements and these parameters can be chosen as global or local to specific regions [48].

⁹The box-shaped geometry was chosen so that in future work, the reflectance and transmittance of the system can be calculated by the internal functions of COMSOL, which requires a planar interface to act as a sensor.

in addition to the PML since it enhances the performance of the COMSOL simulation. It is worth noting that COMSOL's internal tools proposes a meshing size by default [48] and that a thickness for the PML of a fourth of the wavelength λ of \mathbf{E}^i is recommended [49].

To contrast the solutions obtained analytically and through the FEM, the observable optical quantities in the far-field regime, that is, the scattering Q_{sca} , absorption Q_{abs} , and extinction Q_{ext} efficiencies were calculated with both approaches and contrasted. Since the FEM returns the value of the electric field in the whole domain Ω , the Eqs. (1.8), (1.9) and (1.12) were employed to calculate Q_{sca} , Q_{abs} and Q_{ext} , respectively, while they can be calculated with the Mie Theory through Eqs. (1.41) and (1.42) and the Optical Theorem [Eq. (1.12)]. In Fig. 2.5a) the efficiencies Q_{sca} (black), Q_{abs} (orange) and Q_{ext} (blue) are shown as a function of the incident wavelength λ , in the visible light regime, of the incoming electric plane wave \mathbf{E}^i that illuminates a AuNP of radius $a = 12.5$ nm (employing the size-corrected dielectric function —see Appendix B— for its optical response) embedded in air (with refractive index $n_m = 1$); the continuous lines correspond to Q^{Mie} , the analytical solution calculated by the Mie Theory, and the markers to Q^{FEM} the approximated solution returned by COMSOL with the default values for the meshing size —global parameters applied to the whole domain Ω and the PML—, the recommended size for the matrix —the minimum distance between the AuNP and the PML— and the recommended PML thickness; the values of these parameters are shown in Fig. 2.5a) as inset text. The absolute error (Abs. Error) between the analytical and the FEM approximated solution, given by $|Q^{\text{Mie}} - Q^{\text{FEM}}|$, is shown in Fig. 2.5b).

The results in Fig. 2.5a) show that the scattering efficiency of a 12.5 nm AuNP, which was multiplied by a factor of 100, is two orders of magnitude smaller than the absorption efficiency, thus making absorption the most important contribution to the light extinction, as discussed in Section 1.2.3. This behavior is reproduced by the FEM simulation as the absolute error of

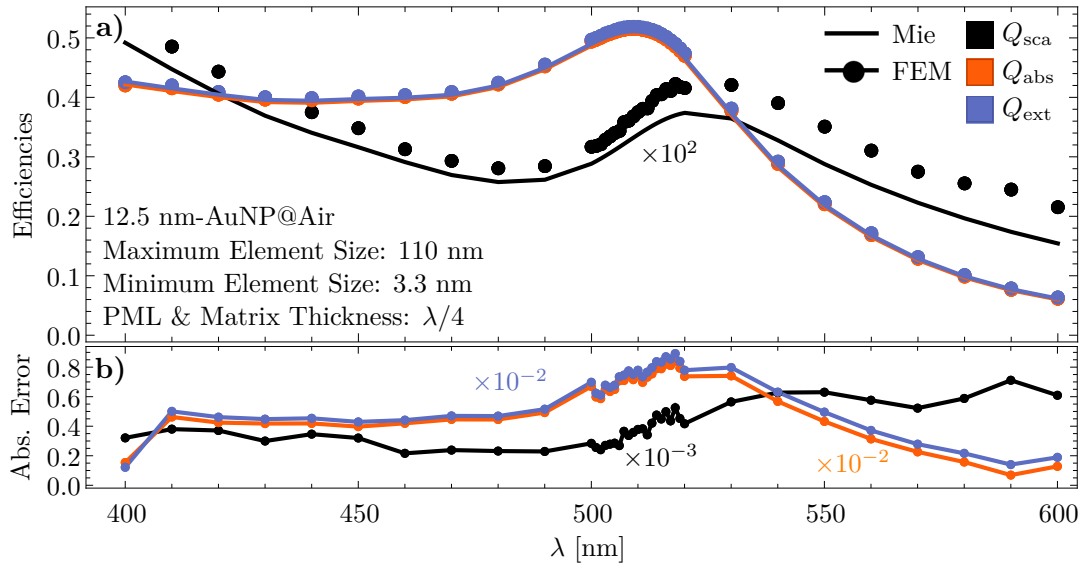


Fig. 2.5: a) Scattering Q_{sca} (black), absorption Q_{abs} (orange), and extinction Q_{ext} (blue) efficiencies of a 12.5 nm AuNP embedded in air calculated by means of the Mie Theory (continuous) and the FEM (markers), and b) their absolute error, as a function of the wavelength λ of the incident plane wave.

2. THE FINITE ELEMENT METHOD

the efficiencies [Fig. 2.5b)] shows a discrepancy between the analytical and the approximated solution in the second digit after the decimal point for Q_{abs} and Q_{ext} , and in the third digit after the decimal point for Q_{sca} . It is worth noting that the absolute error for the absorption efficiency is maximum at a wavelength $\lambda \sim 509$ nm, which corresponds to the LSPR wavelength, while the absolute error for the scattering efficiency grows linearly with the incident wavelength for $\lambda < 521$ nm, the wavelength of maximum scattering. On the one hand, the absorption efficiency is calculated numerically by integrating \mathbf{E}^{int} in the volume of the AuNP [Eq. (1.9)], thus the associated error arises due to the meshing inside the AuNP, which does not resolve \mathbf{E}^{int} good enough for the value of λ that maximizes it. On the other hand, the scattering efficiency is obtained by integrating \mathbf{E}^{sca} on a closed surface outside the AuNP [Eq. (1.8)] —for the FEM simulations the boundary of the AuNP was chosen as the integration surface—, therefore the associated error is related either to the meshing or to unappropriated implementation of the boundary conditions to simulate an infinite matrix.

To analyze the effect of the size of the matrix on the numerical convergence of the FEM approximated solution, its absolute error against the analytical Mie Theory solution is shown in Fig. 2.6 for Q_{sca} , Q_{abs} and Q_{ext} , for two different systems: a 12.5 nm AuNP embedded in air [Fig. 2.6a)] and in glass [Fig. 2.6b)]. The efficiencies are evaluated at the LSPR wavelength (continuous lines) —507 nm for air and 533 nm for glass— and at the wavelength of maximum scattering (dash lines) —521 nm for air and 543 nm for glass— where the error was maximum and where it started to grow, as seen in Fig. 2.5b). In Fig. 2.6 the efficiencies are plotted as a function of the minimum distance between the AuNP’s surface and the PML, that is, as a function of the size of the matrix (in the upper frame the distance is measured in units of the AuNP’s radius $a = 12.5$ nm) and the chosen values for the element size and the PML thickness for the FEM simulation were the same as thos in Fig. 2.5.

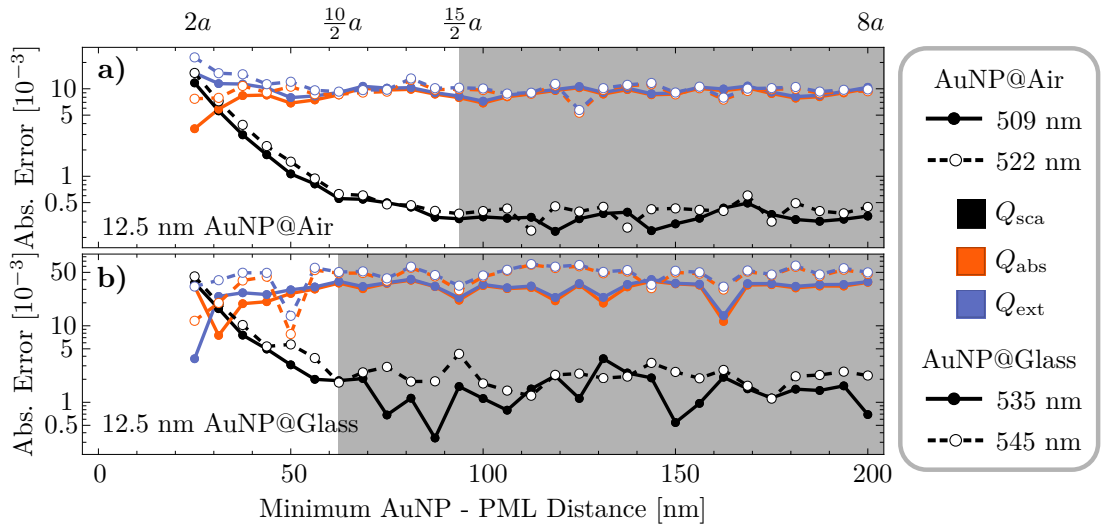


Fig. 2.6: Absolute error between the Mie Theory and the FEM approximated solution of the scattering (black), absorption (orange) and extinction (blue) efficiencies of a 12.5 nm AuNP embedded **a)** in an air matrix ($n_m = 1$) and **b)** in a glass matrix ($n_m = 1.5$) as a function of the matrix size. The FEM numerical simulation parameters were the default mesh size —maximum (minimum) element size of 110 nm (3.3 nm) globally— and the recommended $\lambda/4$ PML thickness.

The absolute error on the absorption and extinction efficiencies remain in the same order of magnitude independently of the matrix size for any matrix material and chosen wavelength, as it can be seen from the orange and blue lines in Fig. 2.6. However, the scattering efficiency does decrease its absolute error, linearly, as the matrix size grows up to a critical value, $\sim 15a/2$ and $\sim 10a/2$ for an air and a glass matrix, respectively, after which the relative error converges. The gray shaded region in Figs. 2.6a) and 2.6b) corresponds to the converged regime for each matrix material. Since the ratio between the critical value of the matrix size between the air and the glass matrix system is approximately 1.5, the refractive index of glass, a matrix of width $\sim (15 + 1)an_m$ guarantees a minimum in the scattered electric field \mathbf{E}^{sca} due to the size of the matrix. This result is only valid for plasmonic NPs, such as the AuNPs, small compared to the incident wavelength, since the scattering is the least important contribution to extinction, as seen in Fig. 2.5a). The convergence of the absolute error on the scattering efficiencies is due to the Sommerfeld's radiation condition [Eq. (2.38)], which is an enough strong criteria to simulate an open boundary if the matrix is sufficiently large; this is supported by the absolute errors shown in Fig. 2.7 where they are plotted as a function of the PML thickness considering a default meshing size —see values in Fig. 2.5a)— and a matrix width of $(15 + 1)an_m$ for both an air [Fig. 2.7a)] and a glass [Fig. 2.7b)] matrix system, where none of the shown absolute errors change considerably.

From the analysis of Figs. 2.6 and 2.7, the absolute error on the scattering efficiency obtained with the default COMSOL parameters [Fig. 2.5] was decreased for a plasmonic NP small compared to the incident wavelength, such as a 12.5 AuNP illuminated in the visible range. To diminish the absolute error on the absorption efficiency, and thus on the extinction, a variation of the mesh size inside the AuNP was performed, while setting the default mesh size in the matrix but considering a recommended PML thickness of $\lambda/4$ and a matrix width of $(15 + 1)an_m$. In Fig. 2.8 the absolute error of the scattering, absorption and extinction efficiencies

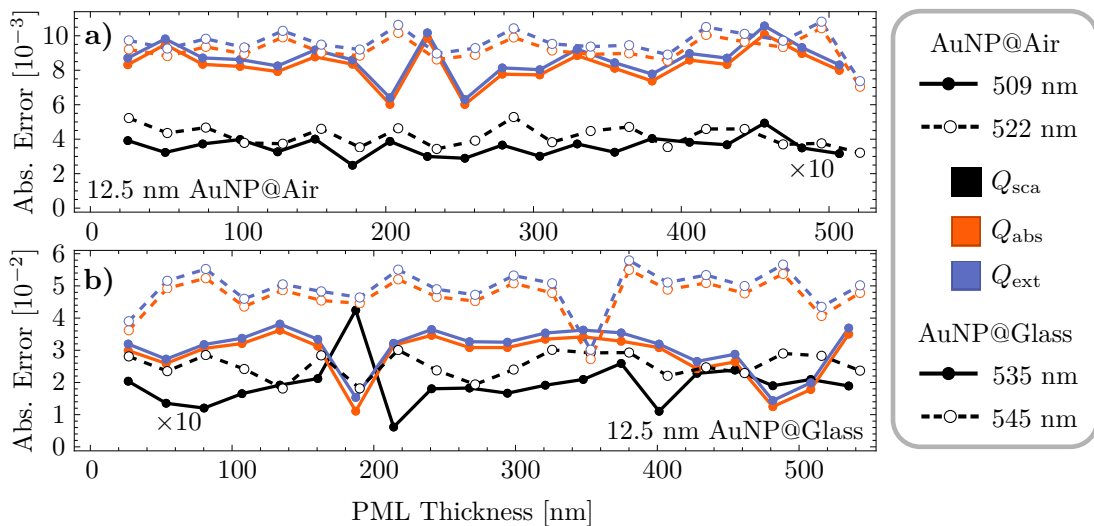


Fig. 2.7: Absolute error between the Mie Theory and the FEM approximated solution of the scattering (black), absorption (orange) and extinction (blue) efficiencies of a 12.5 AuNP embedded **a)** in an air matrix ($n_m = 1$) and **b)** in a glass matrix ($n_m = 1.5$) as a function of the PML thickness. The FEM numerical simulation parameters were the default mesh size —maximum (minimum) element size of 110 nm (3.3 nm) globally— and a matrix width of $(15 + 1)an_m$.

are shown as a function of the maximum mesh size inside a 12.5 AuNP embedded in air [Fig. 2.8a)] and in glass [Fig. 2.8b)], at the wavelength of the LSPR and at the maximum scattering wavelength for each system. The variation of the minimum mesh size is shown in nanometers for the lower frame side and in fractions of the AuNP's radius for the upper frame side.

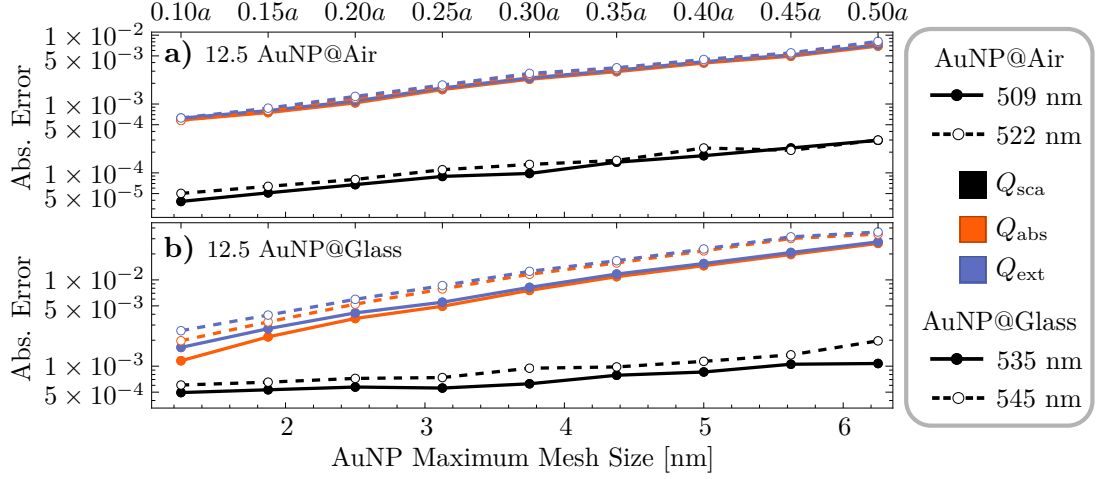


Fig. 2.8: Absolute error between the Mie Theory and the FEM approximated solution of the scattering (black), absorption (orange) and extinction (blue) efficiencies of a 12.5 AuNP embedded **a)** in an air matrix ($n_m = 1$) and **b)** in a glass matrix ($n_m = 1.5$) as a function of the mesh size inside the AuNP. The FEM numerical simulation parameters were the default mesh size in the matrix—maximum (minimum) element size of 110 nm (3.3 nm)—, a matrix width of $(15 + 1)a n_m$ and a PML thickness of $\lambda/4$.

As it can be seen in Fig. 2.8, the absolute error of the efficiencies decreases exponentially as the mesh size inside the AuNP becomes finer for all the considered cases: air and glass matrices at two different wavelengths each. Such behavior can be explained since the absorption (scattering) efficiency is obtained by integrating the internal (scattered) electric field at the AuNP's volume (surface). Thus, a finer mesh at the scatterer allows the induced electric field to be not only better resolved by the FEM, but also to increase the accuracy of the performed numerical integration. Additionally, the results in Fig. 2.8 show that the decrement of the absolute error on Q_{abs} has a higher rate than the decrement on the absolute error of Q_{sca} due to the amount of points in the mesh inside the volume and on the surface of the AuNP. Lastly, the refinement of the mesh size inside the AuNP, alongside with the chosen matrix width and PML thickness, guarantees a difference between the analytical Mie Theory solution and the approximated FEM solution up to the fourth digit after the decimal point both on the scattering and absorption efficiencies. If a refinement in the mesh side inside the matrix were to be done, the absolute error on the efficiencies may diminish even further, but such refinement may not be appreciable for the goals of this thesis. Therefore, the recommended mesh side in the matrix—maximum element size of $\lambda/(6n_m)$ for first order finite elements [48]—is used as it is smaller than the default mesh size in this region.

Taking into account the results shown of Figs. 2.6–2.8 and the recommended maximum mesh size in the matrix, a converged result of the scattering, absorption and extinction efficiencies by means of the FEM is obtained. In Fig. 2.9 the optical efficiencies of a 12.5 nm AuNP embedded in an air and a glass matrix are shown as a function of the incident wavelength λ , as well as the

relative error between the analytical (lines) and FEM (markers) results: the continuous lines and solid markers correspond to the air matrix case while the dashed lines and open markers to the glass matrix case.

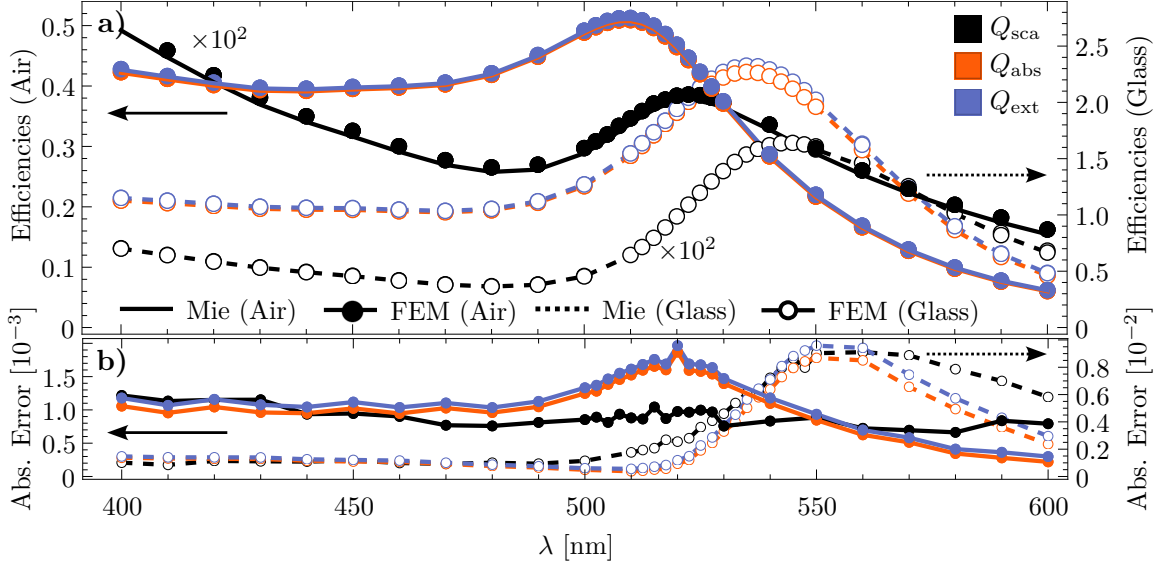


Fig. 2.9: a) Scattering Q_{sca} (black), absorption Q_{abs} (orange) and extinction Q_{ext} (blue) efficiencies of a 12.5 nm AuNP embedded in air calculated by means of the Mie Theory (continuous lines) and the FEM (solid markers) and embedded in glass (dashed lines and open markers), and b) their absolute error, as a function of the wavelength λ of the incident plane wave. The FEM numerical simulation parameters were the recommended mesh side in the matrix —maximum element size of $\lambda/(6n_m)$ — and a maximum mesh side inside the AuNP of $a/5$, a matrix width of $(15 + 1)a n_m$ and a PML thickness of $\lambda/4$.

By comparing the absolute error employing COMSOL's default values for the FEM simulation [Fig. 2.5b)] with optimized the parameters [Fig. 2.9b)] considering an air matrix, it can be seen that the later is an order of magnitud smaller for the absorption and extinction efficiencies in the visible spectrum, while the absolute error of the scattering efficiency between these choices of parameters remains the same nevertheless, the FEM simulation with the optimized parameters required less computational resources than with the default COMSOL parameters due to the smaller matrix size. Additionally, the absolute error of the optical efficiencies considering a AuNP embedded in a glass matrix are smaller for all efficiencies in the visible spectrum than those of a AuNP embedded in an air matrix. This behavior is explained by the nominal values of the optical efficiencies [Fig. 2.9a)] since the greater they are, the greater the induced electric field, that is, the induced electric fields are better resolved for more optically dense media and thus their absolute error diminishes.

Chapter 3

Results and Discussion

The problem of the absorption and scattering of light by a single nanoparticle (NP), illuminated by a monochromatic plane wave, is analytically described by the Mie Theory (Section 1.2) if the NP is considered to be embedded in an infinite medium (the matrix). When more realistic conditions are considered, such as the presence of a second medium (the substrate) forming a planar interface with the matrix and the possibility of a partial embedding of the NP inside the substrate, the Mie Theory is no longer adequate to study the optical properties of such systems. In this Chapter, the optical response of a gold (Au) spherical NP of radius $a = 12.5$ nm, below, above, and at a planar interface between air and glass is calculated through the Finite Element Method (FEM), when a monochromatic plane wave of wavelength λ traveling in the direction \mathbf{k}^i illuminates the system at an angle of incidence θ_i , considering a defined polarization state of the incident electric field \mathbf{E}^i . To identify the effect of the substrate and the embedding of the NPs inside the substrate, the absorption and scattering efficiencies [Eqs. (1.8), (1.9) and (1.43)], as well as the radiation pattern (see Fig. 1.5) and the distribution of the induced electric field on and inside the NP (see Fig. fig:NearField) are calculated numerically for the desired geometries and compared with limiting cases of the Mie theory: a AuNP isolated in a matrix of air and in a matrix of glass.

The aforementioned analysis is organized as follows: In Section 3.1 it is addressed the extreme cases of the supported and the totally embedded NP illuminated at normal incidence (Section 3.1.1) and at oblique incidence (Section 3.1.2), while in Section 3.2 the effect of the partially embedding is studied considering once again normal (Section 3.2.1) and oblique (Section 3.2.2) incidence.

3.1 Supported and Totally Embedded Spherical Particles

To compare the optical response of a NP in the presence of a substrate with that of a NP in a totally homogeneous environment, let us first analyze the spectral response given by the Mie Theory when the matrix and the size of the NP varies. In Fig. 3.1 it is shown the wavelength of resonance λ_{res} , that is, the wavelength at which the scattering (orange) and extinction (black) efficiencies are maximized, as a function of the radius a of a AuNP embedded in a matrix of air [Fig. 3.1a)] and of glass [Fig. 3.1b)], with a refractive index of $n_m = 1$ and $n_m = 1.5$, respectively,

3. RESULTS AND DISCUSSION

and as a function of the refractive index of the matrix n_m for a AuNP with a radius of $a = 12.5$ nm [Fig. 3.1c)] and with a radius of $a = 50$ nm [Fig. 3.1d)]. For the optical response of the AuNP it was employed the experimental data as reported by Johnson and Christy [31] (filled circles) and by considering a size correction —see Appendix B— to it (empty circles).

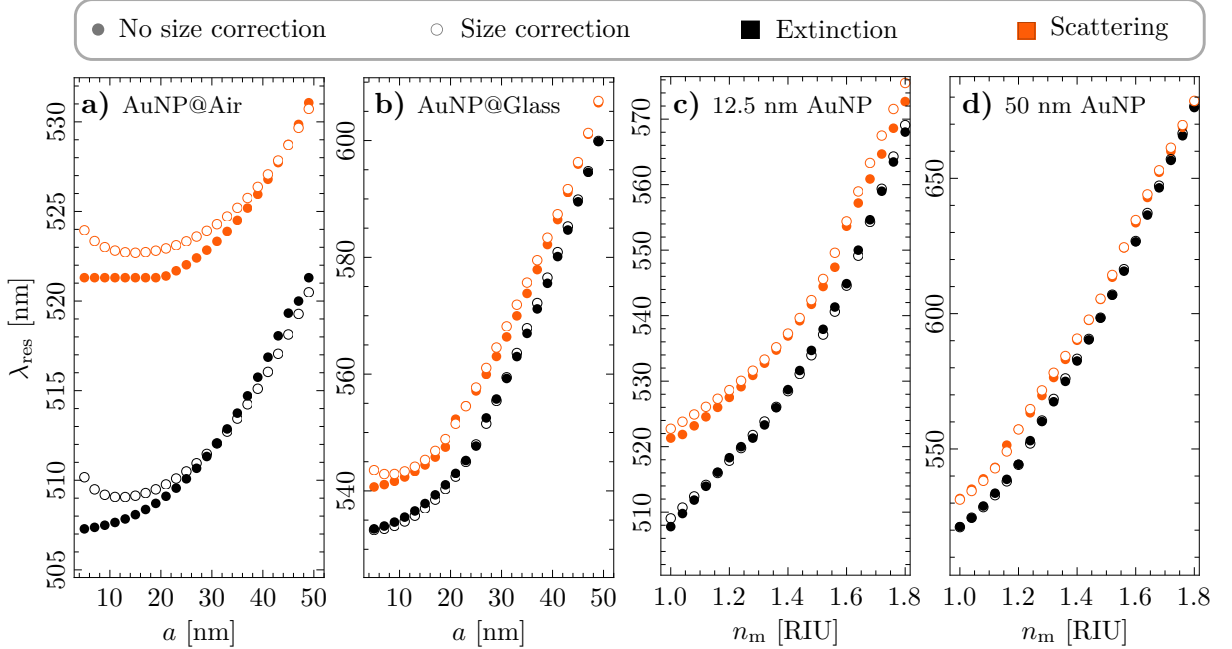


Fig. 3.1: Resonance wavelength λ_{res} of the scattering (orange) and extinction (black) efficiencies of a AuNP as a function of the NP's radius when embedded **a)** in air ($n_m = 1$) and **b)** in glass ($n_m = 1.5$), and as a function of the refractive index of the matrix n_m for a AuNP of radius **c)** 12.5 nm and **d)** 50 nm, using the dielectric function for gold as reported by Johnson and Christy [31] (filled circles) and considering a size correction to it (empty circles).

From the results shown in Fig. 3.1 it can be seen that the wavelength of resonance λ_{res} for the extinction, considering the bulk dielectric function for Au (filled circles), is smaller than that of the scattering and that the distance between them decreases as either the size of the AuNP or the refractive index of the matrix increases. This behavior arises from a redshift of λ_{res} for increasing values of a and n_m and it shows that, for particles small compared to the wavelength of the incident light in the matrix, the main contribution to the extinction of light is due to absorption processes and as the size of the AuNP grows, the extinction is dominated by its other contribution: the scattering, as discussed in Section 1.2.3 and supported by Eq. (1.12). The redshift of λ_{res} can also be observed when considering a size corrected dielectric function (empty circles). Remarkably, for values of radius $\lesssim 15/n_m$ there is a blueshift of λ_{res} , as it can be seen in Figs. 3.1a) and 3.1b), which is a consequence of a greater imaginary part of the dielectric function for the AuNP due to the size correction. On the other hand, an increase in n_m for a fixed radius presents only redshifts either with or without a size corrected dielectric function [see Figs. 3.1c) and 3.1d)].

The spectral behavior of the scattering and extinction of light due to a spherical NP summarized in Fig. 3.1 was calculated by assuming a homogeneous medium (the matrix) where the NP is embedded and thus allowing the direction of the illuminating plane wave to be arbitrary, yet yielding the same results. In the following Sections, the homogeneity of the surroundings of

3.1 Supported and Totally Embedded Spherical Particles

the NP is substituted by two semiinfinite media and thus modifying the optical response of the system depending on how it is illuminated.

3.1.1 Normal Incidence

The problem of scattering and absorption of light by single spherical NP embedded in a matrix, with refractive index n_m , illuminated by a plane wave with wavelength λ and traveling in the \mathbf{k}^i direction, has spherical symmetry, which was exploited to develop the Mie Theory as explained in Section 1.2. If a substrate, with refractive index n_s , is considered and the NP is located right above or below the interface —without crossing the substrate-matrix interface—, there are four combinations in which the system can be excited since the NP can be either embedded in the substrate or supported on it, and it can be illuminated either in an external —from the matrix to the substrate— or in an internal —from the substrate to matrix— configuration, as shown in Fig. 3.2a), where the following cases are depicted: Embedded-External (EE), Embedded-Internal (EI), Supported-External (SE) and Supported-Internal (SI). In the presence of the substrate, the electric field illuminating the AuNP is not the incoming plane wave but the sum of it with the reflected electric field (EI and SE) or the transmitted electric field (EE and SI), both of which can be calculated analytically through Fresnel's reflection and transmission amplitude coefficients, as discussed in Appendix C.

In Figs. 3.2b) and 3.2c) the absorption Q_{abs} and scattering Q_{sca} efficiencies are shown, respectively, as a function of λ for a AuNP of radius $a = 12.5$ nm in the Embedded-External (black), Embedded-Internal (orange), Supported-External (blue) and Supported-Internal (light orange) configurations; the green shaded regions correspond to the values between the two limiting

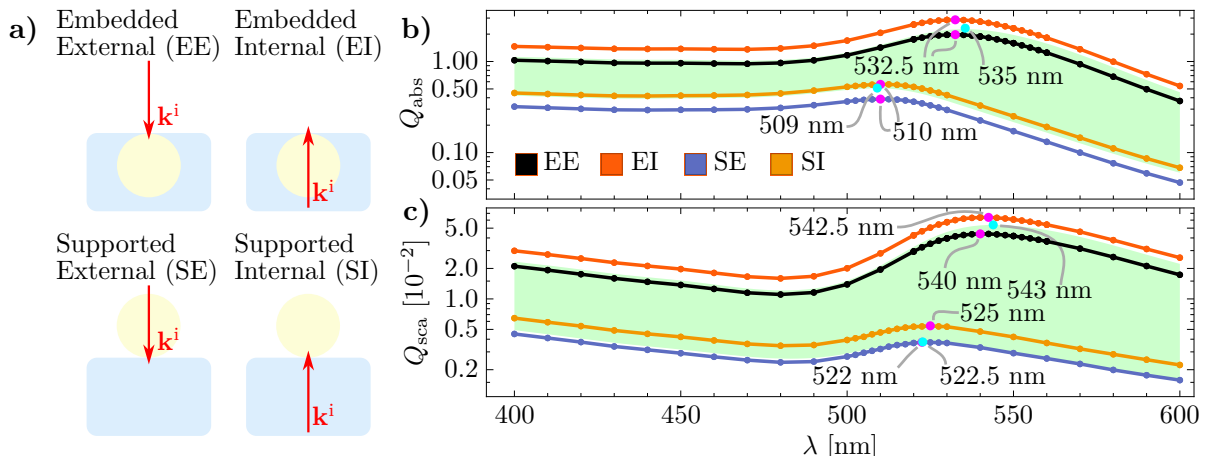


Fig. 3.2: a) Schematics of a AuNP embedded (E) in [supported (S) on] a glass substrate ($n_s = 1.5$) forming a planar interface with an air matrix ($n_m = 1$) and illuminated by a plane wave traveling normally to the air-glass interface in an external (E) and in an internal (I) configuration. b) Absorption Q_{abs} and c) scattering Q_{sca} efficiencies of a 12.5 nm AuNP as a function of the wavelength λ of the illuminating plane wave in different spatial configurations: EE (black), EI (orange), SE (blue) and SI (light orange). The green shaded region shows the two Mie-limiting cases of a AuNP embedded in air and in glass; the magenta (AuNP and substrate) and cyan (Mie-limiting) markers correspond to the efficiencies evaluated at the wavelength of resonance for each case.

3. RESULTS AND DISCUSSION

cases given by the Mie theory: the AuNP embedded in air (lower boundary) and embedded in glass (upper boundary). The magenta markers correspond to the values of the efficiencies evaluated at the wavelength of resonance considering the presence of a substrate while the cyan markers correspond to the efficiencies at the resonance wavelength for the Mie-limiting cases.

From the results shown in Figs. 3.2b) and 3.2c), it can be seen that both the absorption and scattering efficiencies of the four spatial configurations are of the same order of magnitude as the Mie-limiting cases and, even more, the values of the efficiencies for the embedded AuNP (black and orange lines) lie very close to the Mie-limiting case of the AuNP in glass (upper boundary of the green shaded region) and the same behavior is observed for the supported AuNP (blue and light orange lines) and the Mie-limiting case of a AuNP embedded in air (lower boundary of the green shaded region). The presence of a substrate yields an overall enhancement and damping of the scattering and the absorption efficiencies relative to the isolated NP, which depend on the illumination of the system since Q_{abs} and Q_{sca} are inversely proportional to the refractive index of the medium of incidence [Ecs. (1.8) and (1.9)]: If the system is illuminated in an external configuration, the obtained efficiencies are slightly decreased relative to the Mie-limiting case as it can be seen from the black and blue curves, which correspond to the EE and SE cases; on the other hand, the calculated efficiencies for the internal illuminated cases, that is for EI (orange) and SI (light orange), are enhanced relative to the Mie-limiting cases.

Another effect of the substrate in the optical response of the system is a slightly spectral shift of the excitation wavelength of the scattering and absorption efficiencies, which depends on the medium where the AuNP is located. For example, in Figs. 3.2b) and 3.2c) the wavelength of resonance for both the absorption and the scattering efficiencies (magenta markers) are redshifted ~ 1 nm, relative to the Mie-limiting case (cyan markers), for the AuNP supported on the substrate (blue and light orange curves) and blueshifted ~ 2 nm for the embedded AuNP (black and orange curves). These spectral shifts can be understood by considering the AuNPs as electric point dipoles parallel to the interface —an assumption consistent with the near-field distribution in the Mie-limiting cases and with the radiation patterns (see Figs. 1.5 and 1.3)— and their interaction with the image electric point dipoles induced within the substrate [11]. Both the dipoles induced in the AuNP and the image dipoles are parallel to the interface but its strength differs by a factor of $A_{\text{dip}} = (\sqrt{n_j} - \sqrt{n_i}) / (\sqrt{n_j} + \sqrt{n_i})$ [14], where n_j is the refractive index of the medium where the real dipole (the AuNP) is located and n_i of the medium where the image dipole is induced. If the AuNP is embedded in the substrate, then $A_{\text{dip}} > 0$ meaning that the induced dipole is parallel to the real dipole, which is a more energetic configuration that yields the spectral blueshift of the resonance. Conversely, if the AuNP is supported on the substrate then $A_{\text{dip}} < 0$ and the induced dipole is antiparallel to the real dipole, leading to a less energetic configuration and to the redshift observed in Figs. 3.2b) and 3.2c).

The absorption and scattering efficiencies are integral quantities which describe the global behavior of the induced electric field \mathbf{E}^{ind} , which corresponds to the internal electric field \mathbf{E}^{int} inside the AuNP and to the scattered electric field \mathbf{E}^{sca} outside of it. The distribution of \mathbf{E}^{ind} , for a fixed wavelength, is studied in two spatial regimes: the far- and the near-field. To analyze the optical response in the first regime, the radiation patterns of the AuNP are obtained numerically by plotting the magnitude of the scattered electric field in the far-field regime¹ $\mathbf{E}_{\text{far}}^{\text{sca}}$ as a function

¹The FEM returns the induced electric field by a scatterer in a neighborhood around it and there is no guarantee that the returned electric field, even at the boundaries of the volume where the FEM simulation is

3.1 Supported and Totally Embedded Spherical Particles

of the angle relative to the normal direction to the interface. In Figs. 3.3 and 3.4, it is shown the radiation patterns of the embedded and the supported AuNP, respectively, for several values of the wavelength λ of the incident plane wave, as well as considering an illumination of the system in an [a) and b)] external and in an [c) and d)] internal configuration; additionally, it is considered that the incident electric field is totally [a) and c)] parallel to the scattering plane \mathbf{E}_\parallel^i and [b) and d)] perpendicular to the scattering plane \mathbf{E}_\perp^i .

The radiation patterns of both the embedded and the supported AuNP follow the same

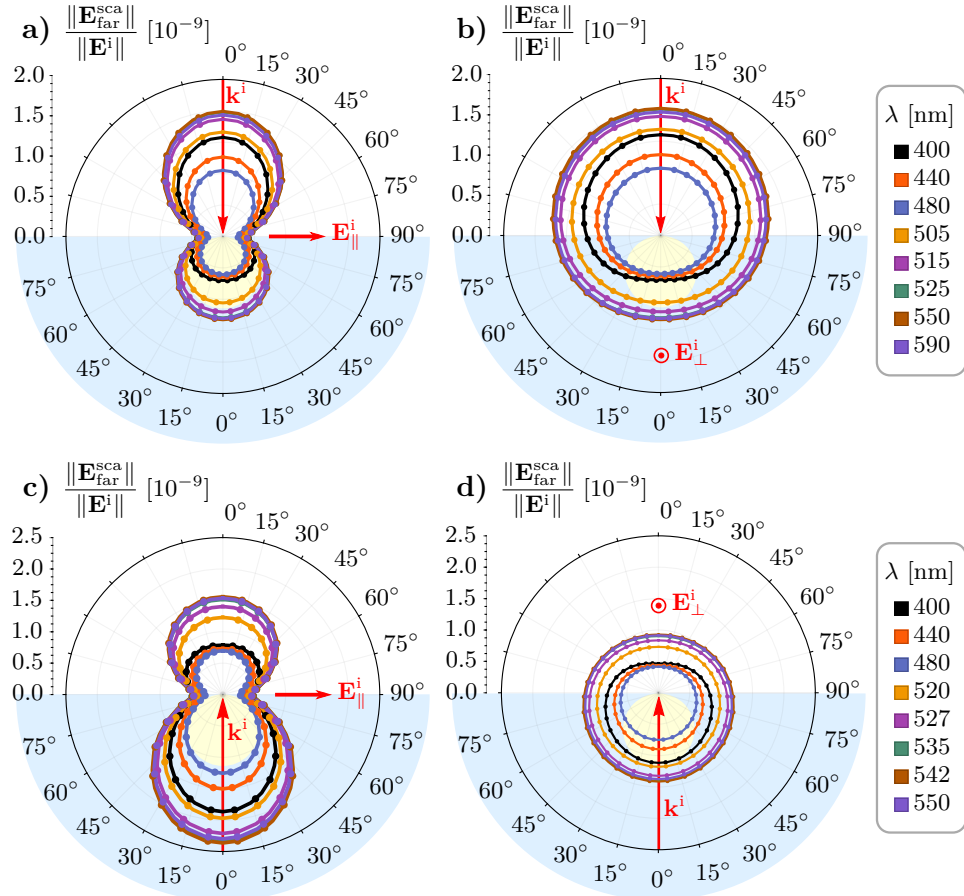


Fig. 3.3: Radiation patterns of a AuNP (light yellow) of radius $a = 12.5$ nm, embedded in a substrate (light blue) and illuminated by an electric plane wave \mathbf{E}^i with a wavelength λ , traveling in the \mathbf{k}^i direction normal to the interface between the substrate ($n_s = 1.5$) and the matrix ($n_m = 1$). The radiation patterns consider the illumination of the system a,b) in an external and c,d) in an internal configuration, and with an incident electric field a,c) \mathbf{E}_\parallel^i parallel to the scattering plane and b,d) \mathbf{E}_\perp^i perpendicular to it.

performed, corresponds to the far-field regime. To calculate the radiation pattern from the obtained induced electric field, COMSOL Multiphysics™ Ver. 5.4 employs the Stratton-Chu formula [49], which is a near-field to far-field transformation that propagates the known electric near-field over a mathematical surface surrounding all the scatterers to an arbitrary point [50]. The Stratton-Chu formula is obtained by employing the vectorial generalization of the Green's second identity with the electric and magnetic near-fields and the Green's function to the scalar Helmholtz equation multiplied by a normal vector to the integration surface [43].

3. RESULTS AND DISCUSSION

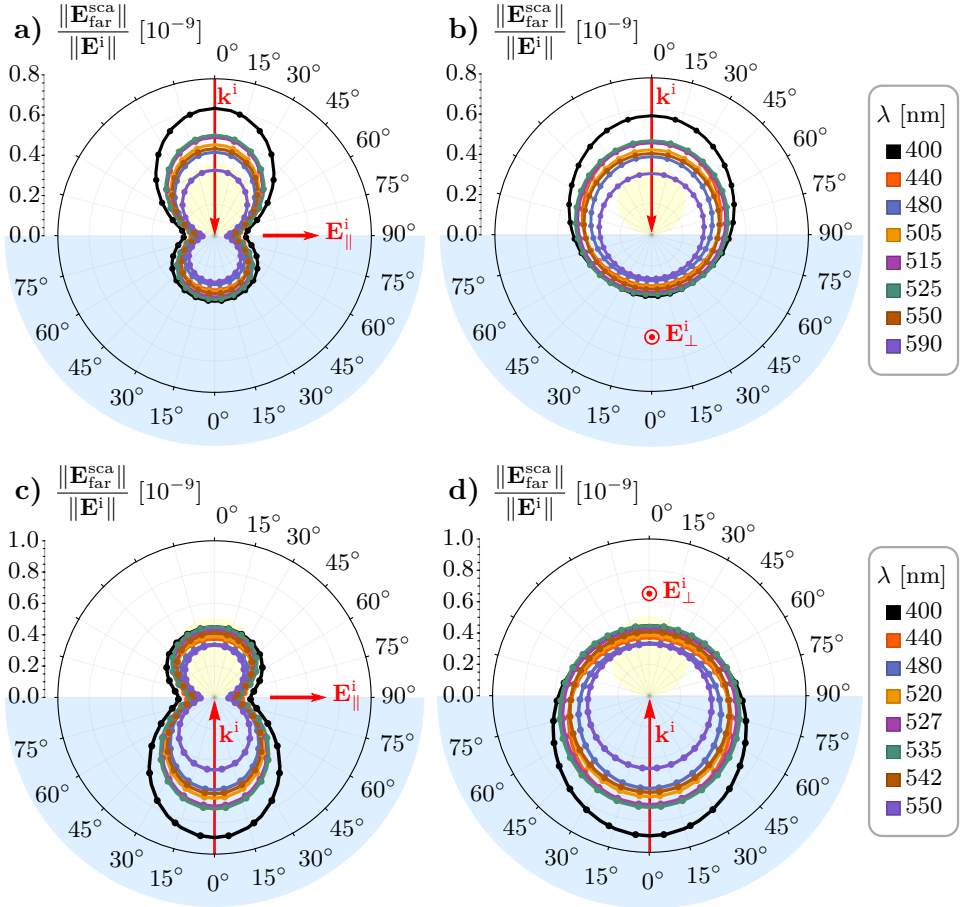


Fig. 3.4: Radiation patterns of a AuNP (light yellow) of radius $a = 12.5$ nm, supported on a substrate (light blue) and illuminated by an electric plane wave \mathbf{E}^i with a wavelength λ , traveling in the \mathbf{k}^i direction normal to the interface between the substrate ($n_s = 1.5$) and the matrix ($n_m = 1$). The radiation patterns consider the illumination of the system **a,b**) in an external and **c,d**) in an internal configuration, and with an incident electric field **a,c**) \mathbf{E}_\parallel^i parallel to the scattering plane and **b,d**) \mathbf{E}_\perp^i perpendicular to it.

trend independently of the illuminating wavelength λ but the amplitude is modulated by the scattering efficiencies shown in Fig. 3.2c). For example, in the EE and EI cases (Fig. 3.3) the scattered electric field (in the far-field) decreases its amplitude as the wavelength increases from 400 nm to 480 nm (black, orange and blue curves) and from 550 nm to 600 nm, while it increases from 485 nm to 542 nm, near the wavelength of resonance for the scattering efficiency, see Fig. 3.2c). Similarly, for the SE and SI cases the amplitude of the far-field is modulated by its scattering efficiency as it can be seen from comparing the radiation patterns in Fig. 3.4 at 400 nm (black), 480 nm (blue) and 527 nm (purple), with the value of Q_{sca} at those wavelengths corresponding to a global maximum, a global minimum and a local maximum at the wavelength of resonance, respectively [see Fig. 3.2c)].

The shape of the radiation pattern of a 12.5 nm AuNP in the presence of a substrate, either embedded or supported, resembles that of the isolated 12.5 nm AuNP discussed in Section 1.2.3.2 [see Fig. 1.5] in that it follows a two-lobe and a one-lobe pattern depending on the

orientation of \mathbf{E}^i relative to the scattering plane. If the incident electric field is parallel to the scattering plane, a two-lobe pattern aligned to the direction \mathbf{k}^i of the incident—and transmitted—plane wave arises as it can be seen in the Figs. 3.3a) and 3.3c) for the EE case, and Figs. 3.4a) and 3.4c) for the EI scenario. Contrastingly, when the incident electric field is perpendicular to the scattering plane, the one-lobe pattern can be identified [see Figs. 3.3b) and 3.3d) (SE), and 3.4b) and 3.4d) (SI)]. By comparing the Mie-limiting radiation pattern (see Fig. 1.5) with the radiation patterns considering a substrate, the later loses the polar symmetry observed in the Mie-limiting case. In particular, the amplitude of $\mathbf{E}_{\text{far}}^{\text{sca}}$ is larger when evaluated at the medium of incidence than at medium of transmission; this asymmetry is observed for both illuminating configurations (external and internal) and it does not depend on whether the AuNP is supported or embedded. Rather, the spatial configuration of the system determines the overall value of the far-field: when the AuNP is embedded, the far-field amplitude is greater by a factor of 2.5 than when the AuNP is supported—see the axis scale in Figs. 3.3 and 3.4; this phenomenon is a consequence of the two following physical mechanisms. The first one is the substrate having a greater refractive index than the matrix, thus making the optical response of the 12.5 nm AuNP as that of a larger NP—but still small compared to the illuminating wavelength—as in the Mie-limiting case. The second mechanism is the relative alignment of the electric point dipole induced within the AuNP—small particle approximation to the AuNP—and the induced electric dipole due to the interface, which is parallel when the AuNP is embedded into the substrate and antiparallel when supported on it, thus leading to a more energetic configuration when the AuNP is located inside the substrate than inside the matrix.

The radiation pattern, an optical property observed in the far-field regime, is a manifestation of the near-field spatial distribution—see the footnote on page 50—which can be calculated numerically through the FEM for a AuNP of radius $a = 12.5$ nm. The scattered electric field in the far-field regime of a AuNP embedded or supported [Figs. 3.3 and 3.4] share some characteristics with the radiated field of an isolated AuNP (Mie-limiting case), and thus it should be for the near-field. In Fig. 3.5 it is shown the magnitude of the induced electric field \mathbf{E}^{ind} when the AuNP is illuminated by a y -polarized incident electric field \mathbf{E}^i traveling in the \mathbf{k}^i direction, perpendicular to the interface between air and glass; the induced electric field is evaluated at the scattering plane $x = 0$, that is, the incident electric field has only a parallel contribution \mathbf{E}_{\parallel}^i to the scattering plane. The wavelength λ of the incoming plane wave is $\lambda = 535.2$ nm for an embedded AuNP either illuminated externally [Fig. 3.5a)] or internally [Fig. 3.5b)] and $\lambda = 510$ nm for a supported AuNP either illuminated externally [Fig. 3.5c)] or internally [Fig. 3.5d)], which correspond to the wavelengths of the Localized Surface Plasmon Resonance (LSPR), that is, at the wavelength of maximum absorption.

The spatial distribution of the near-field shown in Fig. 3.5 is consistent with the description and explanation of both the absorption and scattering efficiencies [Figs. 3.2b) and 3.2c)] and the radiation patterns of the embedded [Fig. 3.3] and the supported [Fig. 3.4] AuNP. The induced electric field is, in general, stronger when the AuNP is embedded in the substrate than when it is supported on it, as can be seen in the magnitude of the hotspots around the AuNP: reddish regions in Figs. 3.5a) and 3.5b) and bluish in Figs. 3.5c) and 3.5d). These hotspots also verify that at the resonance wavelength, the main contribution to the electric fields is due to an electric dipolar moment since the characteristic two-lobe distribution of the near-field can be easily identified nevertheless, the lobes are not horizontally aligned to the AuNP's equator but farther from the substrate for the embedded AuNP and closer to it for the supported AuNP, as if the

3. RESULTS AND DISCUSSION

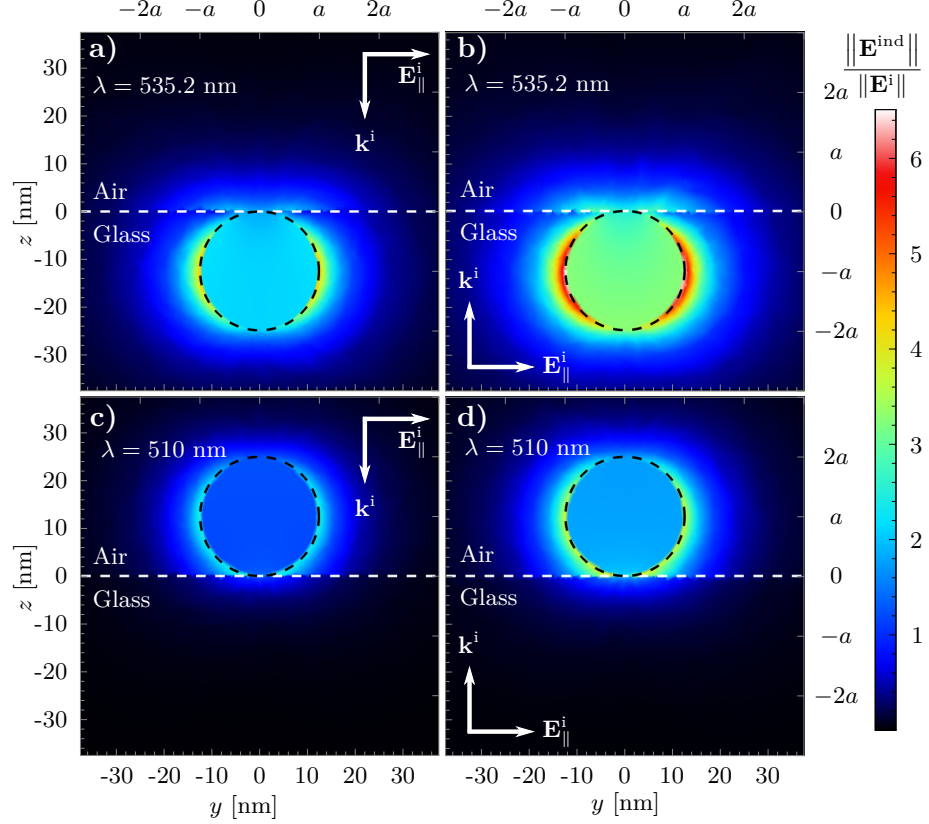


Fig. 3.5: Magnitude of the electric field induced \mathbf{E}^{ind} by a 12.5 nm AuNP (dashed black lines) illuminated by an incident electric plane wave \mathbf{E}^i traveling in the \mathbf{k}^i direction perpendicular to the interface (dashed white lines) between an air matrix ($n_m = 1$) and a glass substrate ($n_s = 1.5$) when the AuNP is **a,b**) embedded in the glass substrate and **c,d**) supported on it; the system is illuminated **a,c**) in an external and **b,d**) in an internal configuration at the resonance wavelength for the absorption efficiency.

induced dipole —in the small particle approximation, where the AuNP is treated as an electric point dipole— is parallel (perpendicular) to the dipolar moment induced in the AuNP when it is embedded in (supported on) the substrate, as discussed above.

Throughout this Section, the optical properties of a 12.5 nm AuNP on the presence of a substrate considering four configurations were studied: the AuNP either embedded or supported and the system illuminated from under the substrate or from above. The choice of normal incidence to the system allowed the obtained results to be compared with the Mie-limiting case, which lead to the identification of similarities and differences among the four configurations. The differences in the optical response are associated to the broken symmetry due to the two semiinfinite media now considered [11], while the similarities arise since the system is always illuminated by a plane wave independently of the choice of the medium of incidence, yielding a mostly dipolar electric field. Therefore, in the next Section the oblique incidence case is addressed only when the AuNP is supported and illuminated in the internal configuration, since it is the only case with a different type illumination to the system: an evanescent wave for incidence angles above the critical angle $\theta_c = \arcsin(n_m/n_s)$ [26].

3.1.2 Supported Spherical Particle in Total Internal Reflection

In the past Section, the AuNP of radius $a = 12.5$ nm was illuminated at normal incidence in four different spatial configurations considering the presence of a substrate: the AuNP either embedded in the substrate (with a refractive index n_s) or supported on it embedded in an air matrix (with refractive index n_m), and the incident electric field illuminating the system from the substrate (internal configuration) or from the matrix (external configuration). By considering that the incident electric plane wave \mathbf{E}^i propagates from the substrate to the matrix at an angle θ_i , relative to the normal direction to the interface between the two media, the electric field interacting with the AuNP is the transmitted field, that propagates at a transmission angle $\theta_t = \arcsin(n_m \sin \theta_i / n_s)$ [26] and two differences arise when compared with the normal incidence cases: there are two different polarization states for \mathbf{E}^i — s and p polarizations²— and if θ_i is greater than the critical angle θ_c the transmitted electric field becomes an evanescent wave propagating along the interface [26]. Similarly to the past Section, the optical properties of the supported AuNP illuminated at an oblique incidence in an internal configuration are studied by analyzing the absorption and scattering efficiencies, the radiation pattern and, lastly, the induced electric field on the AuNP.

In Fig. 3.6 the absorption Q_{abs} [Fig. 3.6a)] and scattering Q_{sca} [Fig. 3.6b)] efficiencies of a 12.5 nm AuNP in air ($n_m = 1$) supported on a glass substrate ($n_s = 1.5$) are shown as a function of the wavelength λ of the incident electric field \mathbf{E}^i , illuminating the AuNP from the substrate at an incidence angle θ_i of 15° (black), 38° (orange), 42° (blue) and 75° (light orange) considering an s (filled circles/solid lines) and a p (empty circles/dashed lines) polarization for \mathbf{E}^i . Since the critical angle for a glass-air interface is $\theta_c = 41.8^\circ$, the blue and light orange curves show the results of the interaction between an evanescent wave and the AuNP. The magenta markers correspond to the values of Q_{abs} and Q_{sca} evaluated at the wavelength of resonance; the Mie-limiting cases (AuNP embedded in air and in glass) are signalized by the boundaries of the green shaded region and the cyan markers correspond to the resonances of their efficiencies.

A general behavior on both the absorption and scattering efficiencies is that their magnitude for all considered values of λ , with a fixed polarization state, increases as the angle of incidence reaches the critical angle 41.8°, as it can be seen by comparing the black, orange — $\theta_i = 15^\circ$, $38^\circ < \theta_c$ — and blue — $\theta_c < \theta_i = 42^\circ$ — curves, and they decrease in the interval $\theta_c < \theta_i < 90^\circ$, which is noticeable by comparing the aforementioned curves with the light orange one — $\theta_i = 75^\circ$ —. This tendency is due to the transmitted electric field which illuminates the AuNP and it is described by a plane wave for $\theta_i < \theta_c$ and by an evanescent wave for $\theta_i > \theta_c$ according to the Fresnel's transmission amplitude coefficients, whose real part are monotonically increasing (decreasing) functions of θ_i for values smaller (greater) than the critical angle. Yet, another way to understand the decreasing behavior after the critical angle is due to the penetration depth of the evanescent electric field, which is given by $\lambda/(2\pi n_s \sin \theta_i)$, which is maximum at $\theta_i = \theta_c$ and decreases as θ_i grows.

When comparing the absorption and scattering efficiencies based on the polarization of the incident plane wave, it can be observed that their enhancement, relative to the Mie-

²The s and p polarization states of the electric field are defined by considering its oscillations perpendicular and parallel to the incidence plane, respectively, defined by the propagating direction of the incident electric plane wave and the normal direction to the interface between the substrate and the matrix [20].

3. RESULTS AND DISCUSSION

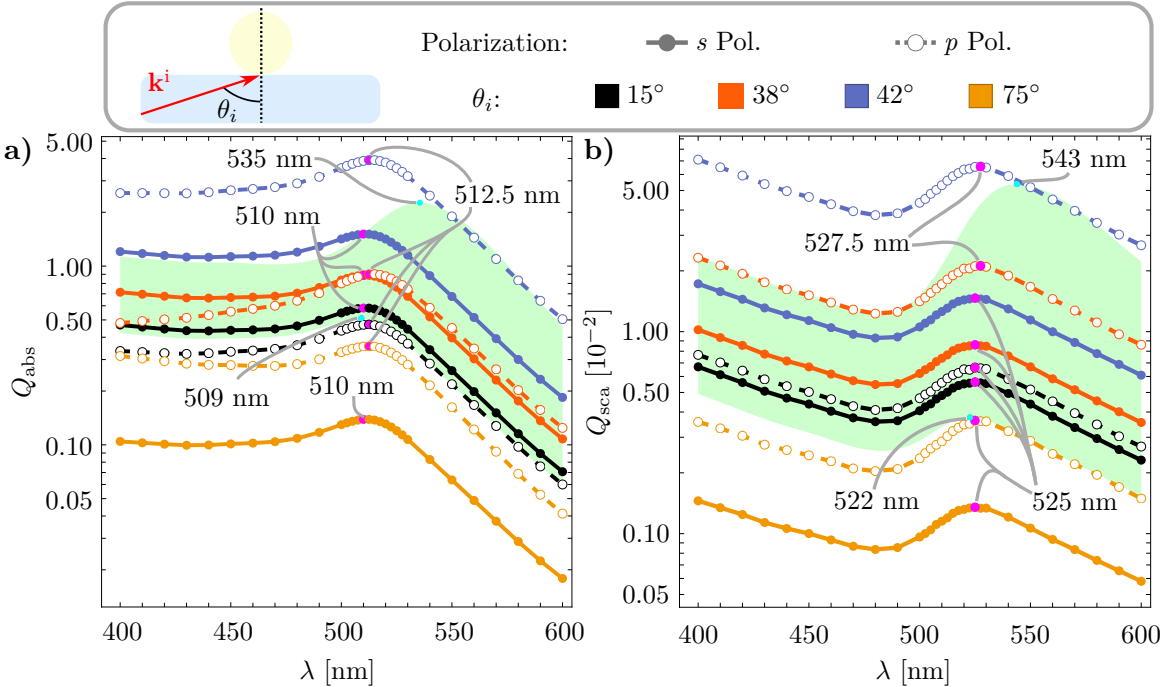


Fig. 3.6: a) Absorption and b) scattering efficiencies of a 12.5 nm AuNP in an air matrix ($n_m = 1$) and supported on a glass substrate ($n_s = 1.5$) as a function of the wavelength λ of an *s* (filled circles/solid lines) and a *p* (empty circles/dashed lines) polarized incident electric plane wave propagating in the direction of the wave vector \mathbf{k}^i , in an internal configuration, at an angle of incidence θ_i of 15° (black), 38° (orange), 42° (blue), and 75° (light orange) relative to the normal direction to the glass-air interface. The green shaded region shows the two Mie-limiting cases of a AuNP embedded in air and in glass; the magenta (supported AuNP) and cyan (Mie-limiting) markers correspond to the efficiencies evaluated at the wavelength of resonance for each case.

limiting case of a AuNP in an air matrix, is greater for a *p* than for an *s* polarized incident electric field for a fixed angle of incidence (see continuous and dashed curves of the same color). Another notable phenomenon is that the efficiencies for $\theta_i = 75^\circ$ (light orange curves) are below the Mie-limiting case for all wavelengths, while only the efficiencies for *p* polarized incident electric field with $\theta_i = 42^\circ \gtrsim \theta_c$ (dashed blue curves) are greater than the glass Mie-limiting case, particularly at the resonance wavelength. The last difference between the *s* and the *p* polarizations arises by analyzing the spectral shift of the LSPR (magenta markers), which are excited at the same wavelength —within the spectral resolution of the FEM simulation³— for a fixed θ_i and polarization state. For example, the wavelength of maximum absorption for the *s* polarized incident electric field is ~ 510 nm, which is the same as the equivalent system illuminated at normal incidence [see Fig. 3.2b)], while the LSPR for the *p* polarization case is excited at the larger wavelength ~ 512.5 nm. To better understand the spectral shift between the two polarization states, the induced electric field in the far and near-field regimes are analyzed.

The radiation pattern of the 12.5 nm AuNP embedded in air and supported on a glass substrate is shown in Fig. 3.7 when an *s* polarized [Figs. 3.7a) and 3.7b)] and a *p* polarized

³The FEM simulations in Fig. 3.6 were performed considering $400 \text{ nm} \leq \lambda \leq 600 \text{ nm}$ with a discretization of $\Delta\lambda$ in the neighborhood of the LSPR.

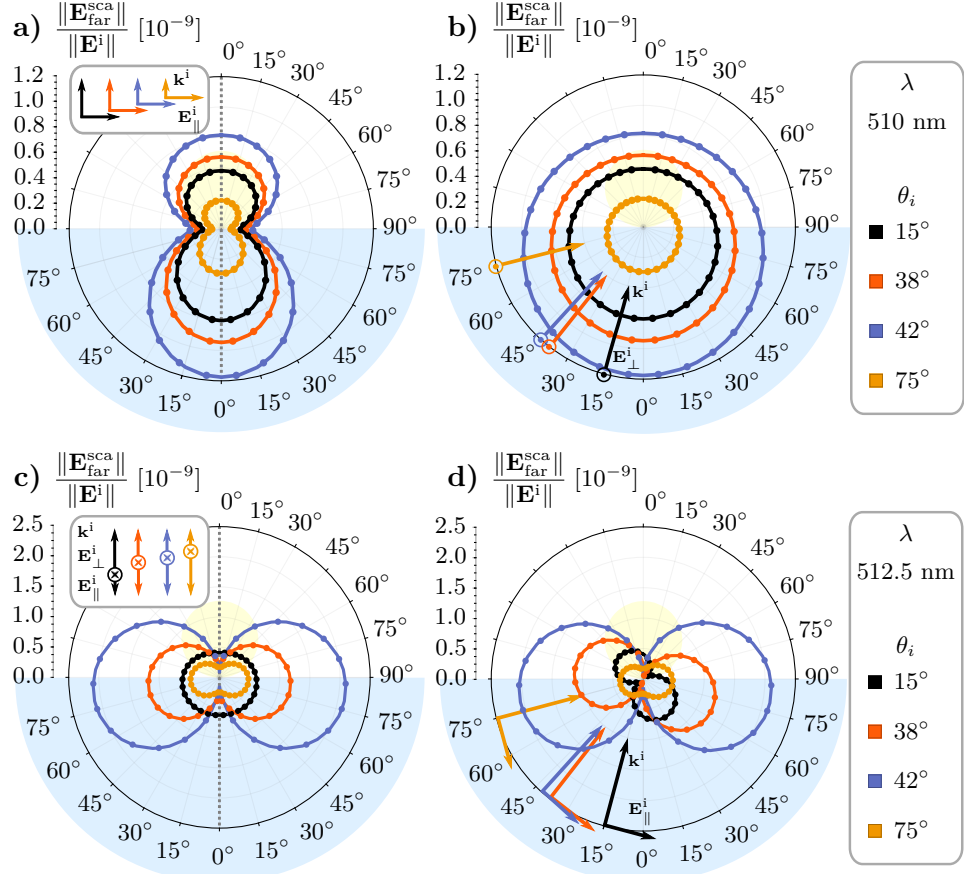


Fig. 3.7: Radiation patterns of a AuNP (light yellow) of radius $a = 12.5$ nm supported on a glass substrate (light blue, $n_s = 1.5$) with an air matrix ($n_m = 1$) illuminated by an incident electric plane wave \mathbf{E}^i , with a wavelength λ , traveling in the \mathbf{k}^i direction at an angle of incidence θ_i of 15° (black), 38° (orange), 42° (blue), and 75° (light orange) relative to the normal direction to the glass-air interface. The radiation patterns consider an **a,b**) *s* polarized and a **c,d**) *p* polarized incident electric field and the scattering plane **a,c**) perpendicular to the incidence plane (vertical gray dotted lines) and **b,d**) equal to the incidence plane. In all cases the incident wave vector \mathbf{k}^i , the perpendicular \mathbf{E}_{\perp}^i and the parallel \mathbf{E}_{\parallel}^i projection of the incident electric field relative to the scattering plane are schematized.

[Figs. 3.7c) and 3.7d)] incident electric field \mathbf{E}^i illuminates the AuNP at an incidence angle of $\theta_i = 15^\circ$ (black) and $\theta_i = 38^\circ$ (orange) —below the critical angle $\theta_c = 41.8^\circ$ —, and $\theta_i = 42^\circ$ (blue) and $\theta_i = 75^\circ$ (light orange) —above θ_c — in an internal configuration at the wavelength of resonance of the absorption efficiency —magenta markers in Fig. 3.6a)— for each case, which corresponds to the LSPR. The scattering plane where the radiation pattern is shown in Figs. 3.7a) and 3.7c) is perpendicular to the incidence plane (vertical gray dotted lines) while the scattering plane overlaps the incidence plane in Figs. 3.7b) and 3.7d); the incident wave vector \mathbf{k}^i and the components of the incident electric field parallel \mathbf{E}_{\parallel}^i and perpendicular \mathbf{E}_{\perp}^i to the scattering plane are schematized in all cases.

As expected from the results in Section 3.1.1, the amplitudes of the radiation patterns for AuNP supported on a substrate and illuminated in an internal configuration at an oblique

3. RESULTS AND DISCUSSION

incidence are modulated by the absorption and scattering efficiencies. For example, the maximum value of the radiation pattern for the *s* polarization case is 1.2 [see Figs. 3.7a) and 3.7b)] while this value is twofold for the *p* polarization case [see Figs. 3.7c) and 3.7d)]. Additionally, the radiation patterns for a fixed angle of incidence present a larger maximum value the greater the absorption and scattering efficiencies are, as it can be seen by comparing the blue and light orange curves—corresponding to $\theta_i = 42^\circ$ and $\theta_i = 75^\circ$, respectively—in Fig. 3.7 with the curves in Fig. 3.6.

Focusing on the shape of the radiation patterns, the *s* polarization case shows a two and a one-lobe shapes if the incident electric field is parallel [Fig. 3.7a)] or perpendicular [Fig. 3.7b)] to the scattering plane, respectively. Such radiation patterns are observed for all values of θ_i in an *s* polarization configuration due to the continuity of the component of the electric field parallel the substrate where the AuNP is supported on. On the other hand, for a *p* polarized incident electric field, the transmitted electric field illuminating the AuNP has a different component perpendicular to the substrate depending on the angle of incidence; the orientation of the transmitted electric field, relative to the normal direction to the substrate, is obtained by adding $-\pi/2$ to the angle of transmission $\theta_t = \arcsin(n_m \sin \theta_i / n_s)$, that is $\theta_t - \pi/2$. The direction of the transmitted electric field for an incidence angle $\theta_i = 15^\circ < \theta_c$ and $\theta_i = 38^\circ < \theta_c$ —black and orange curves—result in the two-lobe shape shown in Fig. 3.7c)—scattering plane perpendicular to the incidence plane—and Fig. 3.7d)—scattering plane overlapping the incidence plane—. When the scattering and incidence planes are perpendicular to each other, the transmitted electric field have components both parallel and perpendicular to the scattering plane for $\theta_i < \theta_c$ yielding radiation patterns without non-radiation directions, while the radiation patterns when the scattering and the incidence planes overlap there are two-lobe shapes rotated with no-radiation directions given by the transmission angle θ_t . For $\theta_i > \theta_c$, the transmitted electric field is described by an evanescent wave traveling along the interface and its direction is perpendicular to the substrate, thus the two-lobe shape of the AuNP’s radiation pattern is aligned to the interface; this can be observed when $\theta_i = 42^\circ$ (blue curve) and $\theta_i = 75^\circ$ (light orange curve) when the scattering and the incidence plane are perpendicular between them [Fig. 3.7c)] and when they overlap [Fig. 3.7d)].

The behavior of the scattered electric field by the AuNP, in the far-field regime, described above suggests that a 12.5 nm AuNP on a substrate can be studied in the small particle approximation and be treated, even at oblique incidence, as an electric point dipole oriented parallel to the substrate for an *s* polarized incident electric field and in a perpendicular direction to that given by the transmission angle for the *p* polarization case. Under such scheme, alongside the interaction between the electric point dipole and an image electric dipole induced within the substrate, the difference in magnitude of the efficiencies, and thus of the far-field, for different polarization states of the incident electric field, is understood since for *s* polarization the point electric dipole and the image electric dipole are parallel to each other, while for *p* polarization the dipoles are collinear to each other, that is, they have a stronger response [51].

To further analyze the optical response of the AuNP on a substrate, the spatial distribution of the induced electric field \mathbf{E}^{ind} —the internal and the scattered electric field in the near-field regime—is needed. Since the radiation patterns observed when an *s* polarized incident electric field illuminates the AuNP follow the same one and two-lobe shapes for all the considered combinations of θ_i and λ only differing in the magnitude, the distribution of \mathbf{E}^{ind} have the same qualitative behavior for all incident angles at this polarization state. Therefore, the magnitude

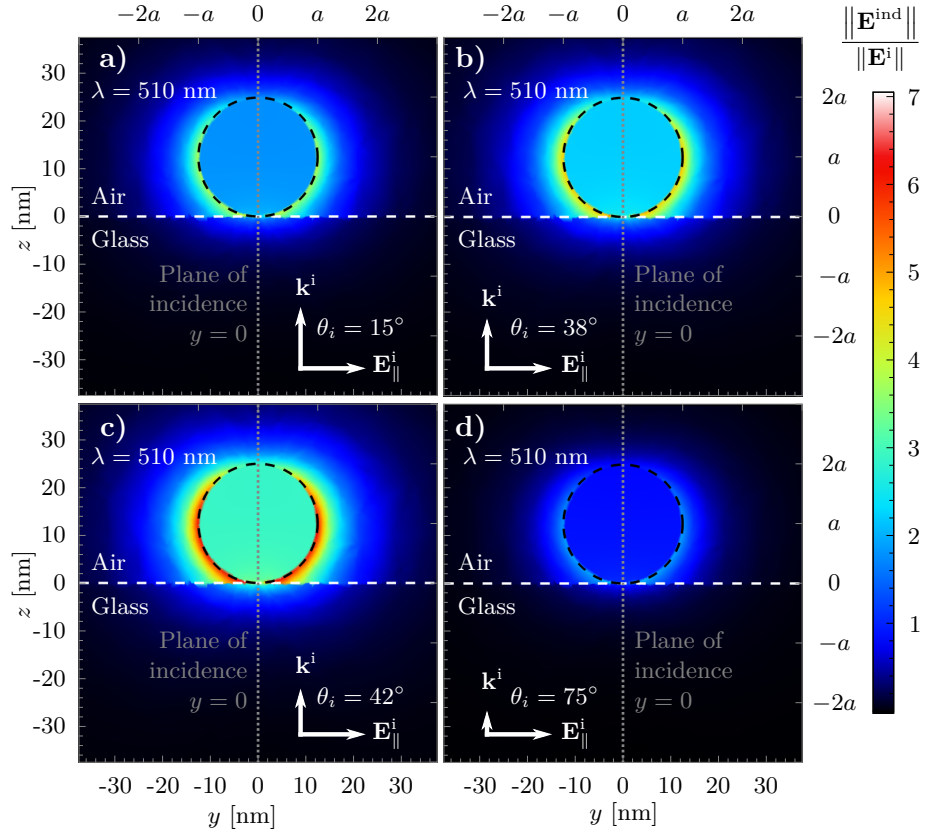


Fig. 3.8: Magnitude of the electric field induced \mathbf{E}^{ind} by a supported 12.5 nm AuNP (dashed black lines) illuminated by an s polarized incident electric plane wave \mathbf{E}^i traveling in the \mathbf{k}^i direction, in an internal configuration, at an angle of incidence of **a)** 15° , **b)** 38° , **c)** 42° , and **d)** 75° , relative to the normal direction to the interface —white dashed lines— between an air matrix ($n_m = 1$) and a glass substrate ($n_s = 1.5$). The incident electric plane wave is evaluated at $\lambda = 510 \text{ nm}$ —resonance wavelength of the absorption efficiency— and in all cases the scattering plane is perpendicular to the incidence plane (vertical gray dotted lines).

of the induced electric field \mathbf{E}^{ind} , evaluated at a scattering plane perpendicular to the incidence plane (vertical gray dashed lines) is shown in Fig. 3.8 for a 12.5 nm AuNP (black dashed lines) supported on the interface between a glass substrate and an air matrix (white dashed lines) when the incident electric field \mathbf{E}^i illuminates the system at an incident angle of 15° [Fig. 3.8a)], 38° [Fig. 3.8b)], 42° [Fig. 3.8c)], and 75° [Fig. 3.8d)].

Contrastingly to the s polarized incident electric field case, the radiation patterns of a supported 12.5 nm AuNP illuminated with a p polarized electric field have a different qualitative behavior depending on the angle of incidence θ_i , as shown in Figs. 3.7c) and 3.7d). Thus, the magnitude of \mathbf{E}^{ind} is shown in Fig. 3.9 and it is evaluated at scattering plane perpendicular to the incidence plane (vertical gray dotted line) [Figs. 3.9a), 3.9c), 3.9e) and 3.9g)] and at the incidence plane [Figs. 3.9b), 3.9d), 3.9f) and 3.9h)] for an incidence angle $\theta_i = 15^\circ$ [Figs. 3.9a) and 3.9b)] and $\theta_i = 38^\circ$ [Figs. 3.9c) and 3.9d)], both below the critical angle $\theta_c = 41.8^\circ$, and $\theta_i = 42^\circ$ [Figs. 3.9e) and 3.9f)] and $\theta_i = 75^\circ$ [Figs. 3.9g) and 3.9h)] above θ_c .

In both figures, Fig. 3.8 and Fig. 3.9, it can be seen that the greater enhancement of

3. RESULTS AND DISCUSSION

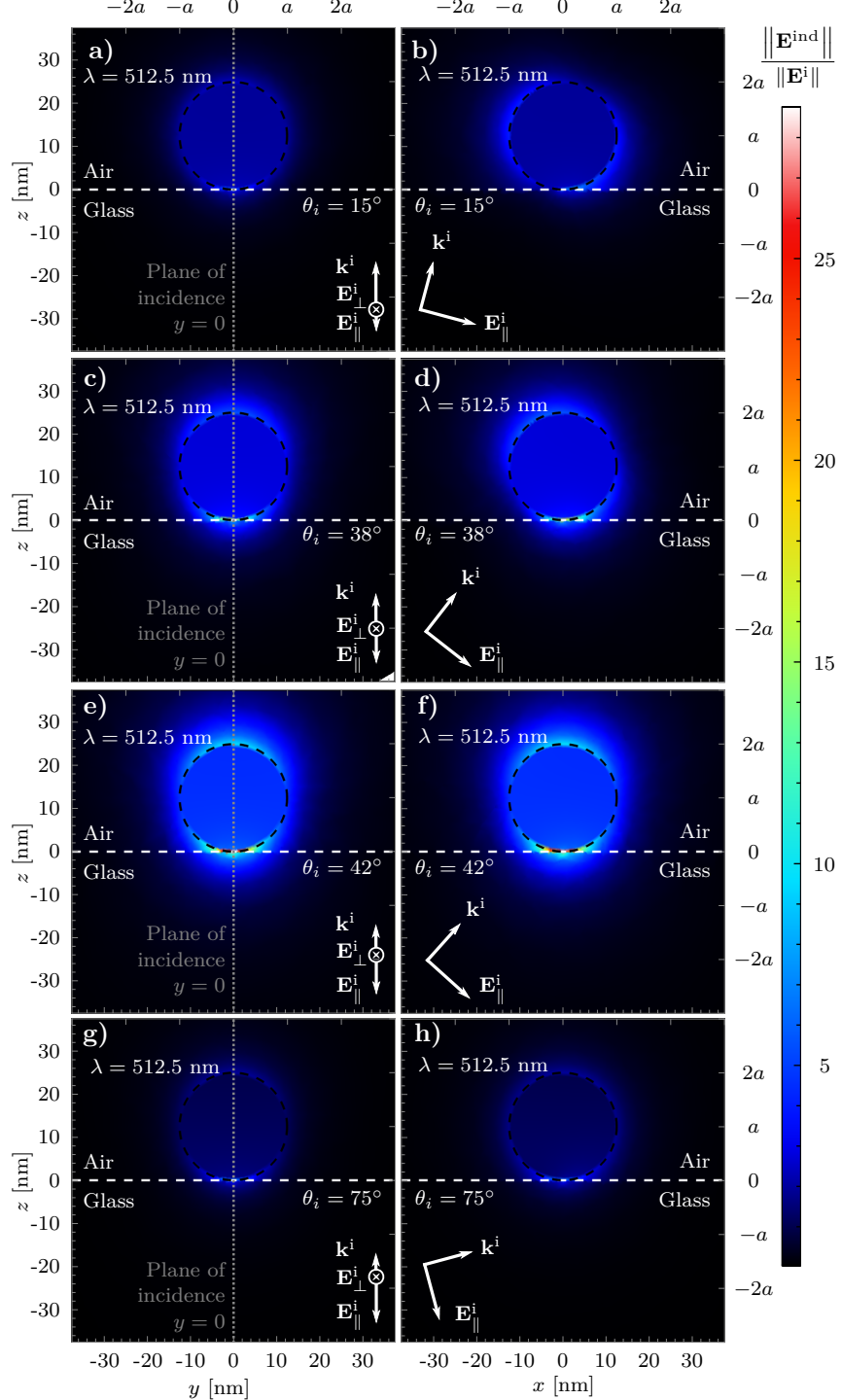


Fig. 3.9: Magnitude of the electric field induced \mathbf{E}^{ind} by a supported 12.5 nm AuNP (dashed black lines) illuminated by a p polarized incident electric plane wave \mathbf{E}^i traveling in the \mathbf{k}^i direction, in an internal configuration, at an angle of incidence of **a,b)** 15° , **c,d)** 38° , **e,f)** 42° and **g,h)** 75° , relative to the normal direction to the interface —white dashed lines— between an air matrix ($n_m = 1$) and a glass substrate ($n_s = 1.5$). The incident electric plane wave is evaluated at the resonance wavelength of the absorption efficiency —see Fig. 3.6a)— and in all cases $\|\mathbf{E}^{\text{ind}}\|$ is evaluated at **a,c,e,g)** the scattering plane perpendicular to the incidence plane (vertical gray dotted lines) and at **b,d,f,h)** the scattering plane equal to the incidence plane.

electric field occurs when the angle of incidence is $\theta_i = 42^\circ \gtrsim \theta_c$ [see Figs. 3.8c), 3.9e) and 3.9f)] for each polarization and the lesser enhancement for θ_i close to 90° [see Figs. 3.8d), 3.9g) and 3.9h)], in agreement with the tendency of the absorption and scattering efficiencies and the radiation patterns presented above. On the spatial distribution, the induced electric field for an *s* polarized incident electric field [Fig. 3.8], the characteristic dipolar distribution with hotspots aligned to the substrate is shown with a deviation close to the substrate, as observed in the normal incidence case, while for the *p* polarization case [Fig. 3.9] the hotspots of the near-field spatial distribution are rotated according to the orientation of the transmitted electric field. This rotation of the spatial distribution of the magnitude of \mathbf{E}^{ind} leads to an enhancement of ~ 30 when $\theta_i \gtrsim \theta_c$ since one hotspot is in contact with the substrate, nevertheless on the diametral hotspot is ~ 12.5 , which is still larger than for the equivalent *s* polarization case.

In this Section, the optical properties of a 12.5 AuNP in air and supported on a glass matrix was studied when illuminated at normal and oblique incidence for both polarization states of the incident electric field. It was observed that there is an enhancement of the absorption and scattering efficiencies of the AuNP relative to the Mie-limiting case and a redshift of the LSPR due to the substrate which is polarization dependent but not angle of incidence dependent. On the other hand, the near and far scattered electric field induced by the AuNP interacting with the transmitted electric field showed a different behavior according to the polarization of the incident electric field and on the angle of incidence since the transmitted electric field is described by a plane or by an evanescent wave if the angle of incidence is smaller or greater than the critical angle, respectively. Lastly, it was shown that when the AuNP is illuminated by an evanescent wave, the overall optical response of the AuNP is stronger and if the system is illuminated by a *p* polarized incident electric field, there is an induced dipolar moment perpendicular to the substrate which describes this optical response. In the next Section, a similar analysis is performed but now considering that the AuNP is partially embedded in the substrate, which corresponds to a more realistic experimental system.

3.2 Partially Embedded Spherical Particle

When studying the optical properties of ensembles of NPs, a series of assumptions and simplifications are done in order to theoretically describe their optical response. For example, the van de Hulst [52] and the Maxwell Garnett [15] models for an effective dielectric function of colloidal three dimensional mixtures require not only the NPs to be perfectly spherical (and small compared to the incident wavelength for the later), but also a low concentration of NPs in the ensemble, which yields the Single Scattering Approximation to be valid and thus the results from the Mie Theory —Section 1.2— can be exploited. When the optical properties of bidimensional arrays of NPs are of interest, one assumption common to several models, besides the aforementioned, is that the NPs are perfectly supported on the substrate, as it is the case for example in the Thin Island Theory [13], the Dipolar Model [14], and the Coherent Scattering Model [53]. While some of these assumptions can be experimentally achieved, such as the size of the NPs and their low concentration in an ensemble [54], a partial embedding of the NP into a substrate is not only a possible outcome of the fabrication process [11] but sometimes it is a desirable feature of the bidimensional array of NPs for its use in applications, for example, in low-cost plasmonic biosensors [17], where the partial embedding diminishes the washability of

3. RESULTS AND DISCUSSION

the sample.

The theoretical approach employed by the Thin Island Theory, the Dipolar Model and the Coherent Scattering Model involves the optical properties of a single scatterer in a surrounding isotropic medium to later introduce the effect of both the multiple scattering due to the ensemble of NPs and the presence of the substrate. Thus, an attempt to extend the validity of such models for more realistic conditions by considering the partial embedding of the nanospheres would require to determine the optical properties of single nanospheres as they are buried into the substrate. In the following Sections, the absorption and scattering efficiencies, as well as the induced electric field in the far and near-field regimes, are studied for a 12.5 nm AuNP partially embedded considering an air matrix and a glass substrate.

3.2.1 Normal Incidence

To study the optical properties of a partially embedded spherical AuNP into a substrate forming a planar interface with a matrix, the incrustation parameter is introduced, which is defined as the ratio h/a , where h is the vertical position of the center of the AuNP relative to the interface and a its radius, as it can be seen in Fig. 3.10. The choice of the incrustation parameter is based on the volume $V_{\text{sph}}^{\text{sub}}$ (surface $S_{\text{sph}}^{\text{sub}}$) fraction of the AuNP partially embedded relative to the total volume V_{sph} (surface S_{sph}) of the AuNP obeying the relation $V_{\text{sph}}^{\text{sub}}/V_{\text{sph}} = S_{\text{sph}}^{\text{sub}}/S_{\text{sph}} = (1 - h/a)/2$. Such a definition of the incrustation parameter h/a characterizes the totally supported and totally embedded AuNP —see Section 3.1.1— by the values 1 and -1 , respectively, while in general if $h/a > 0$ it is understood that most of the AuNP is located in the matrix and if $h/a < 0$ most of the AuNP is buried in the substrate.

In Fig. 3.10 the absorption Q_{abs} [Fig. 3.10a)] and scattering Q_{sca} [Fig. 3.10b)] efficiencies of a 12.5 nm AuNP partially embedded in a glass substrate ($n_s = 1.5$) forming a planar interface with an air matrix ($n_m = 1$), are shown as a function of the wavelength λ of the incident electric field \mathbf{E}^i illuminating the system at normal incidence in an internal configuration—as shown in Fig. 3.10—for several values of the incrustation parameter. The magenta markers correspond to the values of Q_{abs} and Q_{sca} evaluated at the wavelength of resonance and the black, light brown, and purple curves correspond to the limiting values of h/a equal to 1 (totally supported NP), -1 (totally embedded NP) and 0 (half of the NP in the substrate and half in the matrix). To compare the obtained results, the Mie-limiting cases (AuNP embedded in air and in glass) are signalized in Fig. 3.10 by the boundaries of the green shaded region and the cyan markers correspond to the resonances of their efficiencies; the gray dashed lines are guides to the eye.

Both the absorption and the scattering efficiencies for partially embedded 12.5 AuNP present an increase for all wavelengths as the AuNP is buried into the substrate, that is, as the incrustation parameter changes from 1 to -1 . Additionally, the absorption wavelength of resonance is redshifted increasingly from 510 nm to 532.5 nm, as it can be seen from the gray dashed line joining the magenta markers for Q_{abs} with $h/a = 1$ (black curve) and $h/a = -1$ (light brown curve) in Fig. 3.10a). On the other hand, the wavelength of resonance for Q_{sca} presents an increasing redshift for its wavelength of resonance when h/a increases, except when the scattering efficiency of the partially embedded AuNP with $h/a = 0$ (purple curve) and with $h/a = 0.25$ (green curve) in Fig. 3.10b) are compared since for these two cases there is a blueshift

3.2 Partially Embedded Spherical Particle

of the resonance rather than a redshift; all of which is true up to the wavelength discretization of $\Delta\lambda = 2.5$ nm employed in the FEM simulations in the neighborhood of the resonances. Lastly, the absorption and scattering efficiencies for a partially embedded AuNP present only one resonance within the visible range that is spectrally located in between the resonances for the Mie-limiting cases (AuNP in an homogeneous matrix of air and of glass), therefore its optical properties can be mostly described by dipolar contribution, even if the homogeneity of its surroundings is broken as well as the symmetry of the system. To emphasize the last observation, the radiation pattern and the spatial distribution of the induced electric field are to be analyzed.

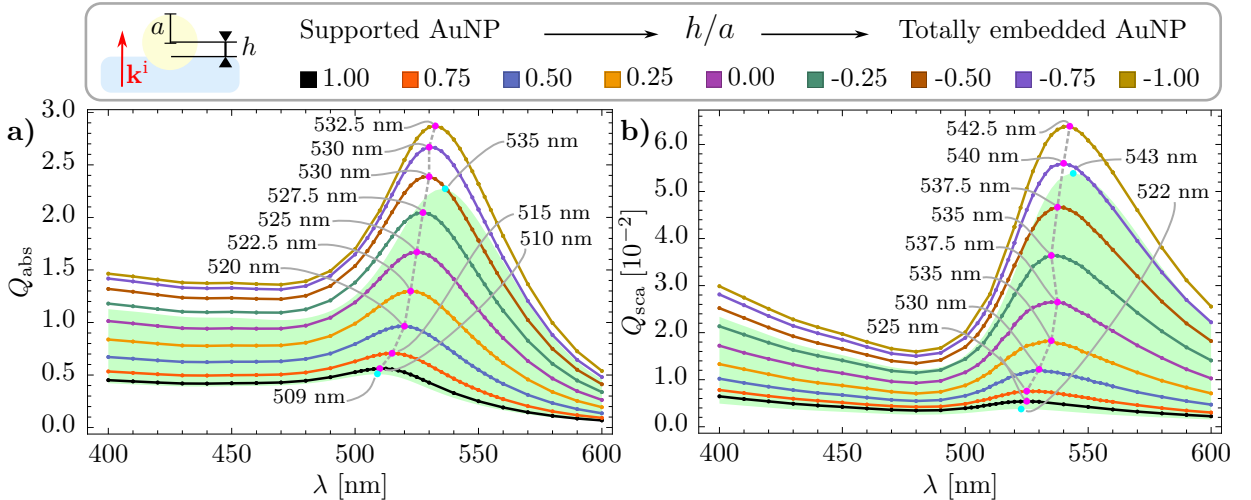


Fig. 3.10: a) Absorption and b) scattering efficiencies of a 12.5 nm AuNP partially embedded in a glass substrate ($n_s = 1.5$) with an air matrix ($n_m = 1$) as a function of the wavelength λ of the incident electromagnetic plane wave with a wave vector \mathbf{k}^i perpendicular to the glass-air interface. The partial embedding of the AuNP is determined by the ratio h/a with a the AuNP's radius and h the distance between the interface and the center of the AuNP. The green shaded region shows the two Mie-limiting cases of a AuNP embedded either in air or in glass; the magenta (partially embedded AuNP) and cyan (Mie-limiting) markers correspond to the efficiencies evaluated at the wavelength of resonance for each case; the gray dashed line is a guide to the eye.

The radiation patterns of a partially embedded AuNP in a glass substrate and an air matrix, when it is illuminated by a plane wave at normal incidence, are shown in Fig. 3.11 for several values of the incrustation parameter of h/a evaluated at the resonance wavelength of the LSPR [magenta markers in Fig. 3.10a)]. The radiation patterns are evaluated at the scattering planes considering an incident electric field parallel \mathbf{E}_{\parallel}^i [Fig. 3.11a)] and perpendicular \mathbf{E}_{\perp}^i [Fig. 3.11b)] to it. Additionally, the color code employed for each value of h/a is the same as in Fig. 3.10.

Similar to the radiation patterns at normal incidence for totally embedded and supported 12.5 nm AuNPs (Section 3.1.1), the radiation patterns of partially embedded AuNPs present the characteristic two and one-lobe shapes of dipolar radiation, with an asymmetrical behavior in the \mathbf{k}^i direction due to the presence of the substrate, when the incident electric field has a component only parallel and only perpendicular to it, as it can be seen in Figs. 3.11a) and 3.11b), respectively. Another common characteristic, already discussed in the past Sections, is that the average magnitude of the scattered electric field is modulated by the efficiencies shown in Fig. 3.10. For example, the AuNP with an incrustation parameter $h/a = -0.75$ (light purple

3. RESULTS AND DISCUSSION

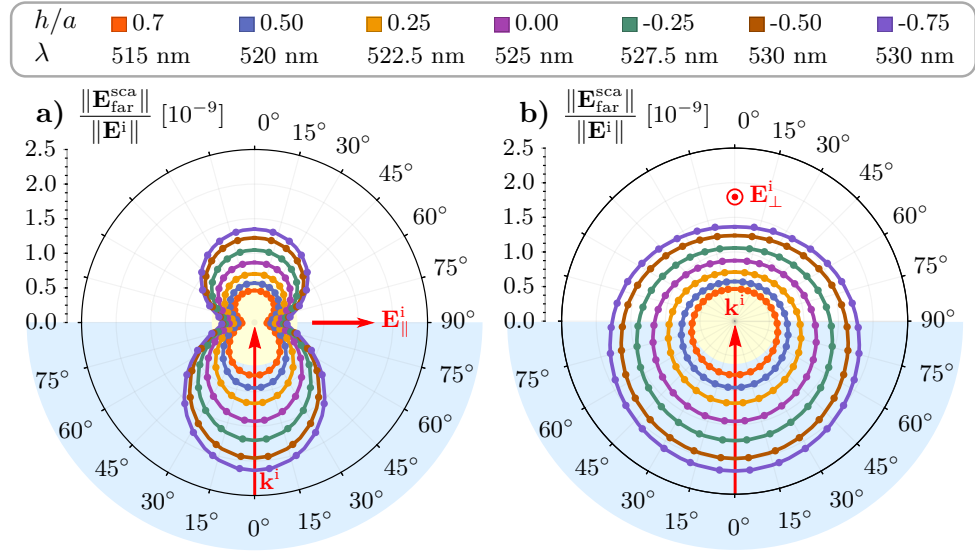


Fig. 3.11: Radiation patterns of a AuNP (light yellow) of radius $a = 12.5$ nm partially embedded in a glass substrate ($n_s = 1.5$, light blue) in an air matrix ($n_m = 1$) illuminated by an incident electric plane wave \mathbf{E}^i , with a wavelength λ traveling in the \mathbf{k}^i direction, normal to the glass-air interface. The radiation patterns consider the incident electric field **a)** \mathbf{E}_{\parallel}^i parallel to the scattering plane and **b)** \mathbf{E}_{\perp}^i perpendicular to it. The partial embedding of the AuNP is determined by the ratio h/a , with h the distance between the interface and the center of the AuNP and a its radius; each radiation pattern is evaluated at the wavelength of the LSPR shown in Fig. 3.10a).

curves) has a maximum amplitude in the far-field regime of ~ 2.3 while this value decreases to ~ 1.5 for $h/a = 0$ (purple curves), whose ratio resembles that of the absorption efficiencies of $\sim 2.7/1.6$ —see magenta markers in Fig. 3.10a)—for the same incrustation parameters. The overall behavior of the absorption and scattering efficiencies and of the radiation patterns from Figs. 3.10 and 3.11 suggests that the small particle approximation, where the 12.5 nm AuNP can be described as an electric point dipole, is still valid even if the AuNP is partially embedded so far it is illuminated normally to the glass-air interface, which can be confirmed by analyzing the induced electric field in the near-field regime.

In Fig. 3.12 it is shown the spatial distribution of the magnitude of the induced electric field \mathbf{E}^{ind} due to the interaction between a plane wave traveling normally to the interface between air and glass (horizontal white dashed lines), where a 12.5 nm AuNP (black dashed lines) is partially embedded with a incrustation parameter $h/a = 0.50$ [Figs. 3.12a) and 3.12b)], $h/a = 0$ [Figs. 3.12c) and 3.12d)], and $h/a = -0.50$ [Figs. 3.12e) and 3.12f)]. The magnitude of \mathbf{E}^{ind} is shown for the scattering plane parallel to the incident electric field [Figs. 3.12a), 3.12c), and 3.12e)] and perpendicular to it [Figs. 3.12b), 3.12d), and 3.12f)] considering that the incident electromagnetic plane wave has a wavelength λ equal to the wavelength of resonance for each case.

The spatial distribution of the induced electric field shows two hotspots for each value of the incrustation parameter considered—with a sixfold enhancement—when the incident electric field is parallel to the scattering plane [see reddish regions in Figs. 3.12a), 3.12c) and 3.12e)], which are not aligned to the equator of the AuNP but located on the surface of the AuNP

3.2 Partially Embedded Spherical Particle

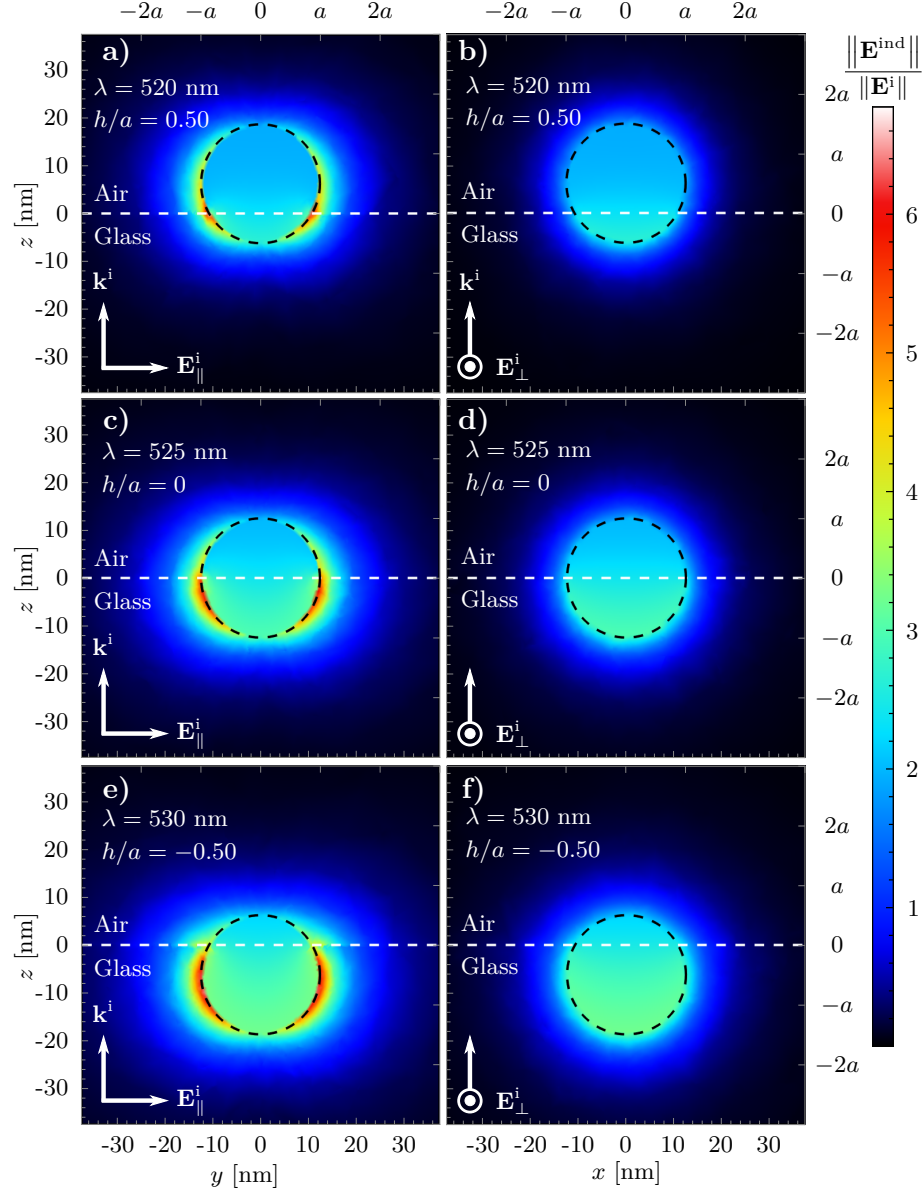


Fig. 3.12: Magnitude of the electric field \mathbf{E}^{ind} induced by a partially embedded 12.5 nm AuNP (dashed black lines) illuminated by an incident electromagnetic plane wave \mathbf{E}^i traveling in the \mathbf{k}^i direction perpendicular to the interface —white dashed lines— between an air matrix ($n_m = 1$) and a glass substrate ($n_s = 1.5$). The incident electromagnetic plane wave is evaluated at the resonance wavelength of the absorption efficiency —see Fig. 3.10a)— for an incrustation parameter h/a of **a,b)** 0.50, **c,d)** 0 and **e,f)** -0.50, and considering an incident electric field **a,c,e)** \mathbf{E}_\parallel^i parallel to the scattering plane and **b,d,f)** \mathbf{E}_\perp^i perpendicular to it.

embedded in the substrate. Such behavior was observed in Section 3.1.1 where the enhancement of the electric field was larger for the totally embedded AuNP. When the AuNP is partially embedded, the larger enhancement in the substrate is not only observed in the hostspots but also in the norm of the scattered electric field reaching a farther region in the glass substrate than in the air matrix, as it can be seen by comparing the bluish regions in Figs. 3.12b), 3.12d) and 3.12f), where the scattering plane is perpendicular to the incident electric field, above and below

3. RESULTS AND DISCUSSION

the white dashed lines. While this behavior of $\|\mathbf{E}^{\text{ind}}\|$ is common to all values of the incrustation parameter h/a , the effect of h/a can be identified in the localization of the hotspots and in the internal electric field inside the AuNP: the hotspots are less localized as h/a changes from 1 to -1 and the internal electric field is greater in the regions where the AuNP is in the substrate than in the matrix. The lesser localization of the hostspots the larger the incrustation parameter, is understood by taking into account the polarization of the materials (glass and air), while the magnitude of the gradient for the internal electric field is due to the boundary conditions on the AuNP's surface.

From the analysis of the absorption Q_{abs} and scattering Q_{sca} efficiencies (Fig. 3.10), and of the induced electric field in the far (Fig. 3.11) and near-field (Fig. 3.12) regimes, it was identified a similar behavior of the optical properties of a 12.5 nm AuNP when it is totally supported on (embedded in) a substrate than when the AuNP is partially embedded in bewteen the substrate and the matrix, for a normal incidence of an electromagnetic plane wave. Specifically, it was found that the optical properties of the AuNP can be mostly described by a dipolar contribution with any value of the incrustation parameter, whose effect is noticeable in a redshift of the LSPR and an enhancement of Q_{abs} and Q_{sca} as the AuNP is more embedded into the substrate, as well as a stronger scattered field in the far-field regime and larger hotspots in the near-field regime on the surface of the AuNP embedded in the substrate. The later, shows a disadvantage of the partial embedding of the AuNP for its possible application as a biosensor since the largest enhancement occurs at a spatial region inaccessible to any desired sample. In the following Section, the optical properties of partially embedded AuNP are studied at oblique incidence in order to find an optimal configuration where the partially embedded AuNP is suited for interactions in the matrix side.

3.2.2 Partially Embedded Spherical Particle in Total Internal Reflection

In the past Section, the optical properties of a spherical AuNP with radius $a = 12.5$ nm were studied when the AuNP was located at the interface between a glass substrate and an air matrix, and illuminated in the normal direction to the glass-air interface. On the one hand, it was found that the AuNP can be still described by a mostly dipolar contribution, as in the Mie-limiting case (AuNP in a homogeneous medium), even though the homogeneity and symmetry of its surroundings is broken. On the other hand, the near-field enhancement on the surface of the AuNP was greater in the side of the glass substrate than in the air matrix, which is undesired if the partially embedded AuNP is to be used as the unit cell for a bidimensional array suited for biosensing. In order to find an optimal configuration of the system suited for interactions above the substrate, in this Section the optical properties of a partially embedded AuNP are analyzed considering an oblique incidence to the system (both below and above the critical angle), meaning that the AuNP is illuminated either with an s or a p polarized incident electric field.

The absorption Q_{abs} and scattering Q_{sca} efficiencies of a partially embedded AuNP with radius $a = 12.5$ nm in a glass substrate ($n_s = 1.5$) and in an air matrix ($n_m = 1$) —for different values of the incrustation parameter h/a , with h the distance between the center of the AuNP and the interface— are shown in Figs. 3.13 and 3.14, respectively, as a function of the wavelength λ of the incident electric field \mathbf{E}^i illuminating the AuNP from the substrate at an incidence angle $\theta_i < \theta_c = 41.8^\circ$ of 15° [Figs. 3.13a) and 3.14a)] and 38° [Figs. 3.13b) and 3.14b)], and at a value

of $\theta_i > \theta_c$, thus forcing the interaction between an evanescent wave and the AuNP, equal to 42° [Figs. 3.13c) and 3.14c)] and 75° [Figs. 3.13d) and 3.14d)], considering an *s* (filled circles/solid lines) and a *p* (empty circles/dashed lines) polarization for \mathbf{E}^i . To compare the obtained results with the Mie-limiting cases (AuNP embedded in air and in glass)—green shaded region and cyan markers corresponding to the resonance of the absorption and scattering efficiencies—the values of Q_{abs} (Q_{sca}) evaluated at their wavelength of resonance $\lambda_{\text{res}}^{\text{abs}}$ ($\lambda_{\text{res}}^{\text{sca}}$) are signalized by the magenta markers and the numerical values of the later can be found in Table 3.1, where the saturation of the cell colors corresponds to a larger wavelength. Lastly, in Figs. 3.13 and 3.14 the gray continuous lines are a guide to the eye joining the resonances of the absorption and scattering efficiencies in each case considering an *s* and a *p* polarized incident electric field.

In Figs. 3.13 and 3.14 it can be seen that the absorption and scattering efficiencies, for each combination of θ_i and h/a , present a general redshift of the resonance wavelengths $\lambda_{\text{res}}^{\text{abs}}$ and $\lambda_{\text{res}}^{\text{sca}}$ as h/a decreases, while preserving only one appreciable resonance in the visible range in the intervals $509 \text{ nm} < \lambda_{\text{res}}^{\text{abs}} < 535 \text{ nm}$ and $522 \text{ nm} < \lambda_{\text{res}}^{\text{sca}} < 545 \text{ nm}$, whose extreme values (cyan markers) correspond to the resonance wavelength for the Mie-limiting cases: AuNP in air and in glass. Besides the redshift of the resonances, it is observed an overall growth—or decrease, depending on the choice of incrustation parameter and angle of incidence—for all wavelengths on the absorption and scattering efficiencies, which are integral optical properties and thus an average response of the system. Therefore, these changes can be identified as the combination of the effects due to the AuNP interacting with a plane or an evanescent wave, as discussed in Section 3.2.2, and due to the embedding of the AuNP, discussed in Section 3.2.1.

A general effect of the choice of θ_i on Q_{abs} and Q_{sca} is their enhancement, in the visible range, for incidence angles near the critical angle $\theta_c = 41.8^\circ$, as it can be seen from the absorption and scattering efficiencies, for both the *s* and *p* polarization cases, at $\theta_i = 42^\circ$ [Figs. 3.13c) and 3.14c)], which are larger, for all λ , than the equivalent results for incidence angles of 15° , 38° , and 75° . This observation can be verified by comparing the vertical axis scale with a maximum value of ~ 10.0 in Fig. 3.13c) and $\sim 10.1 \times 10^{-2}$ Fig. 3.14c)—absorption and scattering efficiencies, respectively—with the maximum value of the axis scale for $\theta_i = 15^\circ$ in Figs. 3.13a) (~ 1.2) and 3.14a) ($\sim 5.3 \times 10^{-2}$) and for $\theta_i = 38^\circ$ in Figs. 3.13b) (~ 4.1) and 3.14b) ($\sim 9.1 \times 10^{-2}$)—both angles below θ_c ; on a similar manner, the absorption and scattering efficiencies, for a fixed polarization state and incrustation parameter, are the smallest for $\theta_i = 75^\circ$ as shown by the maximum value of the vertical axes of ~ 1.0 in Fig. 3.13d) and of $\sim 1.0 \times 10^{-2}$ in Fig. 3.14d). A similar analysis based on the Mie-limiting cases can be performed by comparing the values of the continuous curves relative to the green shaded region, yielding the same results.

To notice the effect of the polarization state—modulated by the AuNP’s embedding—of the incident electric field \mathbf{E}^i in the absorption and scattering efficiencies, let us recall the behavior observed for a normally illuminated partially embedded AuNP in Section 3.2.1, where the values of Q_{abs} and Q_{sca} grew uniformly, for all wavelengths in the visible range, as the incrustation parameter h/a changes from 1 to -1 , that is, as the AuNP is buried into the substrate. Such behavior can be identified in the continuous gray curves for any angle of incidence in Figs. 3.13 (absorption efficiency) and 3.14 (scattering efficiency). This can be explained by the direction of the electric field not changing across the glass-air interface due to the continuity of the parallel component of the electric field at any boundary: for an *s* polarized \mathbf{E}^i , the electric field illuminating the partially AuNP only changes in amplitude on its boundary, even for $\theta_i > \theta_c$,

3. RESULTS AND DISCUSSION

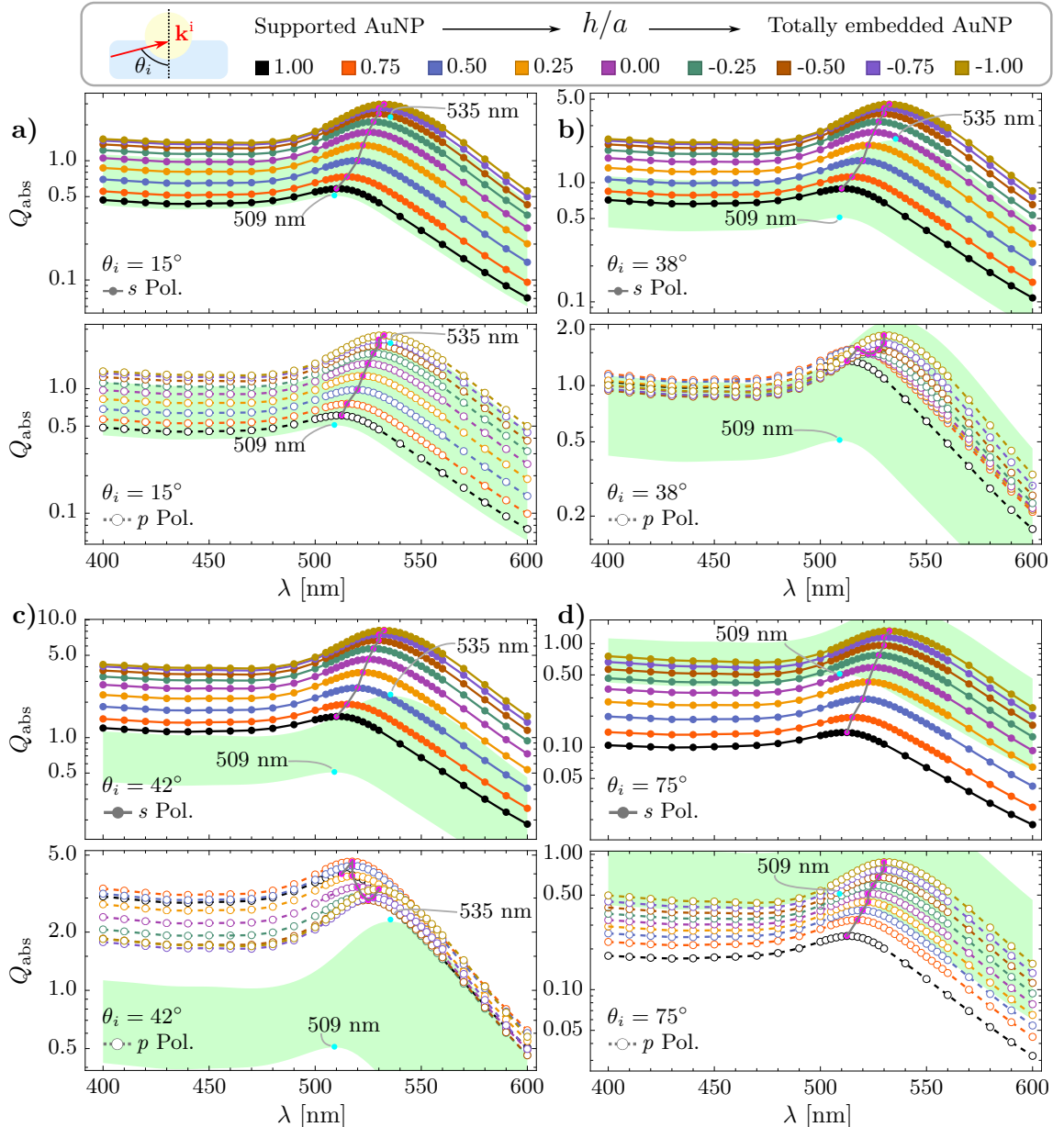


Fig. 3.13: Absorption efficiency of a 12.5 nm AuNP partially embedded in a glass substrate ($n_s = 1.5$) with an air matrix ($n_m = 1$), as a function of the wavelength λ of an s (filled circles/solid lines) and a p (empty circles/dashed lines) polarized incident electromagnetic plane wave propagating in the direction of the wave vector \mathbf{k}^i , in an internal configuration, at an angle of incidence θ_i of **a**) 15° , **b**) 38° , **c**) 42° , and **d**) 75° relative to the normal direction to the glass-air interface. The green shaded region shows the two Mie-limiting cases of a AuNP embedded either in air or in glass; the magenta (partially embedded AuNP) and cyan (Mie-limiting) markers correspond to the efficiencies evaluated at the wavelength of resonance for each case; the gray line is a guide to the eye.

yielding a smooth increase in the average optical properties (Q_{abs} and Q_{sca}) of the AuNP as its surroundings become optically denser.

Contrastingly, the efficiencies for the p polarization case (empty circles/dashed lines) are uniformly enhanced as h/a decreases —as in the s polarization case— only for the angles of

3.2 Partially Embedded Spherical Particle

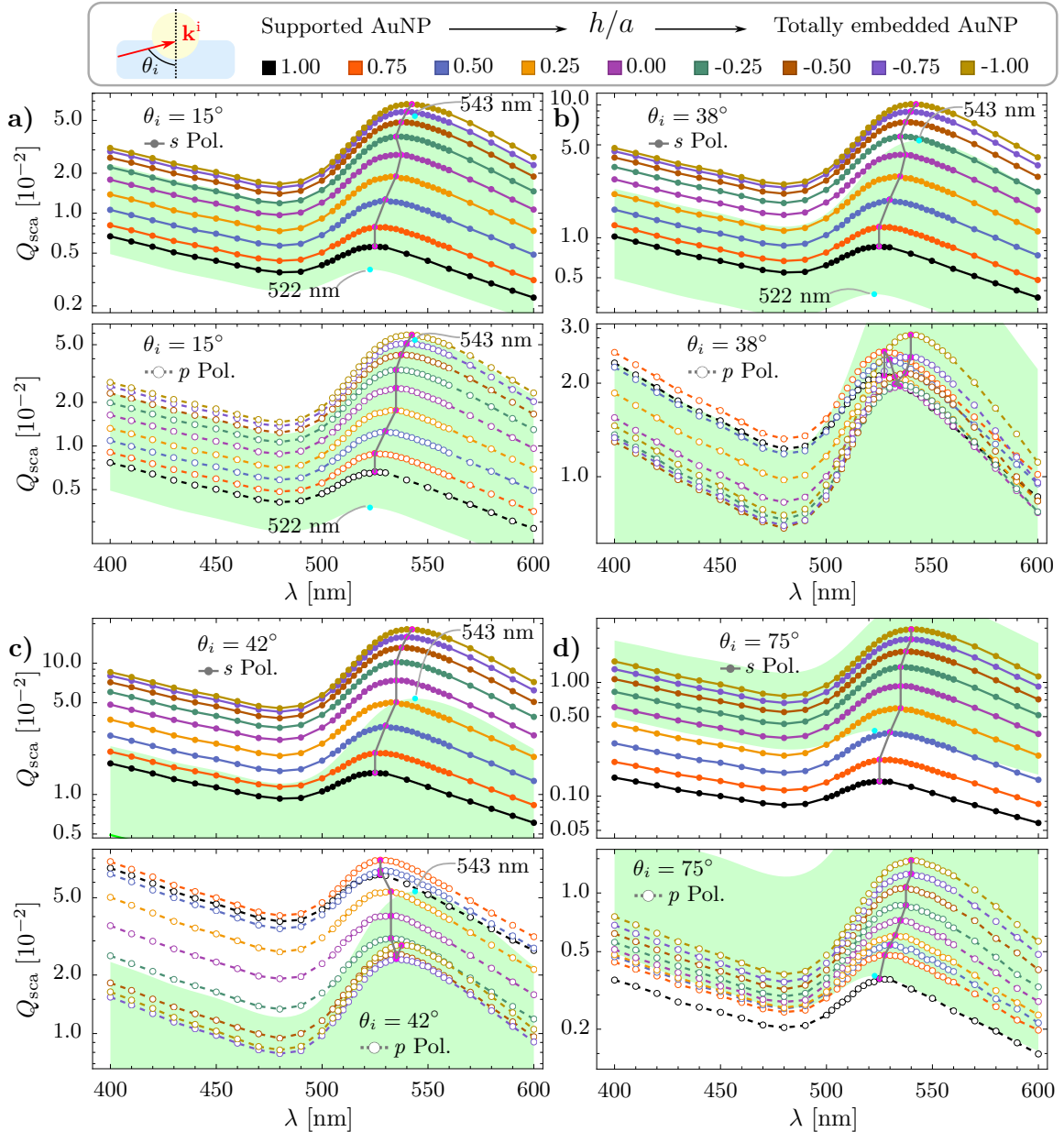


Fig. 3.14: Scattering efficiency of a 12.5 nm AuNP partially embedded in a glass substrate ($n_s = 1.5$) with an air matrix ($n_m = 1$), as a function of the wavelength λ of an s (filled circles/solid lines) and a p (empty circles/dashed lines) polarized incident electromagnetic plane wave propagating in the direction of the wave vector \mathbf{k}^i , in an internal configuration, at an angle of incidence θ_i of **a)** 15° , **b)** 38° , **c)** 42° , and **d)** 75° relative to the normal direction to the glass-air interface. The green shaded region shows the two Mie-limiting cases of a AuNP embedded either in air or in glass; the magenta (partially embedded AuNP) and cyan (Mie-limiting) markers correspond to the efficiencies evaluated at the wavelength of resonance for each case; the gray line is a guide to the eye.

incidence of 15° [Figs. 3.13a) and 3.14a)] and 75° [Figs. 3.13a) and 3.14a)], while for values of θ_i near $\theta_c = 41.8^\circ$, the dependency of the overall growth of Q_{abs} and Q_{sca} on h/a is as follows: the absorption efficiency for values of θ_i in the neighborhood of θ_c , such as for 38° and 42° [Figs. 3.13b) and 3.13c), respectively] present an uniform enhancement—for all λ —when $1 \leq h/a < 0.75$ and $0 < h/a \leq -1$ and an uniform diminishment as h/a changes from 0.75 (orange dashed

3. RESULTS AND DISCUSSION

curve) to 0.50 (blue dashed curve) and 0.25 (light orange dashed curve); a similar observation is made for the sactteringe efficiency for $\theta_i = 38^\circ$ and 42° [Figs. 3.14b) and 3.14c), respectively] where the diminishment of Q_{sca} occurs at a incrustation parameter of $0.50 \leq h/a \leq -0.50$ and the enhancement when h/a changes from 1 to 0.75 (black and orange dashed curves) and from -0.75 to -1 (light purple and brown dashed curves). Both of the aforementioned descriptions of the uniform enhancement and diminishment of Q_{abs} and Q_{sca} can be easily seen by following the gray lines joining their resonances as the incrustation parameters is changed. Attributing such behavior to the change of the electric field illuminating the AuNP above and below the glass-air interface, it can be seen that for a p polarized incident electric field, the scattering and absorption efficiencies of the partially embedded AuNP are similar to that of the supported (totally embedded) AuNP, due to the strength of the transmitted electric field, under determined values of the incrustation parameter: when $1 < h/a < 0.75$ ($-0.75 > h/a > -1$), that is, when one eight of the AuNP's volume/surface is embedded in the substrate (matrix).

The oblique illumination of a partially embedded AuNP of radius $a = 12.5$ nm with different values of the incrustation parameter h/a leads, besides to the uniform increase (decrease) of the absorption and scattering efficiencies discussed above, to a redshift of the absorption and scattering wavelengths of resonance, $\lambda_{\text{res}}^{\text{abs}}$ and $\lambda_{\text{res}}^{\text{sca}}$, which are shown in Table 3.1 —for all considered values of h/a , θ_i and both polarization sates— with aid of the saturation of the cell color, which is greater the larger the value of the resonance wavelength by case: $\lambda_{\text{res}}^{\text{abs}}$ and $\lambda_{\text{res}}^{\text{sca}}$ in either s or p polarization. From the reported values in Table 3.1, both the absorption and

Table 3.1: Wavelength of resonance for the absorption $\lambda_{\text{res}}^{\text{abs}}$ and the scattering $\lambda_{\text{res}}^{\text{sca}}$ efficiencies of a partially embedded 12.5 nm AuNP with a glass substrate ($n_s = 1.5$) and an air matrix ($n_m = 1$), illuminated by an s and a p polarized electromagnetic plane wave traveling to the glass-air interface at an incidence angle of 0° , 15° , 38° , 42° and 75° , for several values of the incrustation parameter h/a with h the distance between the AuNP and its radius a . The values in this table correspond to the magenta markers in Figs. 3.10, 3.13 and 3.14 while the saturation of the cell colors are a guide to the eye for the wavelength shift.

		$\lambda_{\text{res}}^{\text{abs}}$ [nm]					$\lambda_{\text{res}}^{\text{sca}}$ [nm]					
		h/a	0°	15°	38°	42°	75°	0°	15°	38°	42°	75°
s Polarization	1.00	510	510	510	510	512.5	525	525	525	525	525	525
	0.75	515	515	515	515	515	525	525	525	525	525	525
	0.50	520	520	520	520	520	530	530	530	530	530	530
	0.25	522.5	522.5	522.5	522.5	522.5	535	535	535	535	535	535
	0.00	525	525	525	525	525	537.5	537.5	537.5	535	535	535
	-0.25	527	527	527	527	527	535	535	535	535	535	535
	-0.50	530	530	530	530	530	537.5	537.5	537.5	537.5	537.5	537.5
	-0.75	530	530	530	530	530	540	540	540	540	540	540
	-1.00	532.5	532.5	532.5	532.5	532.5	542.5	542.5	542.5	542.5	540	540
p Polarization	1.00	510	512.5	512.5	512.5	512.5	525	525	527.5	527.5	525	525
	0.75	515	515	517.5	517.5	517.5	525	525	527.5	527.5	527.5	527.5
	0.50	520	520	517.5	517.5	520	530	530	530	527.5	530	530
	0.25	522.5	525.5	520	517.5	525.5	535	535	532.5	532.5	532.5	532.5
	0.00	525	525	522.5	520	522.5	537.5	535	535	535	535	535
	-0.25	527	527	525	522.5	525	535	535	532.5	535.5	537.5	537.5
	-0.5	530	530	527	525	527	537.5	537.5	537.5	535	537.5	537.5
	-0.75	530	530	530	527	530	540	540	540	535	540	540
	-1.00	532.5	532.5	530	530	530	542.5	542.5	540	537.5	540	540

scattering resonances are spectrally located in between the resonances for the Mie-limiting results (cyan markers in Figs. 3.13 and 3.14) and that resonances for the partially embedded AuNP are, in general, redshifted as the embedding of the AuNP increases (h/a changes from 1 to -1). In particular, the redshift of $\lambda_{\text{res}}^{\text{abs}}$ (gray cells) and $\lambda_{\text{res}}^{\text{sca}}$ (orange cells) for an s polarized incident electric field (upper block in Table 3.1) is independent of the angle of incidence and the rate of change of the redshift in relation to the incrustation parameter is a uniform function. The observed rate of change of the redshift for the p polarization case (lower block in Table 3.1) as the incrustation parameter decreases, has a similar behavior for the absorption and scattering resonances just as the one observed for the s polarization case nevertheless, this rate for the p polarized illumination of the AuNP is different for each incident angle unlike its counterpart. On the one hand, for values of θ_i far from θ_c the dependence of $\lambda_{\text{res}}^{\text{abs}}$ and $\lambda_{\text{res}}^{\text{sca}}$ on h/a for p polarization resembles that for s polarization, as it can be seen not only in the color gradient in Table 3.1 but also in the comparison between the gray continuous lines in Figs. 3.13a) and 3.14a) for $\theta_i = 15^\circ$ and in Figs. 3.13d) and 3.14d) for $\theta_i = 75^\circ$. On the other hand, for θ_i in the neighborhood of θ_c , the rate of the redshift as the AuNP is buried into the substrate is larger for values of $h/a < 0$ than for $h/a > 0$ and, additionally, this change in the rate is more notorious for $\theta_i = 42^\circ \gtrsim \theta_c$ than for $38^\circ \lesssim \theta_c$. The redshift for both s and p polarizations can be explained by the directions of electric field below and above the glass-substrate interface. For s polarization the electric field is parallel to the interface and due to its continuity across boundaries there is no change in its direction for any θ_i , thus the uniform redshift arises. For p polarization, there are both parallel and perpendicular components of the electric field relative to the glass-air interface; the perpendicular component of the electric field in the substrate is antiparallel to that in the matrix, and thus there is a competition among the perpendicular components of the electric field when it is integrated at the surface of the AuNP (to calculate Q_{sca}) and in its volume (to calculate Q_{abs}) when h/a is around zero, that is, when there is no major part of the AuNP in one medium.

Both the uniform enhancement of Q_{abs} and Q_{sca} and the redshift of their resonance wavelength are expected to behave similarly, for a fixed angle of incidence and polarization, since the absorption and scattering efficiencies are quantities calculated by a volume and a surface integral given by Eqs. (1.9) and (1.8), respectively, and since both the volume and surface fraction of the AuNP in the substrate, relative to its total volume or surface, are given by the same expression $(1 - h/a)/2$. The uniform changes on Q_{abs} and Q_{sca} and their resonance wavelength for the s polarization case as the AuNP is buried suggest that the average optical properties of the partially embedded AuNP are determined, for the s polarization case, solely by the fraction of the AuNP embedded in either medium between the substrate and the matrix, while for p polarization the direction and magnitude of the transmitted electric field are to be taken into account if more (less) than one eighth of the AuNP is in the substrate, leading to a rapid (slow) change of its average optical properties as h/a changes. The past summary of the discussion on Figs. 3.13 and 3.14, and Table 3.1 describes the average optical properties of a partially embedded 12.5 nm AuNP given by Q_{abs} and Q_{sca} ; to have a better understanding of all the optical properties of such system, the spatial distribution of the induced electric field, in the far and near-field regimes, is to be analyzed.

The radiation patterns of a partially embedded 12.5 nm AuNP shown in Fig. 3.15 consider that the AuNP is illuminated at an angle of incidence—above the critical angle—of 42° [Figs. 3.15a) and 3.15b)] and of 75° [Figs. 3.15c) and 3.15d)] by an s polarized incident electric field

3. RESULTS AND DISCUSSION

with a wavelength $\lambda = 525$ nm, the resonance wavelength for the incrustation parameter $h/a = 0$; in Figs. 3.15a) and 3.15c) the radiation patterns are evaluated at a scattering plane perpendicular to the plane of incidence (vertical gray dotted line), while it overlaps to it in Figs. 3.15b) and 3.15d). The radiation patterns for $\theta_i < \theta_c$ were omitted since they follow the same tendency as the one presented in Fig. 3.11 due to the incident electric field being parallel to the interface between the substrate and the matrix.

What is observed in Fig. 3.15 is that the radiation patterns for different values of the incrustation parameters h/a , at fixed angle of incidence and s polarization, present the two and one-lobe shapes with an asymmetry due to the substrate, as discussed in the Section 3.2.1 for a normally illuminated AuNP. As mentioned, the average amplitude of the radiation pattern for oblique incidence is larger the more embedded into the substrate the AuNP is, for example, as h/a changes from 0.75 (orange curves) to -0.75 (light purple curves). Additionally, the radiation pattern is modulated by the magnitude of the efficiencies, thus it is expected that the scattered far-field has a shorter extent for an angle of incidence farther from θ_c , that is the case when Figs. 3.15a) and 3.15b) ($\theta_i = 42^\circ$) are compared with Figs. 3.15c) and 3.15d) ($\theta_i = 75^\circ$). These results are in agreement with the discussion on the optical properties of a partially embedded AuNP illuminated with an s polarization incident electric field: their properties change uniformly with the incrustation parameter including the far-field distribution as well as the absorption and scattering efficiencies, due to the direction of the transmitted electric field not changing above and below the glass-air interface.

For a p polarized incident electric field \mathbf{E}^i , the reflected and transmitted electric fields have a direction dependent on the angle of incidence θ_i , therefore the radiation patterns of a partially embedded 12.5 AuNP is expected to behave differently for each θ_i . The radiation patterns for the described system, considering a wavelength $\lambda = 525$ nm for \mathbf{E}^i , are shown in Figs. 3.16 and 3.17 for values of θ_i below and above the critical angle 41.8° , respectively. The radiation patterns in Figs. 3.16a) and 3.16b) correspond to $\theta_i = 15^\circ$ and in Figs. 3.16c) and 3.16d) to $\theta_i = 38^\circ$, while the radiation patterns for $\theta_i = 42^\circ$ are shown in Figs. 3.17a) and 3.17b), and for $\theta_i = 75^\circ$ in Figs. 3.17c) and 3.17d). In both Fig. 3.16 and Fig. 3.17, the radiation patterns are evaluated at a) a scattering plane perpendicular to the incidence plane (vertical gray dotted line) and at b,d) a scattering plane overlapping the incidence plane.

The radiation patterns for a partially embedded AuNP when it is illuminated at $\theta_i < \theta_c = 41.8^\circ$ [Fig. 3.16], so that the transmitted electromagnetic field is a plane wave, resembles that of a supported AuNP —discussed in Section 3.1.2—: an asymmetrical one-lobe shape and a two-lobe shape characteristic of a point dipole oriented perpendicularly to the propagating direction of the transmitted electromagnetic field. One effect of the AuNP's embedding is the enhancement of the average amplitude of the radiation patterns according to the absorption and scattering efficiencies, as already discussed for the s polarization case shown in Fig. 3.15 and also observed for p polarization at $\theta_i = 15^\circ$ in Figs. 3.16a) and 3.16b) nevertheless, a deformation of the radiation patterns as the AuNP is buried into the substrate can be observed, particularly for $\theta_i = 38^\circ$ in Figs. 3.16c) and 3.16d). In the first, the one-lobe shape for $h/a \leq 0$ is deformed into a two lobe-shape if $h/a > 0$, and in the later there is a rotation of $\sim 10^\circ$ clockwise of the two-lobe radiation pattern for $h/a > 0$ relative to the patterns for $h/a \leq 0$, which are aligned around the direction of the transmitted electric field.

Another difference that arises between the radiation patterns of a partially embedded

3.2 Partially Embedded Spherical Particle

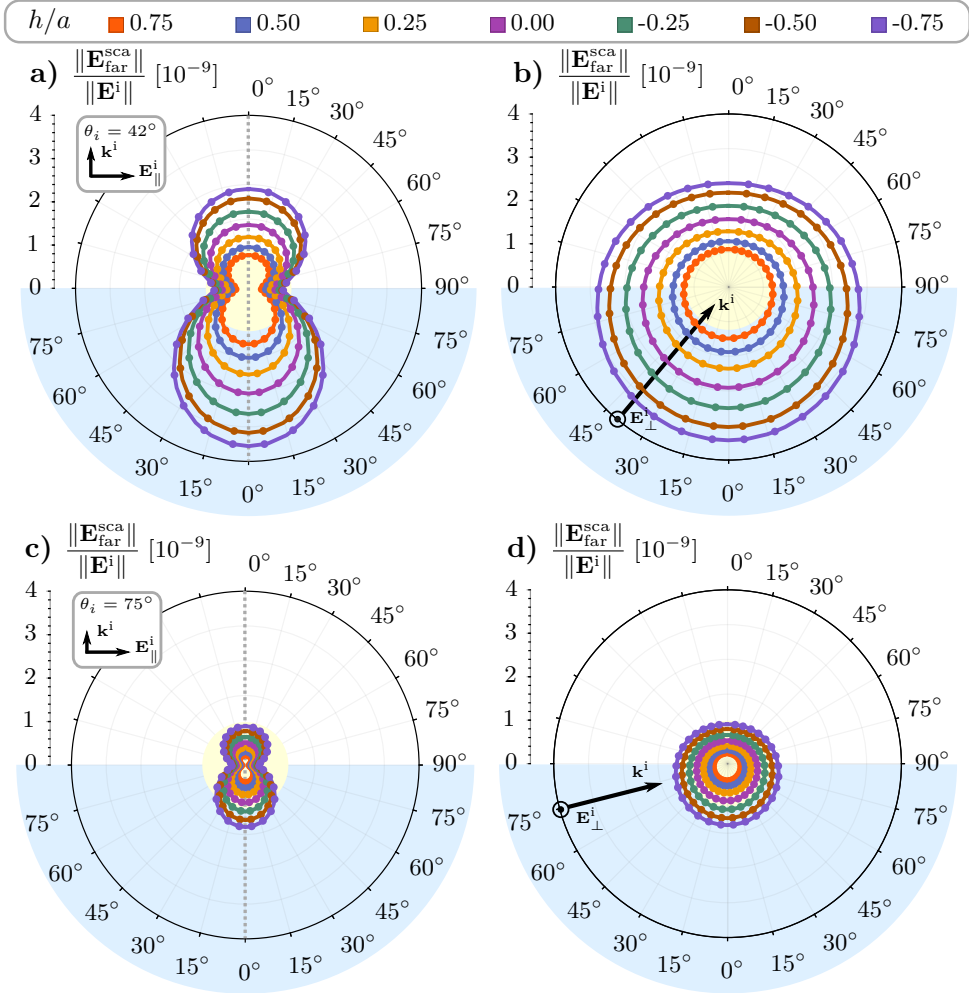


Fig. 3.15: Radiation patterns of a AuNP (light yellow) of radius $a = 12.5$ nm partially embedded in a glass substrate (light blue, $n_s = 1.5$) with an air matrix ($n_m = 1$), illuminated by an s polarized incident electromagnetic plane wave \mathbf{E}^i , with a wavelength $\lambda_{\text{abs}}^{\text{res}}$ (see Table 3.1) and traveling in the \mathbf{k}^i direction at an angle of incidence θ_i of **a,b**) 42° and **c,d**) 75° relative to the normal direction to the glass-air interface. The radiation patterns consider various values of the incrustation parameter h/a , with a the AuNP's radius and h the distance between its center and the interface, and an incident electric field **a,c**) perpendicular to the incidence plane (vertical gray dotted lines) and **b,d**) equal to the incidence plane. In all cases, the incident wave vector \mathbf{k}^i , the perpendicular \mathbf{E}_{\perp}^i and the parallel \mathbf{E}_{\parallel}^i projections of the incident electric field relative to the scattering plane are schematized.

AuNP and a supported AuNP (Section 3.1.2) when illuminated at an oblique incidence, is that the amplitude of the radiation patterns, at is maximum, is different depending on the polarization state of the incident electric field. While the radiation patterns for supported AuNPs show a greater magnitude for p polarization than for s polarization —see Fig. 3.7— when $\theta_i \gtrsim \theta_c$, the contrary is observed for the partially embedded AuNP, as it can be verified by comparing the axis scales in Figs. 3.15 (up to 4 for s polarization) and 3.17 (up to 2.5 for p polarization). Such difference in magnitude of the radiation patterns may arise due to the anisotropy of the electric field for each polarization; particularly the influence of the transmitted electric field described by an evanescent wave, whose effect is easily identified even for slightly embedded

3. RESULTS AND DISCUSSION

AuNPs— $0.75 \leq |h/a|$ —at $\theta_i = 42^\circ$ where the radiation patterns correspond to that of an electric point dipole perpendicular to the glass-substrate interface—see the two-lobe shapes aligned along the interface in Figs. 3.17a) and 3.17b)—. Lastly, the radiation patterns observed for $\theta_i = 75^\circ$ in Figs. 3.17c) and 3.17d) show, respectively, a less defined two-lobe shape aligned to the substrate and an asymmetrical shape that deforms from a one to a two-lobe shape perpendicular to the interface as h/a decreases. Both of these effects are the result of the contribution of the electric field below the substrate overcoming the contribution of the transmitted field since the penetration depth of the evanescent wave decreases for larger angles of incidence, as well as the embedding decreases the coupling of the evanescent wave and the AuNP.

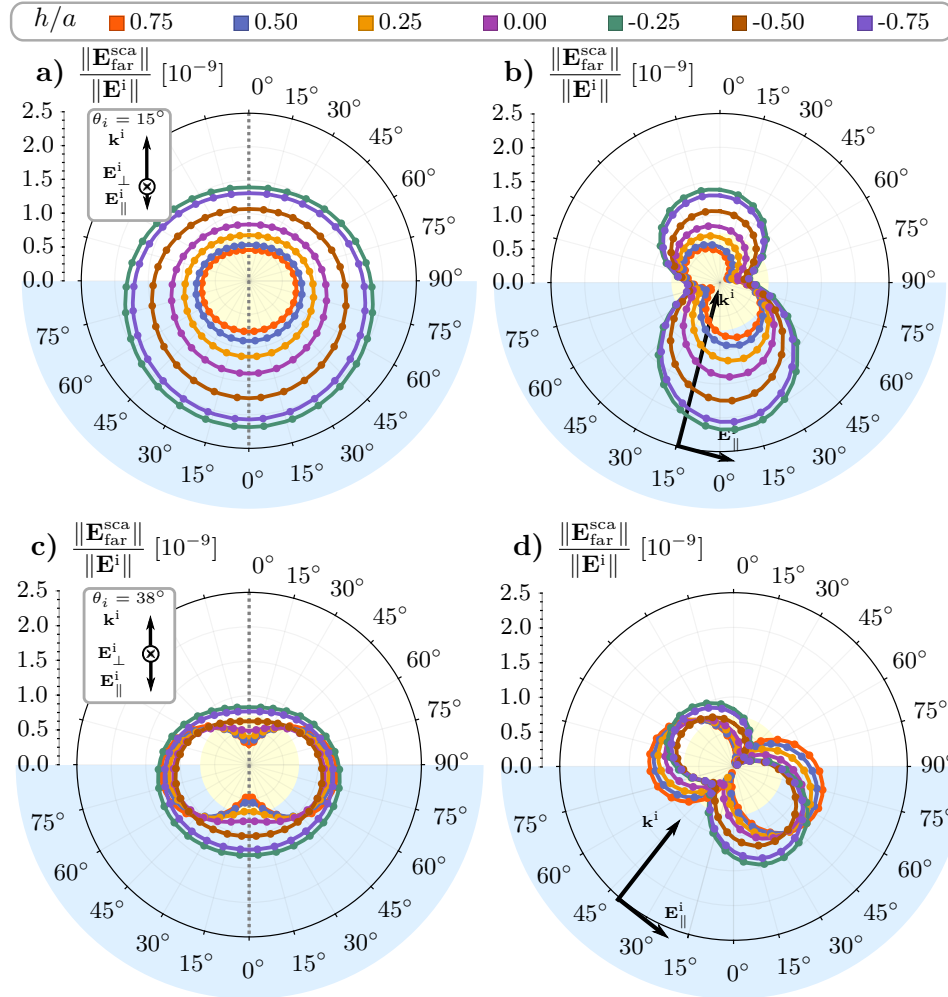


Fig. 3.16: Radiation patterns of a AuNP (light yellow) of radius $a = 12.5$ nm partially embedded in a glass substrate (light blue, $n_s = 1.5$) with an air matrix ($n_m = 1$), illuminated by an p polarized incident electromagnetic plane wave \mathbf{E}^i , with a wavelength $\lambda_{\text{abs}}^{\text{res}}$ (see Table 3.1) and traveling in the \mathbf{k}^i direction at an angle of incidence θ_i of a,b) 15° and c,d) 38° relative to the normal direction to the glass-air interface. The radiation patterns consider various values of the incrustation parameter h/a , with a the AuNP's radius and h the distance between its center and the interface, and an incident electric field a,c) perpendicular to the incidence plane (vertical gray dotted lines) and b,d) equal to the incidence plane. In all cases, the incident wave vector \mathbf{k}^i , the perpendicular \mathbf{E}_\perp^i and the parallel \mathbf{E}_\parallel^i projections of the incident electric field relative to the scattering plane are schematized.

3.2 Partially Embedded Spherical Particle

The analysis of the scattered electric field in the far-field regime, was in agreement with the discussion of the absorption and scattering efficiencies in that the optical properties of a partially embedded AuNP changes uniformly as the NP is buried into the substrate when it is illuminated by an s polarized electric field, while these changes are also dependent on the angle of incidence for a p polarization, yielding a more sensitive optical response for an incidence at an angle above and near the critical angle. When the system is illuminated by a p polarized electromagnetic field, it was noted that, in general, the average optical properties of the system (Q_{abs} and Q_{sca}) are closer to that of the Mie-limiting case of the AuNP in the substrate (matrix) if more (less) than one eighth of the AuNP is in such medium. On the other hand, the radiation patterns for

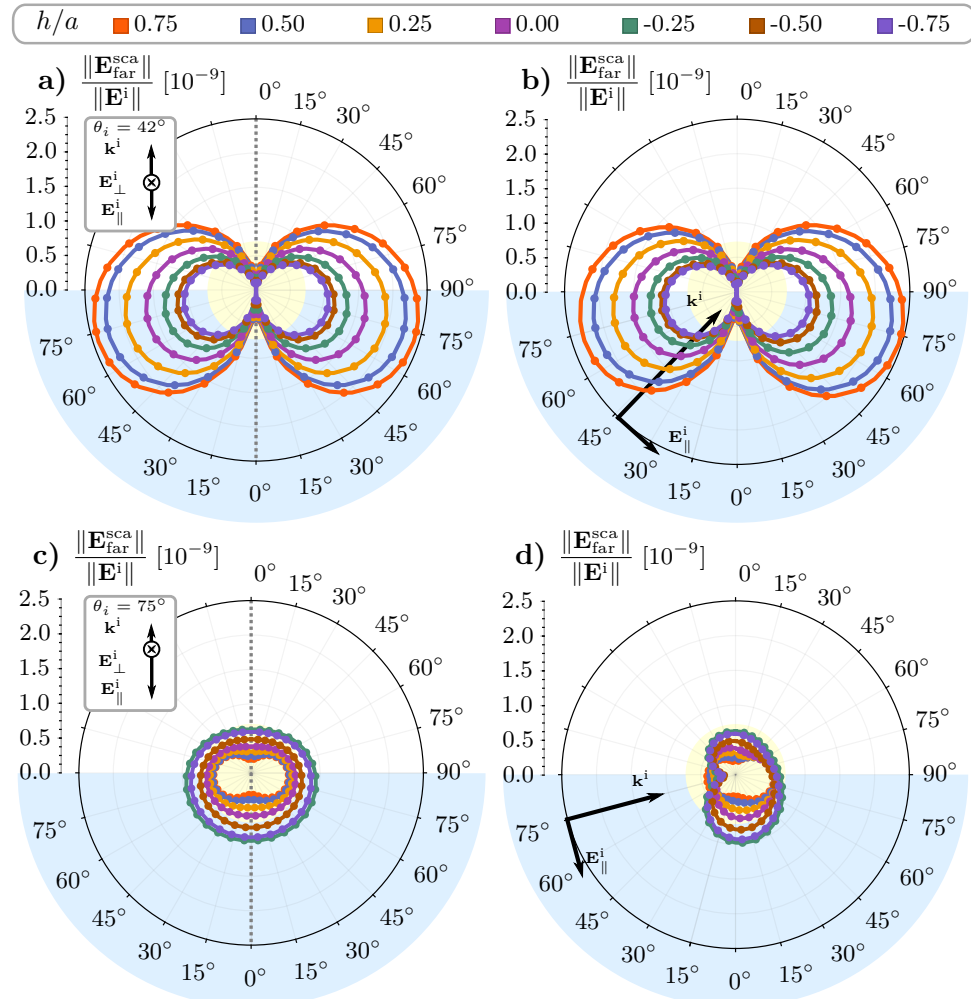


Fig. 3.17: Radiation patterns of a AuNP (light yellow) of radius $a = 12.5$ nm partially embedded in a glass substrate (light blue, $n_s = 1.5$) with an air matrix ($n_m = 1$), illuminated by an p polarized incident electromagnetic plane wave \mathbf{E}^i , with a wavelength $\lambda_{\text{abs}}^{\text{res}}$ (see Table 3.1) and traveling in the \mathbf{k}^i direction at an angle of incidence θ_i of **a,b**) 42° and **c,d**) 75° relative to the normal direction to the glass-air interface. The radiation patterns consider various values of the incrustation parameter h/a , with a the AuNP's radius and h the distance between its center and the interface, and an incident electric field **a,c**) perpendicular to the incidence plane (vertical gray dotted lines) and **b,d**) equal to the incidence plane. In all cases, the incident wave vector \mathbf{k}^i , the perpendicular \mathbf{E}_{\perp}^i and the parallel \mathbf{E}_{\parallel}^i projections of the incident electric field relative to the scattering plane are schematized.

3. RESULTS AND DISCUSSION

the p polarized illumination of a partially embedded AuNP are uniformly transformed (only in shape) as the incrustation of the AuNP changes for all angles of incidence, except values of θ_i near and above the critical angle where the contribution to the optical properties in the spatial distribution of the induced electric field are dominated by the evanescent wave. To observe such distribution, and evaluate if there is a configuration of the system of interest suited for biosensing, the induced electric field is analyzed in the near-field regime.

In Fig. 3.18 the spatial distribution of the induced electric field is shown for a partially embedded 12.5 nm AuNP when it is illuminated at an angle of incidence of $\theta_i = 42^\circ > \theta_c$, in an internal configuration and an incrustation parameter $h/a = 0$, by an s [Figs. 3.18a) and 3.18b)] and a p [Figs. 3.18c) and 3.18d)] polarized incident electric field \mathbf{E}^i with a wavelength of $\lambda = 525$ nm; additionally, the near-field distribution of a partially embedded AuNP considering an incrustation parameter $h/a = -0.75$ is shown only for the p polarized incident electric field with $\lambda = 525$ nm in Figs. 3.18e), 3.18f). The magnitude of \mathbf{E}^{ind} is shown for a scattering plane parallel to the incident electric field [Figs. 3.18a), 3.18c), and 3.18e)] and perpendicular to it [Figs. 3.18b), 3.18d), and 3.18f)].

The choice of the values of θ_i , h/a and polarization for the distribution of the induced electric field shown in Fig. 3.18 exemplifies the general trends found in the optical properties in the far-field of the partially embedded AuNP. For the s polarized \mathbf{E}^i traveling at $\theta_i = 42^\circ$, it is observed that the stronger enhancement of the near field is localized on the surface of the AuNP inside the substrate and that the hotspots are aligned parallel to the substrate and perpendicular to the incidence plane [Fig. 3.18a)], such as when the AuNP was normally illuminated in Section 3.2.1. Nevertheless, the strength of the induced electric field on the overall AuNP's surface is ~ 4 times stronger than the incident electric field due to the effect of the transmitted evanescent wave. For the case with $\theta_i = 42^\circ$ and considering p polarization for \mathbf{E}^i , the hotspots of the induced electric field are located perpendicularly to the glass-air interface for both $h/a = 0$ [Figs. 3.18c) and 3.18d)] and $h/a = -0.75$ [Figs. 3.18e) and 3.18f)], and the spatial distribution of the induced electric field presents a cylindrical symmetry for both incrustation parameters, meaning that even if the average optical properties of the partially embedded AuNP, with $h/a = -0.75$, are dominated by their response in the substrate—as discussed above—the spatial distribution in the near-field is dominated by the evanescent wave, as it can be seen in Figs. 3.18c), 3.18d), 3.18e) and 3.18f), since the largest enhancement of the electric field is located on the AuNP's surface above the substrate.

In this Chapter, the optical properties of a AuNP of radius $a = 12.5$ nm in the presence of an homogeneous surrounding consisting of a glass substrate and an air matrix were calculated numerically by means of the Finite Element Method. The obtained results were compared with the Mie-limiting cases, which correspond to the analytical solution of the light absorption and scattering of a single spherical particle in a homogeneous medium due to its interaction with an electromagnetic plane wave. The presence of the substrate allows for different illumination schemes based on the polarization of the incident electric field and on the side from which the system is illuminated, as well as an additional degree of freedom: the embedding of the AuNP in the substrate. From the obtained results, it was concluded that a 12.5 nm AuNP can be studied in the small particle approximation even if it is partially embedded and illuminated by an evanescent wave, rather than with a plane wave, in the case of total internal reflection. Additionally, it was observed that the Localized Surface Plasmon Resonance (LSPR) of the

3.2 Partially Embedded Spherical Particle

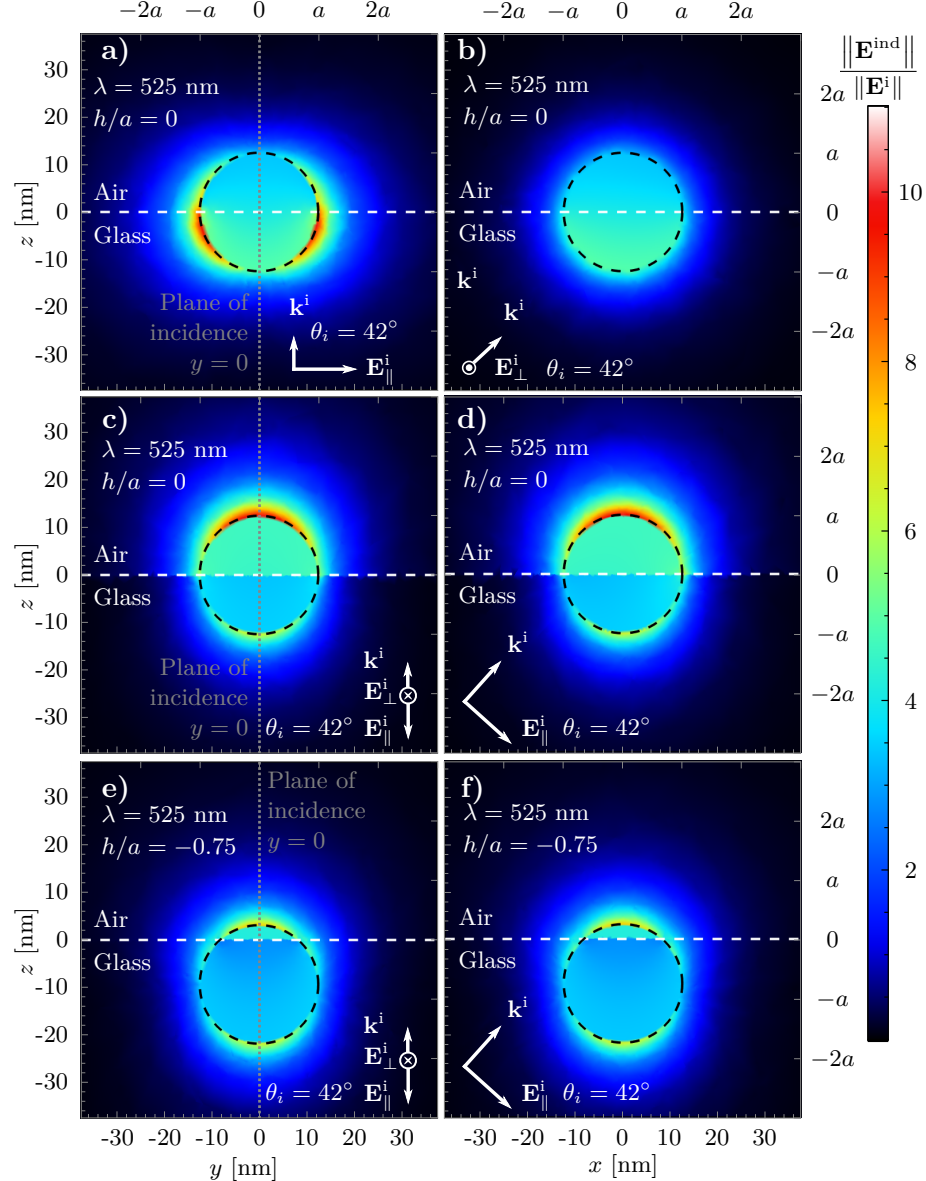


Fig. 3.18: Magnitude of the electric field \mathbf{E}^{ind} induced by a partially embedded 12.5 nm AuNP (dashed black lines) illuminated by an incident electromagnetic plane wave \mathbf{E}^i traveling in the \mathbf{k}^i direction, in an internal configuration, at an angle of incidence of 42° relative to the normal direction to the interface—white dashed lines—between an air matrix ($n_m = 1$) and a glass substrate ($n_s = 1.5$), considering **a,b**) *s* polarization of \mathbf{E}^i and an incrustation parameter $h/a = 0$, **c,d**) *p* polarization and $h/a = 0$, and **e,f**) *p* polarization and $h/a = -0.75$. The incident electromagnetic plane wave is evaluated at $\lambda = 525$ nm and $\|\mathbf{E}^{\text{ind}}\|$ is evaluated at **a,c,e**) a scattering plane perpendicular to the incidence plane (vertical gray dotted lines) and at **b,d,f**) a scattering plane overlapping the incidence plane.

partially embedded 12.5 nm AuNP particle is spectrally localized in between the LSPR of the two Mie-limiting cases but that the values of the absorption and scattering efficiencies can be larger than for the Mie-limiting cases, specifically for angles of incidence in the neighborhood of the critical angle. Such changes, for an *s* polarized illumination of the system were found to

3. RESULTS AND DISCUSSION

be uniform relative to the incrustation parameter —introduced in Section 3.2— while for a p polarized illumination the change of direction of the transmitted electric above the substrate yield an optical response dependent on both the angle of incidence and on the incrustation parameter. In particular, the spatial distribution of the near-field is strongly determined by the evanescent wave for a p polarized illuminated system, which forced the greater enhancement of the electric field to be on the AuNP’s surface in contact with the substrate. In summary, the presence of a substrate enhances the optical properties of a 12.5 nm AuNP when illuminated by an evanescent wave. Depending on the polarization of the incident electromagnetic field, the enhancement of the induced electric field can be localized in the matrix side, rather than in the substrate, even when the AuNP is partially embedded in between both media.

In this thesis the optical properties of a partially embedded AuNP were calculated by the FEM and characteristics such as tuning of the LSPR and control over the spatial distribution of the electric field were identified. Due to these characteristics, which can be exploited alongside the intrinsic feature of non-washability of partial embedding, bidimensional arrays of partially embedded AuNPs are suited for biosensing. Lastly, the methodology developed in this thesis can be employed for nanospheres of different materials than Au, and different matrices and substrates considering a relatively small spectral window in between the Mie-limiting cases of the system of interest.

Conclusions

In this thesis, the optical properties of a spherical gold nanoparticle (AuNP) of radius $a = 12.5$ nm, partially embedded in an air matrix and in a glass substrate, was studied as a function of its embedding degree, characterized by the incrustation parameter h/a —with h the position of the center of the AuNP relative to the planar air-glass interface—. By means of the Finite Element Method —implemented in the commercial software COMSOL Multiphysics™ Ver. 5.4— the absorption and scattering efficiencies, the radiation pattern and the spatial distribution of the induced electric field of the partially embedded 12.5 nm AuNP were calculated when the AuNP was illuminated by an electromagnetic plane wave traveling at an oblique direction, with a defined polarization state; all numerical results were compared with the Mie-limiting cases calculated analytically, consisting in a 12.5 nm AuNP embedded in an infinite matrix of air, and an infinite matrix of glass. From the preformed calculations, it was observed that the 12.5 nm AuNP with partial embedding can be described by a mainly dipolar contribution, that its coupling with the incident light and the spatial distribution of the electric field enhancement on its surface can be tuned depending on the embedding of the AuNP and its illumination conditions, and that the optical response is maximized if the system is illuminated with an evanescent wave at an angle of incidence near the critical angle. More specifically, from the preformed calculations the following can be concluded:

- **The optical response of a single partially embedded AuNP can be described by a mainly dipolar contribution.**

The absorption and scattering efficiencies present only one global maximum in the visible spectrum, at which the spatial distribution of the electric field enhancement and its radiation pattern resemble that of an electric point dipole. This behavior can be extended to other materials of the matrix, the substrate and the nanosphere (of any size) as long as the scattering contribution to the extinction of light is small compared to the absorption contribution.

- **There is a smooth transition between the two Mie-limiting cases as the nanosphere is partially embedded into the substrate.**

The wavelength of resonance of the absorption and scattering efficiencies of the partially embedded nanosphere is localized in between the two Mie-limiting cases, which consist in the nanosphere embedded in an infinite media (either the matrix or the substrate). Additionally, the wavelength of resonance is redshifted from the resonance wavelength of the matrix Mie-limiting case to the resonance wavelength of the substrate Mie-limiting case, and this redshift is different for an s or for a p polarized incident electric field.

3. RESULTS AND DISCUSSION

- The optical response of the nanosphere resembles that of a supported (totally embedded) nanosphere if at most one eighth of its volume is partially embedded in the substrate (matrix).

The supported and totally embedded nanosphere are the extreme cases of the partially embedded nanosphere when the sphere is tangential to the matrix-substrate interface. The absorption and scattering efficiencies of the partially embedded nanospheres, for both polarizations, are enhanced and redshifted in the same trend as the supported and totally embedded spheres as the angle of incidence of the incident light changes if at most one eighth of the nanosphere crossed the interface.

- The optical properties of the partially embedded nanospheres are maximized if illuminated at an angle of incidence near the critical angle.

For any incrustation parameter and polarization state, the magnitude of the scattering and absorption efficiencies is enhanced—for all wavelengths in the visible spectrum—as the angle of incidence grows from zero to the critical angle, and they start to diminish for angles of incidence above the critical angle. This behavior is due to the effect of an evanescent wave illuminating the system above the interface, whose penetration depth is maximum at the critical angle.

- The wavelength of resonance and the electric field spatial distribution of the partially embedded nanospheres for *s* polarized illumination do not depend on the angle of incidence while they do for *p* polarized illumination.

On the one hand, for *s* polarization, the redshift of the resonance wavelength as the nanosphere is buried into the substrate, is the same for all angles of incidence and the electric field at the resonance wavelength is enhanced in two hotspots aligned parallel to the interface and on the surface of the nanosphere in the substrate side of the system. On the other hand, for *p* polarization, the redshift of the resonance wavelength is different for each angle of incidence. For example, near the critical angle, the redshift is appreciable if more than half of the nanosphere is buried into the substrate, while for normal incidence the behavior is equivalent to the *s* polarization case. On the spatial distribution, one hotspot is located in the matrix and other in the substrate, and their alignment is determined by the transmitted electric field; in particular, for angles above the critical angle, the hotspots are aligned perpendicular to the substrate.

Finally, it can be concluded that the optical properties of a partially embedded spherical AuNP of radius 12.5 nm, with at most one eighth of its volume buried into the substrate, is suited for interactions with elements in the matrix under internal illumination. If the system is illuminated with a *p* polarized incident electromagnetic plane wave traveling at an angle $\theta_i \gtrsim \theta_c$, the system is optimized to interact with its surroundings above the substrate since the optical response is maximized in the matrix. Therefore, partially embedded spherical AuNPs are strong candidates for meta-atoms conforming a disordered biosensing-aimed-metasurface.

Future Work: Application on Metasurfaces

Based on numerical calculations performed with the Finite Element Method, in this thesis it was determined the conditions at which a single spherical AuNP of radius 12.5 nm partially

embedded in an air matrix and glass substrate is able to interact with its surrounding above the substrate and at which its optical response is maximized. This feature does not only suit the 12.5 nm AuNP as a candidate for the meta-atoms conforming a disordered metasurface tailored for biosensing, but also give rise to methodologies to theoretically study the optical properties of such bidimensional systems and to experimentally determine its average incrustation degree. The proposal for these methodologies are the following:

- **Theoretical description of the optical behavior of disordered metasurfaces of partially embedded AuNPs**

To include the partial embedding of the nanosphere in theoretical models that describe the optical properties of bidimensional arrays of small particles supported on a substrate, like the Thin Island Theory [13] or the Dipolar Model [14] which are Effective Medium Theories (EMTs), it is proposed to modify a homogenization theory for the medium surrounding the nanosphere —like the Bruggeman or power law formulas [15]—, so that the resonance of a single nanosphere is excited at the same wavelength than that of the partially embedded nanosphere, for a fixed angle, polarization and incrustation degree. Once a homogenization theory for the surroundings of the partially embedded nanosphere is developed, an EMT can be used considering that the nanospheres are perfectly supported on a substrate and embedded in the homogenized medium, then the optical response of the real system can be described with a stratified system of three layers: substrate-homogenized EMT-matrix. It is expected that this approach can describe the optical properties of biosensing-aimed-metasurfaces with the embedding feature that can allow them to be used long-lastingly under realistic conditions.

- **Methodology to measure the average incrustation degree of a disordered metasurfaces of partially embedded AuNPs**

To determine the average incrustation degree of bidimensional arrays of identical spherical nanospheres (small compared with the wavelength of the incident light), it can be performed reflectivity measurements with p polarized white light in Kretschmann configuration for different angles of incidence. By following the redshift of the resonance wavelength as a function of the angle of incidence it can be determined the average incrustation parameter by comparing the experimental data with theoretical calculations, as those presented in Fig. 3.1.

Appendix A

Mie Theory (Conventions)

The Vector Spherical Harmonics (VSH) were defined in Section 1.2.1 in terms of their generating function $\psi(r, \theta, \varphi)$ which must satisfy the scalar Helmholtz equation [Eq. (1.15)]. By employing the separation of variables method, it was determined that ψ is the product of either $\sin(m\varphi)$ or $\cos(m\varphi)$, the associated Legendre functions $P_\ell^m(\cos \theta)$ and the spherical Bessel/Hankel functions $z_\ell(kr)$, which are solutions to Eqs. (1.16)-(1.20). In this Section, it is discussed the chosen definitions for P_ℓ^m , z_ℓ and related functions, as well as how to calculate them.

Radial Dependency: Spherical Bessel/Hankel Functions

The radial dependency of the VSH is given by the two linearly independent solutions to Eq. (1.20) which are the spherical Bessel function of first and second kind $j_\ell(\rho)$ and $y_\ell(\rho)$, respectively, related to the regular Bessel function of fractional order $J_{\ell+1/2}(\rho)$ and $Y_{\ell+1/2}(\rho)$ by [55]

$$j_\ell(\rho) = \sqrt{\frac{\pi}{2\rho}} J_{\ell+1/2}(\rho), \quad \text{and} \quad y_\ell(\rho) = \sqrt{\frac{\pi}{2\rho}} Y_{\ell+1/2}(\rho). \quad (\text{A.1})$$

Another set of two linear independent solutions to Eq. (1.20) are the spherical Hankel functions of first ($h_\ell^{(1)}$) and second kind ($h_\ell^{(2)}$) given by [55]

$$h_\ell^{(1)}(\rho) = j_\ell(\rho) + iy_\ell(\rho), \quad \text{and} \quad h_\ell^{(2)}(\rho) = j_\ell(\rho) - iy_\ell(\rho). \quad (\text{A.2})$$

Since the spherical Hankel functions are a linear combination of the Bessel spherical functions, they four obey the following recurrence relations [55]

$$\frac{z_\ell(\rho)}{\rho} = \frac{z_{\ell-1}(\rho) + z_{\ell+1}(\rho)}{2\ell + 1}, \quad (\text{A.3})$$

$$\frac{dz_\ell(\rho)}{d\rho} = \frac{\ell z_{\ell-1}(\rho) - (\ell + 1)z_{\ell+1}(\rho)}{2\ell + 1}, \quad (\text{A.4})$$

with z_ℓ any of the functions in Eqs. (A.1) and (A.2).

Azimuthal Angular Dependency φ : Sine, Cosine

Within this text, it was chosen the azimuthal solution to the scalar Helmholtz equation to be sines and cosines, so m can only take non negative integer values. These functions obey the orthogonality relations

$$\int_0^{2\pi} \sin(m\varphi) \sin(m'\varphi) d\varphi = \delta_{m,m'}(1 - \delta_{0,m})\pi, \quad (\text{A.5})$$

$$\int_0^{2\pi} \cos(m\varphi) \cos(m'\varphi) d\varphi = \delta_{m,m'}(1 + \delta_{0,m})\pi, \quad (\text{A.6})$$

$$\int_0^{2\pi} \cos(m\varphi) \sin(m'\varphi) d\varphi = 0, \quad (\text{A.7})$$

with $\delta_{m,m'}$ the Kronecker delta.

Polar Angular Dependence: Associated Legendre Functions and the Angular Functions π_ℓ and τ_ℓ

The solution to the polar angle equation [Eq. (1.17)] are the associated Legendre functions and in this work they are defined as by Arfken and Weber [47], that is,

$$P_\ell^m(\mu) = (1 - \mu^2)^{m/2} \frac{d^m}{d\mu^m} P_\ell(\mu), \quad \text{with} \quad P_\ell(\mu) = \frac{1}{2^\ell \ell!} \frac{d^\ell}{d\mu^\ell} (\mu^2 - 1)^\ell, \quad (\text{A.8})$$

where $\mu = \cos \theta$ and $P_\ell(\mu)$ are the Legendre polynomials with ℓ a non negative integer. With such definition, the associated Legendre functions follows the orthogonality relation

$$\int_{-1}^1 P_\ell^m(\mu) P_{\ell'}^m(\mu) d\mu = \frac{2\delta_{\ell,\ell'}}{2\ell + 1} \frac{(\ell + m)!}{(\ell - m)!}. \quad (\text{A.9})$$

It was shown in Section 1.2.2 that a plane wave can be written as a linear combination of the VSH with only $m = 1$, which lead to the definition of the angular functions π_ℓ and τ_ℓ given by

$$\pi_\ell(\cos \theta) = \frac{P_\ell^1(\cos \theta)}{\sin \theta}, \quad \text{and} \quad \tau_\ell(\cos \theta) = \frac{dP_\ell^1(\cos \theta)}{d\theta},$$

that can be calculated recursively with Eq. (A.8) and the recurrence relations of the Legendre polynomials

$$(2\ell - 1)\mu P_{\ell-1}(\mu) = (\ell - 1)P_\ell(\mu) + \ell P_{\ell-2}(\mu), \quad (\text{A.10})$$

$$(1 - \mu)^2 \frac{dP_\ell(\mu)}{d\mu} = \ell P_{\ell-1}(\mu) - \ell \mu P_\ell(\mu), \quad (\text{A.11})$$

leading to

$$\pi_\ell(\mu) = \frac{2\ell - 1}{\ell - 1} \mu \pi_{\ell-1}(\mu) - \frac{\ell}{\ell - 1} \pi_{\ell-2}, \quad (\text{A.12})$$

$$\tau_\ell(\mu) = \ell\mu\pi_\ell(\mu) - (\ell+1)\pi_{\ell-2}(\mu), \quad (\text{A.13})$$

where $\pi_1(\mu) = 1$ according to Eq. (A.8) and where $\pi_0(\mu) = 0$ is defined. Another result from Eq. (A.8) is that the angular functions $\pi_\ell(\mu)$ and $\tau_\ell(\mu)$, when evaluated at $\theta = 0$ ($\mu = 1$), follows

$$\pi_\ell(\mu = 1) = \frac{dP_\ell(\mu)}{d\mu} \Big|_{\mu=1}, \quad (\text{A.14})$$

$$\tau_\ell(\mu = 1) = \left[\frac{dP_\ell^1(\mu)}{d\mu} + (1 - \mu^2)^{1/2} \frac{d^2P_\ell(\mu)}{d\mu^2} \right] \Big|_{\mu=1} = \frac{dP_\ell(\mu)}{d\mu} \Big|_{\mu=1}, \quad (\text{A.15})$$

which can be obtained from the Legendre equation by setting $m = 1$ and $\mu = 1$ in Eq. (1.19), leading to

$$\pi_\ell(\mu = 1) = \tau_\ell(\mu = 1) = \frac{\ell(\ell+1)}{2} P_\ell(\mu = 1) = \frac{\ell(\ell+1)}{2}, \quad (\text{A.16})$$

where the last equality arises from the chosen definition of the Legendre polynomials [Eq. (A.8)].

The angular functions π_ℓ and τ_ℓ are not orthogonal in general, nevertheless $\pi_\ell(\mu) \pm \tau_\ell(\mu)$ are. To prove the orthogonality of $\pi_\ell \pm \tau_\ell$ let us apply the Legendre equation [Eq. (1.17)] to P_ℓ^m and multiply it by $P_{\ell'}^m$; repeating this procedure inverting ℓ and ℓ' and adding both equations it is obtained that

$$\begin{aligned} & \frac{d}{d\theta} \left(\sin \theta P_{\ell'}^m(\mu) \frac{dP_\ell^m(\mu)}{d\theta} \right) + \frac{d}{d\theta} \left(\sin \theta P_\ell^m(\mu) \frac{dP_{\ell'}^m(\mu)}{d\theta} \right) + \\ & [\ell(\ell+1) + \ell'(\ell'+1)] P_{\ell'}^m(\mu) P_\ell^m(\mu) \sin \theta = 2 \left(\frac{mP_\ell^m(\mu)}{\sin \theta} \frac{mP_{\ell'}^m(\mu)}{\sin \theta} + \frac{dP_\ell^m(\mu)}{d\theta} \frac{dP_{\ell'}^m(\mu)}{d\theta} \right) \sin \theta, \end{aligned} \quad (\text{A.17})$$

where it was added $2 dP_\ell^m/d\theta dP_{\ell'}^m/d\theta$ on both sides to complete the derivatives. Integrating Eq. (A.17) in the interval $\theta \in (0, \pi)$, or $\mu \in (-1, 1)$, and employing Eqs. (A.8) and (A.9), one obtains that

$$\int_{-1}^1 \left(\frac{mP_\ell^m(\mu)}{\sin \theta} \frac{mP_{\ell'}^m(\mu)}{\sin \theta} + \frac{dP_\ell^m(\mu)}{d\theta} \frac{dP_{\ell'}^m(\mu)}{d\theta} \right) d\mu = \delta_{\ell,\ell'} \frac{2\ell(\ell+1)}{2\ell+1} \frac{(\ell+m)!}{(\ell-m)!}. \quad (\text{A.18})$$

Additionally

$$\int_{-1}^1 \frac{mP_\ell^m(\mu)}{\sin \theta} \frac{dP_{\ell'}^m(\mu)}{d\theta} d\mu = \int_0^\pi mP_\ell^m(\mu) \frac{dP_{\ell'}^m(\mu)}{d\theta} d\theta = - \int_{-1}^1 \frac{mP_{\ell'}^m(\mu)}{\sin \theta} \frac{dP_\ell^m(\mu)}{d\theta} d\mu, \quad (\text{A.19})$$

where Eq. (A.8) was employed along integration by parts. Thus, combining Eqs. (A.18) and (A.19), it leads to

$$\int_{-1}^1 \left(\frac{mP_\ell^m(\mu)}{\sin \theta} \pm \frac{dP_\ell^m(\mu)}{d\theta} \right) \left(\frac{mP_{\ell'}^m(\mu)}{\sin \theta} \pm \frac{dP_{\ell'}^m(\mu)}{d\theta} \right) d\mu = \delta_{\ell,\ell'} \frac{2\ell(\ell+1)}{2\ell+1} \frac{(\ell+m)!}{(\ell-m)!}. \quad (\text{A.20})$$

The Eq. (A.20) is the orthogonality of $\pi_\ell(\mu) \pm \tau_\ell(\mu)$ when $m = 1$, which also simplifies the right hand side to $\delta_{\ell,\ell'} 2\ell^2(l+1)^2/(2\ell+1)$.

Vector Spherical Harmonics Orthogonality Relations

The VSH follow orthogonality relations inherited from the orthogonality of sine, cosine and the associated Legendre functions. Let us define the inner product as the integral in the solid angle between two vector functions as

$$\langle \mathbf{A}, \mathbf{A}' \rangle_{\Omega} = \int_0^{2\pi} \int_0^{\pi} \mathbf{A} \cdot \mathbf{A}' \sin \theta d\theta d\varphi. \quad (\text{A.21})$$

Under this inner product, all even VSH are orthogonal to the odd VSH, as well as all VSH with $m \neq m'$, due to the orthogonality of $\sin(m\varphi)$ and $\cos(m'\varphi)$. The remaining orthogonality relations can be obtained by employing Eq. (A.18), leading to

$$\begin{aligned} \langle \mathbf{L}_{em'\ell}, \mathbf{L}_{em'\ell'} \rangle_{\Omega} &= \langle \mathbf{L}_{om\ell}, \mathbf{L}_{om\ell'} \rangle_{\Omega} \\ &= \delta_{m,m'} \delta_{\ell,\ell'} (1 \pm \delta_{m,0}) \frac{2\pi}{2\ell+1} \frac{(\ell+m)!}{(\ell-m)!} \left[\left(k \frac{dz_{\ell}(kr)}{d(kr)} \right)^2 + \ell(\ell+1) \left(k \frac{z_{\ell}(kr)}{kr} \right)^2 \right], \end{aligned} \quad (\text{A.22})$$

$$\begin{aligned} \langle \mathbf{M}_{em\ell}, \mathbf{M}_{em\ell'} \rangle_{\Omega} &= \langle \mathbf{M}_{om\ell}, \mathbf{M}_{om\ell'} \rangle_{\Omega} \\ &= \delta_{m,m'} \delta_{\ell,\ell'} (1 \pm \delta_{m,0}) \pi \frac{2\ell(\ell+1)}{2\ell+1} \frac{(\ell+m)!}{(\ell-m)!} z_{\ell}^2(kr), \end{aligned} \quad (\text{A.23})$$

$$\begin{aligned} \langle \mathbf{N}_{em\ell}, \mathbf{N}_{em\ell'} \rangle_{\Omega} &= \langle \mathbf{N}_{om\ell}, \mathbf{N}_{om\ell'} \rangle_{\Omega} \\ &= \delta_{m,m'} \delta_{\ell,\ell'} (1 \pm \delta_{m,0}) \pi \frac{2\ell(\ell+1)}{2\ell+1} \frac{(\ell+m)!}{(\ell-m)!} \left[\left(\frac{z_{\ell}}{kr} \right)^2 + \left(\frac{1}{kr} \frac{d[krz_{\ell}(kr)]}{d(kr)} \right)^2 \right], \end{aligned} \quad (\text{A.24})$$

$$\begin{aligned} \langle \mathbf{L}_{em\ell}, \mathbf{N}_{em\ell'} \rangle_{\Omega} &= \langle \mathbf{L}_{om\ell}, \mathbf{N}_{om\ell'} \rangle_{\Omega} \\ &= \delta_{m,m'} \delta_{\ell,\ell'} (1 \pm \delta_{m,0}) \pi \frac{2\ell(\ell+1)}{2\ell+1} \frac{(\ell+m)!}{(\ell-m)!} \left[\frac{z_{\ell}}{kr} \frac{dz_{\ell}(kr)}{d(kr)} + \left(\frac{1}{kr} \frac{d[krz_{\ell}(kr)]}{d(kr)} \right)^2 \right], \end{aligned} \quad (\text{A.25})$$

where $(1 + \delta_{m,0})$ is for odd VSH and $(1 - \delta_{m,0})$ for even VSH. The orthogonality relations of the VSH can be further simplified by means of the recurrence relations of the spherical Bessel/Hankel functions [Eqs. (A.3) and (A.4)], which imply that

$$\left[\left(k \frac{dz_{\ell}(kr)}{d(kr)} \right)^2 + \ell(\ell+1) \left(k \frac{z_{\ell}(kr)}{kr} \right)^2 \right] = k^2 [\ell z_{\ell-1}^2(kr) + \ell(\ell+1) z_{\ell+1}^2(kr)], \quad (\text{A.26})$$

$$\left[\left(\frac{z_{\ell}}{kr} \right)^2 + \left(\frac{1}{kr} \frac{d[krz_{\ell}(kr)]}{d(kr)} \right)^2 \right] = \ell(\ell+1) [(\ell+1) z_{\ell-1}^2(kr) + \ell z_{\ell+1}^2(kr)], \quad (\text{A.27})$$

$$\left[\frac{z_{\ell}}{kr} \frac{dz_{\ell}(kr)}{d(kr)} + \left(\frac{1}{kr} \frac{d[krz_{\ell}(kr)]}{d(kr)} \right)^2 \right] = \ell(\ell+1) [z_{\ell-1}^2(kr) - z_{\ell+1}^2(kr)]. \quad (\text{A.28})$$

Appendix B

Size Correction to the Dielectric Function

In this work, the optical properties of spherical gold (Au) nanoparticles (NPs) with radius $a = 12.5$ nm were studied. Even though the optical response of a non magnetic material is encoded in the dielectric function $\varepsilon(\omega)$, the dielectric function for materials at the nanoscale differs from those in bulk due to surface effects. To perform a size correction to the dielectric function, let us decompose it into two additive contributions arising from intra- and interband electronic transitions [32]. If no spatial dispersion is considered, the intraband contribution of the dielectric function can be described by means of the Drude-Sommerfeld model

$$\frac{\varepsilon_{\text{Drude}}(\omega)}{\varepsilon_0} = 1 - \frac{\omega_p^2}{\omega(\omega + i\gamma)}, \quad (\text{B.1})$$

where ε_0 is the vacuum permittivity, and ω_p is the plasma frequency and γ the damping constant. In general, the damping constant is inversely proportional to the average time between collision events of the electrons inside the material and its value depends on the material itself and on its the geometry and dimensions. For example, the damping constant for a material in bulk γ^{Bulk} equals v_F/L with v_F the Fermi velocity and L the mean free path of the electrons. On the other hand, the damping constant γ_a^{NP} for a spherical NP of radius a deviates from γ^{Bulk} if the mean free path is greater than the size of the NP ($L > 2a$). In this case, an effective mean free path replaces L , leading to the following expression for the damping constant:

$$\gamma_a^{\text{NP}} = \gamma^{\text{Bulk}} + A \frac{v_F}{a}, \quad \text{with} \quad \gamma^{\text{Bulk}} = \frac{v_F}{L}, \quad (\text{B.2})$$

where A is a theory dependent parameter whose exact value changes according to the approach employed to calculate the effective mean free path; for this work it is considered that $A = 1$.

In practice, the experimental data for the dielectric function of a material $\varepsilon_{\text{Exp}}(\omega)$ corresponds to a material in bulk, so a size correction is needed for $\varepsilon_{\text{Exp}}(\omega)$ if the optical properties of NPs are studied. The size correction is done by subtracting the intraband contribution that best fits the experimental bulk data and adding an intraband contribution considering Eq. (B.2), that is, the size corrected dielectric function $\varepsilon_{\text{Size}}(\omega)$ is given by

$$\frac{\varepsilon_{\text{Size}}(\omega)}{\varepsilon_0} = \frac{\varepsilon_{\text{Exp}}(\omega)}{\varepsilon_0} + \left(-\frac{\varepsilon_{\text{Drude}}(\omega)}{\varepsilon_0} \Big|_{\gamma=\gamma^{\text{Bulk}}} + \frac{\varepsilon_{\text{Drude}}(\omega)}{\varepsilon_0} \Big|_{\gamma=\gamma_a^{\text{NP}}} \right). \quad (\text{B.3})$$

B. SIZE CORRECTION TO THE DIELECTRIC FUNCTION

The size correction in Eq. (B.3) considers the size effects on the intraband contribution of the dielectric function while the size corrections due to the interband contributions are neglected since it has been reported that they are relevant for NPs with radii smaller than 2 nm [56].

To use the size corrected dielectric function [Eq. (B.3)], the parameters ω_p and γ^{Bulk} that best fit $\varepsilon_{\text{Exp}}(\omega)$ are needed. Let us develop two linear relations involving ω_p and γ^{Bulk} and the real and imaginary parts of $\varepsilon_{\text{Drude}}(\omega)$ following the method from Mendoza Herrera, Arboleda, Schinca, and Scaffardi [56]. The real and imaginary parts of $\varepsilon_{\text{Drude}}(\omega)$ are

$$\text{Re} \left[\frac{\varepsilon_{\text{Drude}}(\omega)}{\varepsilon_0} \right] = 1 - \frac{\omega_p^2 \omega^2}{\omega^4 + (\omega \gamma)^2}, \quad \text{and} \quad \text{Im} \left[\frac{\varepsilon_{\text{Drude}}(\omega)}{\varepsilon_0} \right] = \frac{\omega_p^2 (\omega \gamma)}{\omega^4 + (\omega \gamma)^2}, \quad (\text{B.4})$$

according to Eq. (B.1). By multiplying the imaginary part of $\varepsilon_{\text{Drude}}(\omega)$ by ω and comparing it with its real part, one obtains that

$$\omega \text{Im} \left[\frac{\varepsilon_{\text{Drude}}(\omega)}{\varepsilon_0} \right] = \gamma \left(1 - \text{Re} \left[\frac{\varepsilon_{\text{Drude}}(\omega)}{\varepsilon_0} \right] \right), \quad (\text{B.5})$$

and in a similar manner it can be verified that

$$\omega^2 \left\{ \text{Im} \left[\frac{\varepsilon_{\text{Drude}}(\omega)}{\varepsilon_0} \right]^2 + \left(1 - \text{Re} \left[\frac{\varepsilon_{\text{Drude}}(\omega)}{\varepsilon_0} \right] \right)^2 \right\} = \omega_p^2 \left(1 - \text{Re} \left[\frac{\varepsilon_{\text{Drude}}(\omega)}{\varepsilon_0} \right] \right). \quad (\text{B.6})$$

By plotting the left hand side of Eqs. (B.5) and (B.6) as a function of $1 - \text{Re}[\varepsilon_{\text{Drude}}(\omega)/\varepsilon_0]$ and fitting two linear functions, the values for γ and ω_p^2 can be calculated according to the right hand side of Eqs. (B.5) and (B.6), respectively. As a final remark, the experimental dielectric function includes both an intra- and an interband contribution while Eqs. (B.5) and (B.6) are only valid for the intraband contribution of the dielectric function, thus the linear fits should be done within a spectral window into which the interband contributions are negligible compared to the Drude-Sommerfeld model, which best describes the optical properties of a material when $\omega \rightarrow 0$. The choice of the spectral window for the experimental data fit of the dielectric function modifies the calculated values of γ and ω_p .

In Fig. B.1, the left hand side of Eqs. (B.5) and (B.6) are plotted in orange and black, respectively, as a function of $1 - \text{Re}[\varepsilon(\omega)/\varepsilon_0]$, where $\varepsilon(\omega)$ corresponds to the experimental data of the dielectric function of Au (markers) reported by Johnson and Christy [31]; to ease the read of Fig. B.1, continuous lines between the data were added as a guide to the eye and the photon energy $\hbar\omega$ of selected points of the experimental data are shown on the top margin. The shaded region in Fig. B.1 is the frequency window $0.64 \text{ eV} < \hbar\omega < 1.76 \text{ eV}$, where the experimental data for Au shows a linear behavior as stated by Eqs. (B.5) and (B.6), that is, within this interval the intraband contribution to the dielectric function is dominant, thus the linear fits (dashed lines) were made with the data in this region, determining a plasma frequency of $\hbar\omega_p = (8.70 \pm 0.08) \text{ eV}$ and a damping constant of $\hbar\gamma = (8.29 \pm 0.14) \times 10^{-2} \text{ eV}$ for Au in bulk. Once the plasma frequency and the damping constant for Au have been obtained, the size corrected dielectric for spheres can be calculated.

The real part (blue) and imaginary part (red) of the size corrected dielectric function for Au, based in the experimental data from Johnson and Christy [31], is plotted in Fig. B.2 as a

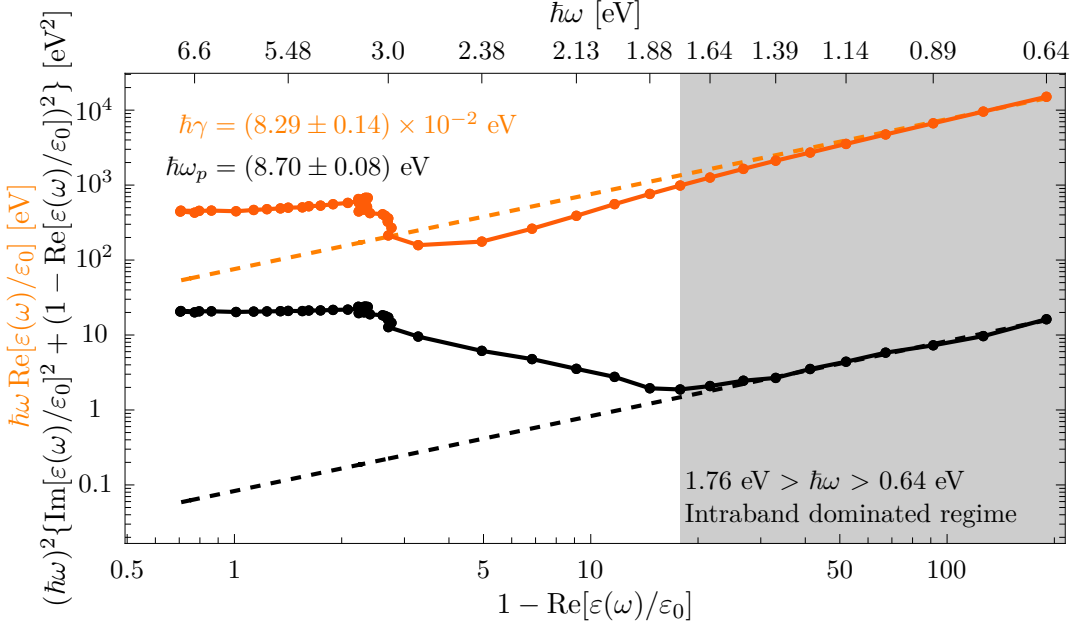


Fig. B.1: Plot of Eqs. (B.5) (orange) and (B.6) (black) evaluated with the experimental dielectric function reported by Johnson and Christy [31]. The shaded region corresponds to the frequency window from 0.64 eV to 1.76 eV, which is best described by the Drude-Sommerfeld model and was considered to perform the linear fits (dashed), determining a plasma frequency of $\hbar\omega_p = (8.70 \pm 0.08)$ eV and a damping constant of $\hbar\gamma = (8.29 \pm 0.14) \times 10^{-2}$ eV for Au.

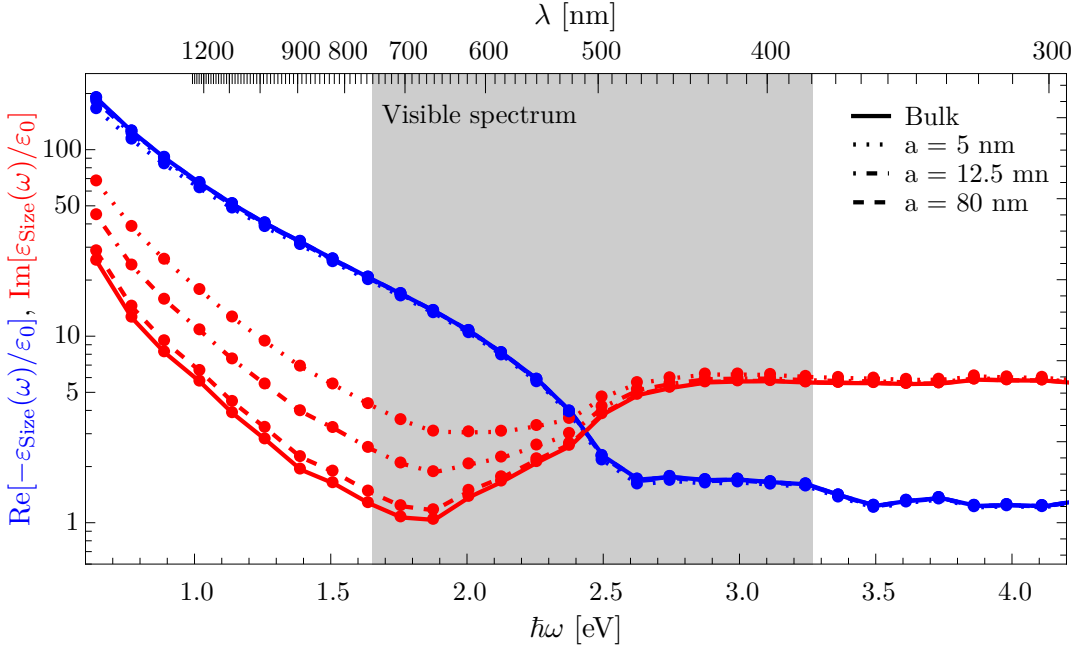


Fig. B.2: Real (blue) and imaginary (red) parts of the size corrected dielectric function of Au in bulk (continuous lines) and of spherical Au NPs of radius 5 nm (dotted lines), 12.5 nm (dash dotted lines) and 80 nm (dashed lines), as a function of the photon energy $\hbar\omega$ (wavelength λ). The size corrected dielectric function was calculated from the experimental data of Johnson and Christy [31].

B. SIZE CORRECTION TO THE DIELECTRIC FUNCTION

function of the photon energy $\hbar\omega$; on the top margin it is shown the conversion of the photon energy into wavelength λ . The size corrected dielectric function was calculated for several cases: Au in bulk (continuous lines) and spherical Au NPs of radius 5 nm (dotted lines), 12.5 nm (dash dotted lines) and 80 nm (dashed lines); all lines are guides to the eye. The data in Fig. B.2 shows that the need for a size corrected dielectric functions increases as the frequency decreases (wavelength increases), specifically for the visible spectrum (shaded region) the size correction is appreciated for $\hbar\omega < 2.5$ eV ($\lambda > 500$ nm). From Fig. B.2 it can also be seen that the imaginary part of the size corrected dielectric function differs the most from the bulk dielectric function compared to its real part, whose deviation from the bulk optical response are barely visible near $\hbar\omega \approx 1$ eV.

Appendix C

Brief COMSOL Implementation of the Scattering Problem

The commercial software COMSOL Multiphysics™ Ver. 5.4 (COMSOL) allows the user to set a desired geometry for solving Eqs. (2.23) as well as the physical properties of each component of the geometry including boundary conditions and the discretization of the system into finite elements. Additionally, once the Eqs. (2.23) are solved, the returned value of the FEM simulation is the total electric field that can be decomposed into an external electric field¹ \mathbf{E}^{ext} , which illuminates the system, and the induced electric field² \mathbf{E}^{ind} , which corresponds to the scattered (internal) electric field if it is evaluated outside (inside) the scatterer. In this Section a brief summary of the implementation of the scattering problem with a planar interface and a spherical scatterer is described for users familiarized with the COMSOL interface, where the desired geometry is the setup presented in Fig. 2.4 in Section 2.3 and the external electric field is an incident electric plane wave and a reflected electric plane wave in the upper half volume of the system and a transmitted electric plane wave in the lower half volume of the system. In order to set up the geometry of the system, the boundary conditions and the physical properties of the system, COMSOL’s *Model Builder* is used.

COMSOL’s Model Builder is the internal tool where the user sets all the parameters for the FEM simulation and it is divided into four categories: Global Definitions, Components, Study and Results. COMSOL allows for several Components and Studies, since they define the Partial Different Equations (PDE) problem to solve, as well as the desired geometry and physical properties of the system. To build the whole system, geometry and physical properties, one must define the general parameters, then the geometry of the system, afterwards the definition of local variables and operators, later the formulation of the PDE and the external electric field, then the boundary conditions and, lastly, the meshing of the system.

The Global Definitions allocate the common parameters of any simulation to be performed with its numerical value. Table C.1 shows the parameters to solve Eq. (2.23) considering a spherical scatterer embedded in a matrix conformed by two semiinfinite non-absorbing media forming a planar interface between them. The parameters in Table C.1 include the properties of the incident electric plane wave —its amplitude (E_0), wavelength (`wlength`), traveling direction

¹COMSOL’s name for the external electric field is the *background electric field*.

²COMSOL’s name for the induced electric field is the *relative electric field*.

Table C.1: Global definitions for COMSOL simulation: Parameters

Name	Expression	Description
E_0	1. [V/m]	Incident electric field amplitude
wlength	550. [nm]	Wavelength of incident plane wave
theta_i	0. [deg]	(Polar) angle of incidence
phi	0. [deg]	(Azimuthal) angle of incidence
alpha	0. [deg]	Electric field inclination
E_s	E_0 * cos(alpha)	Electric field amplitude (<i>s</i> pol)
E_p	E_0 * sin(alpha)	Electric field amplitude <i>p</i> pol)
n_i	1.0	Refractive index of the incidence side
n_t	1.5	Refractive index of the transmission side
radius_NP	12.5 [nm]	Radius of the NP
d_matrix	15. * radius_NP / (2 * max(n_i,n_t))	Distance between NP and PML
h_center	radius_NP / 4.	Height of the center of the NP

(`theta_i` and `phi`) and its polarization through `alpha`, a parameters which is 0° for *s* polarization and 90° for *p* polarization—, the physical properties of the spherical scatterer such as its radius (`radius_NP`) and position in the *z*-plane (`h_center`), and the physical properties of the matrices—the refractive indices of the incidence (`n_i`) and transmission (`n_t`) media and its width (`d_matrix`)—.

Once the parameters of Table C.1 are introduced in COMSOL’s Model Builder, the next step is to define the geometry of the system into the Component/Geometry section. The employed geometry consisted in a sphere of radius `radius_NP`, a block of sides equal to `2*d_matrix + radius_NP + wlength/4.` and a layer of `wlength/4.` in all sides—which defines the PML subvolume—, and a working plane of sides `2*d_matrix + radius_NP + wlength/4.`, which corresponds to the planar interface between the two semiinfinite media. All of these elements can be seen in Fig. C.1, where a screenshot of COMSOL’s interface is shown.

After the geometry is built, within section Component/Definitions, several subvolumes can be labeled to simplify future calculations. In Fig. C.1 it can be seen that the volume and surface of the scatterer are explicitly selected and labeled as `NP` and `NP Surface`, respectively. Additionally, the subvolumes corresponding to the `Physical Domain` selection are those where the calculated electric field has physical meaning, while the complement of such subvolume, labeled as `PML Domain` corresponds to the region where the PML is defined. Another selection explicitly made are the subvolumes `Incidence side` and `Transmssion side`, both of which are subvolumes of both `Physical Domain` and `PML Domain`. The last volumes to be defined are the intersection of `Physical Domain` with `Incidence side`, and with `Transmssion side`, labeled as `Physical incidence side` and `Physical transmission side`, respectively.

With the made volume and surface definitions, integral operators can be defined. In particular, it can be seen in Fig. C.1 that the volume integral operator of a scalar quantity is defined as `vol_int`, where the integration volume is `NP` and a surface integral operators in the surface `NP Surface` is defined as `area_int`. Besides integral operators, one can define functions from interpolation of data points, which is the case of the functions `nRe` and `nIm` that correspond to the real and the imaginary parts of the size corrected refractive index of a gold nanoparticle—see Appendix B—. The PML of the system requires to be set in the Component/Definitions section by choosing this option in its menu and applying it to the `PML Domain` subvolume. Lastly,

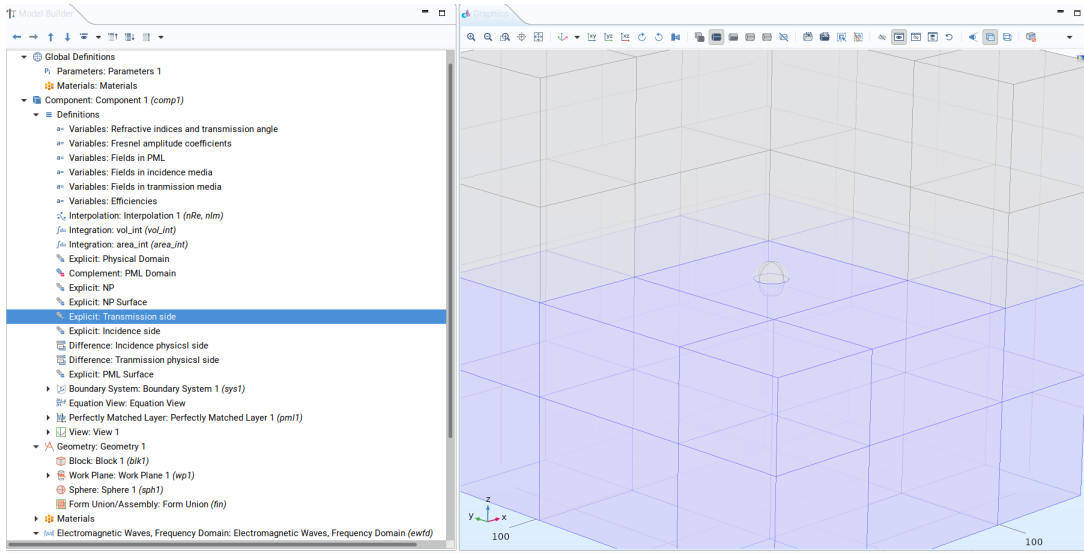


Fig. C.1: Screenshot of a COMSOL Multiphysics™ Ver. 5.4 file showing the Model Builder (left panel) and the Graphics of the built Geometry (right panel). In the Model Builder the Definitions and Geometry sections in Component are expanded to show their contents.

within Component/Definitions one can define local variables into a subvolume or for the whole system; this COMSOL’s function was used to define the external electric field which corresponds to an incident, a reflected and a transmitted electric plane wave. These three contributions were defined piecewise in three subvolumes: **Physical incidence side**, **Physical transmission side** and **PML Domain**. On the one hand, in Table C.2 there are shown the phase of the incident and reflected electric fields, defined as \mathbf{k}_i and \mathbf{k}_r , respectively, as well as their three spatial components — $E_{i,x}$, $E_{i,y}$ and $E_{i,z}$ for the incident plane wave and $E_{r,x}$, $E_{r,y}$ and $E_{r,z}$ for the reflected plane wave—, alongside the Fresnel’s reflection amplitude coefficients for both s (r_s) and p (r_p) polarization. On the other hand, in Table C.3 the three spatial components — $E_{t,x}$, $E_{t,y}$ and $E_{t,z}$ — and the phase — \mathbf{k}_t — of the transmitted electric field are defined, as well as Fresnel’s transmission amplitude coefficients for both s (t_s) and p (t_p) polarization; the component of the incident electric field are all set equal to zero. Additionally, the external electric field is set to zero in the **PML Domain**, as shown in Table C.4.

Before defining the scattering, absorption and extinction cross sections in the Component/Definitions section, one must choose the PDE problem to be solved in the Electromagnetic Waves, Frequency Domain (**ewfd**) and set its formulation in Scattered Field and choose the external electric field, defined piecewise in Tables C.2–C.4, as the sum of the incident, the reflected and the transmitted plane waves. This can be done in the settings panel of **ewfd** as shown in Fig. C.2, where the Scattering formulation allows the user to use the generalized Sommerfeld’s radiation condition [Eq. (2.38)] and to separate the contributions of the total electric field into the external and the induced electric fields, as well as to access to precomputed physical quantities related to the calculated electric field, such as the Poynting vector, for example.

After the Scattering Formulation of the **ewfd** is set, and the external electric field was introduced into COMSOL’s interface, the scattering, absorption and extinction cross sections are defined in the Component/Definitions section as a variable in the whole system. Since the

Table C.2: Local definitions for COMSOL simulation: Component/Definitions/Variables. The below variables are locally defined in the subvolume Physical incidence side.

Name	Expression	Description
k_ir	(2*pi/wlength)*n_i*(x*sin(theta_i)*cos(phi)+y*sin(theta_i)*sin(phi)+z*cos(theta_i))	Incident plane wave phase
k_rr	(2*pi/wlength)*n_i*(x*sin(theta_i)*cos(phi)+y*sin(theta_i)*sin(phi)-z*cos(theta_i))	Reflected plane wave phase
Ei_x	(-E_s*sin(phi)+E_p*cos(theta_i)*cos(phi))*exp(-j*k_ir)	Incident plane wave - x component
Ei_y	(E_s*cos(phi)+E_p*cos(theta_i)*sin(phi))* exp(-j*k_ir)	Incident plane wave - y component
Ei_z	E_p*sin(theta_i)* exp(-j*k_ir)	Incident plane wave - z component
r_s	(n_i*cos(theta_i)-n_t*cos(theta_t))/(n_i*cos(theta_i)+n_t*cos(theta_t))	S reflection amplitude coefficient
r_p	(n_t*cos(theta_i)-n_i*cos(theta_t))/(n_t*cos(theta_i)+n_i*cos(theta_t))	P reflection amplitude coefficient
Ert_x	(-E_s*sin(phi)*r_s - E_p*cos(theta_i)*cos(phi)*r_p)* exp(-j*k_rr)	Reflected plane wave - x component
Ert_y	(E_s*cos(phi)*r_s - E_p*cos(theta_i)*sin(phi)*r_p)* exp(-j*k_rr)	Reflected plane wave - y component
Ert_z	E_p*sin(theta_i)*r_p * exp(-j*k_rr)	Reflected plane wave - z component

Table C.3: Local definitions for COMSOL simulation: Component/Definitions/Variables. The below variables are locally defined in the subvolume Physical transmission side.

Name	Expression	Description
k_tr	(2*pi/wlength)*n_t*(x*sin(theta_t)*cos(phi)+y*sin(theta_t)*sin(phi)+z*cos(theta_t))	Transmitted plane wave phase
Ei_x	0.	Incident plane wave - x component
Ei_y	0.	Incident plane wave - y component
Ei_z	0.	Incident plane wave - z component
t_s	2*n_i*cos(theta_i)/(n_i*cos(theta_i)+n_t*cos(theta_t))	S amplitude transmission coefficient
t_p	2*n_i*cos(theta_i)/(n_t*cos(theta_i)+n_i*cos(theta_t))	P amplitude transmission coefficient
Ert_x	(-E_s*sin(phi)*t_s - E_p*cos(theta_t)*cos(phi)*t_p)* exp(-j*k_tr)	Transmitted plane wave - x component
Ert_y	(E_s*cos(phi)*t_s - E_p*cos(theta_t)*sin(phi)*t_p)* exp(-j*k_tr)	Transmitted plane wave - y component
Ert_z	E_p*sin(theta_i)*t_p * exp(-j*k_tr)	Transmitted plane wave - z component

Table C.4: Local definitions for COMSOL simulation: Component/Definitions/Variables. The below variables are locally defined in the subvolume PML Domain.

Name	Expression	Description
Ei_x	0.	Incident electric plane wave - x component
Ei_y	0.	Incident electric plane wave - y component
Ei_z	0.	Incident electric plane wave - z component
Ert_x	0.	(Reflected) Transmitted plane wave - x component
Ert_y	0.	(Reflected) Transmitted plane wave - y component
Ert_z	0.	(Reflected) Transmitted plane wave - z component

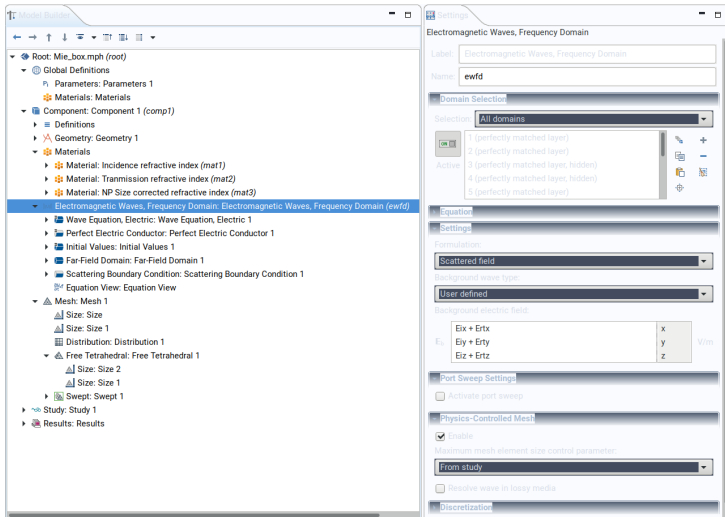


Fig. C.2: Screenshot of a COMSOL Multiphysics™ Ver. 5.4 file showing the Model Builder (left panel) and the settings panel of the Electromagnetic Waves, Frequency Domain —ewfd— (right panel). In the Model Builder the Materials and ewfd sections in Components are expanded to show their content, while in the settings planel in ewfd it is shown that the Scattered Field formulation is set and that the external electric field is a user-defined quantity given by the expressions shown in Tables C.2–C.4.

scattering cross section is calculated by Eq. (1.8), the time-averaged scattering Poynting vector is projected onto the normal vector to a closed surface and then integrated on such surface. The component of the time-averaged scattering Poynting vector are precalculated by COMSOL and are accessed by the user thought the variables `ewfd.relPoavx`, `ewfd.relPoavy` and `ewfd.relPoavz` [49] and the component of the normal vector to any surface are given by `nx`, `ny` and `nz`. By calculating the dot product of the normal vector and the time-averaged scattering Poynting vector, applying to it the integral operator `area_int` and dividing by the irradiance of the incident plane wave `s_i`, the scattering cross section `c_sca` is obtained. For the absorption cross section `c_abs` the Eq. (1.9) is employed, that is the integral operator `vol_int` is applied to the variable `ewfd.Qh`, which are the heat losses calculated by Joule's law [49]; lastly the extinction cross section `c_ext` is calculated as the sum of the scattering and the absorption cross sections. All the needed definitions are shown in Table C.5.

Table C.5: Local definitions for COMSOL simulation: Component/Definitions/Variables. The below variables are locally defined in all domains.

Name	Expression	Description
<code>theta_t</code>	<code>arcsin((n_i/n_t)*sin(theta_i))</code>	Transmission angle
<code>S_i</code>	<code>n_i*E0^2/(2*Z0_const)</code>	Incident Irradiance
<code>S_x</code>	<code>nx * ewfd.relPoavx</code>	Average Poynting Vector in the normal x direction
<code>S_y</code>	<code>ny * ewfd.relPoavy</code>	Average Poynting Vector in the normal y direction
<code>S_z</code>	<code>nz * ewfd.relPoavz</code>	Average Poynting Vector in the normal z direction
<code>C_sca</code>	<code>area_int(S_x + S_y + S_z)/(S_i)</code>	Scattering cross section
<code>C_abs</code>	<code>vol_int(ewfd.Qh)/(S_i)</code>	Absorption cross section
<code>C_ext</code>	<code>C_sca + C_abs</code>	Extinction cross section

The last step before running the FEM simulation in COMSOL is to define the mesh—or the partition into finite elements—of the system. As discussed in Section 2.3, the mesh size can be set for different subvolumes in the system, as also the geometric shape of the finite elements. For this work tetrahedral finite element were chosen for the meshing in the matrix and the spherical scatterer (blue regions in Fig. C.3), where the later had a finer meshing to diminish the absolute error of the obtained approximated solution. This is specified in the Component/Mesh section of the Model Builder by setting two different sizes to each subvolume of interest. Since the PML requires a geometrical transformation to simulate an absorbing media with no reflection, the finite elements in the PML must match the geometrical symmetry of the system to minimize errors [48], which is a rectangular or Cartesian symmetry in the employed geometry, as seen in the gray areas of Fig. C.3. Following the described steps in this section, the geometry and boundary conditions employed in this work can be reproduced. After the system is set up, one can choose any Study and visualize the results in COMSOL’s viewer or export them.

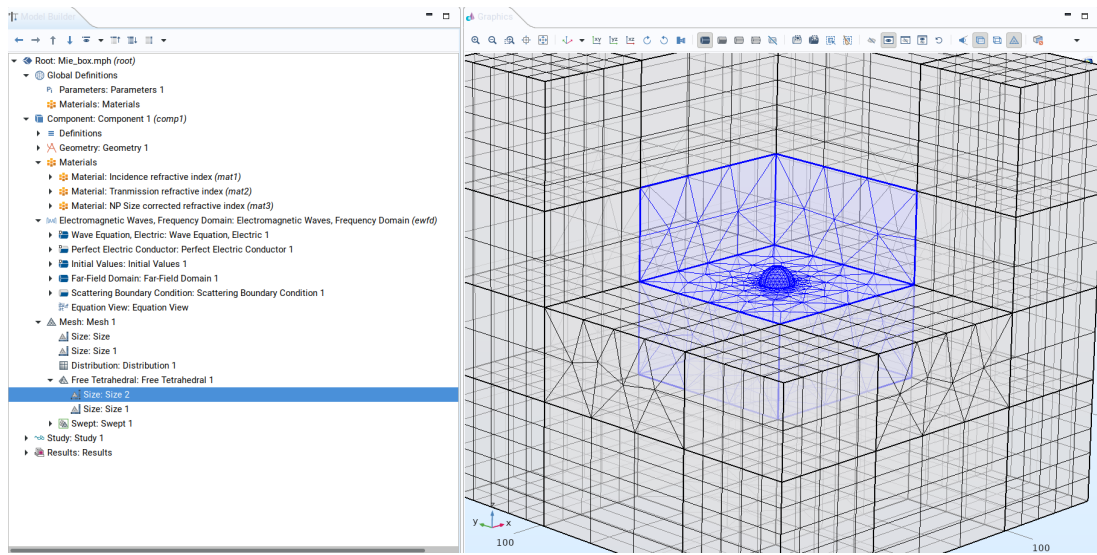


Fig. C.3: Screenshot of a COMSOL Multiphysics™ Ver. 5.4 file showing the Model Builder (left panel) and the Graphics of the built geometry with the chosen mesh (right panel). In the Model Builder the Materials, Electromagnetic Waves, Frequency Domain —ewfd— and Mesh sections in Component are expanded to show their contents.

Bibliography

- [1] S. A. Khan, N. Z. Khan, Y. Xie, M. T. Abbas, M. Rauf, I. Mehmood, M. Runowski, S. Agathopoulos, and J. Zhu. Optical sensing by metamaterials and metasurfaces: from physics to biomolecule detection. *Advanced Optical Materials*, **10**(18):2200500, 2022. DOI: [10.1002/adom.202200500](https://doi.org/10.1002/adom.202200500) (cited on page 1).
- [2] A. K. González-Alcalde and A. Reyes-Coronado. Large angle-independent structural colors based on all-dielectric random metasurfaces. *Optics Communications*, **475**:126289, 2020. DOI: [10.1016/j.optcom.2020.126289](https://doi.org/10.1016/j.optcom.2020.126289) (cited on page 1).
- [3] M. Kim, J. Lee, and J. Nam. Plasmonic photothermal nanoparticles for biomedical applications. *Advanced Science*, **6**(17):1900471, 2019. DOI: [10.1002/advs.201900471](https://doi.org/10.1002/advs.201900471). (Visited on 10/27/2022) (cited on page 1).
- [4] H.-T. Chen, A. J. Taylor, and N. Yu. A review of metasurfaces: physics and applications. *Reports on Progress in Physics*, **79**(7):076401, 2016. DOI: [10.1088/0034-4885/79/7/076401](https://doi.org/10.1088/0034-4885/79/7/076401) (cited on page 1).
- [5] M.-C. Estevez, M. A. Otte, B. Sepulveda, and L. M. Lechuga. Trends and challenges of refractometric nanoplasmonic biosensors: a review. *Analytica Chimica Acta*, **806**:55–73, 2014. DOI: [10.1016/j.aca.2013.10.048](https://doi.org/10.1016/j.aca.2013.10.048) (cited on pages 1, 2).
- [6] P. K. Jain, X. Huang, I. H. El-Sayed, and M. A. El-Sayed. Noble metals on the nanoscale: optical and photothermal properties and some applications in imaging, sensing, biology, and medicine. *Accounts of Chemical Research*, **41**(12):1578–1586, 2008. DOI: [10.1021/ar7002804](https://doi.org/10.1021/ar7002804) (cited on page 1).
- [7] A. V. Kabashin, P. Evans, S. Pastkovsky, W. Hendren, G. A. Wurtz, R. Atkinson, R. Pollard, V. A. Podolskiy, and A. V. Zayats. Plasmonic nanorod metamaterials for biosensing. *Nature Materials*, **8**(11):867–871, 2009. DOI: [10.1038/nmat2546](https://doi.org/10.1038/nmat2546) (cited on pages 1–3).
- [8] L. Feuz, P. Jönsson, M. P. Jonsson, and F. Höök. Improving the limit of detection of nanoscale sensors by directed binding to high-sensitivity areas. *ACS Nano*, **4**(4):2167–2177, 2010. DOI: [10.1021/nn901457f](https://doi.org/10.1021/nn901457f) (cited on pages 1, 2).
- [9] G. Qiu, Z. Gai, Y. Tao, J. Schmitt, G. A. Kullak-Ublick, and J. Wang. Dual-functional plasmonic photothermal biosensors for highly accurate severe acute respiratory syndrome coronavirus 2 detection. *ACS Nano*, **14**(5):5268–5277, 2020. DOI: [10.1021/acsnano.0c02439](https://doi.org/10.1021/acsnano.0c02439) (cited on pages 1, 2).
- [10] M. Svedendahl, R. Verre, and M. Käll. Refractometric biosensing based on optical phase flips in sparse and short-range-ordered nanoplasmonic layers. *Light: Science & Applications*, **3**(11):e220–e220, 2014. DOI: [10.1038/lsa.2014.101](https://doi.org/10.1038/lsa.2014.101) (cited on pages 1–3).

BIBLIOGRAPHY

- [11] X. Meng, T. Shibayama, R. Yu, J. Ishioka, and S. Watanabe. Anisotropic surroundings effects on photo absorption of partially embedded au nanospheroids in silica glass substrate. *AIP Adv.*, **5**(2):027112, 2015. DOI: [10.1063/1.4908010](https://doi.org/10.1063/1.4908010) (cited on pages 2, 3, 50, 54, 61).
- [12] G. Qiu, S. P. Ng, and C. M. L. Wu. Differential phase-detecting localized surface plasmon resonance sensor with self-assembly gold nano-islands. *Optics Letters*, **40**(9):1924, 2015. DOI: [10.1364/OL.40.001924](https://doi.org/10.1364/OL.40.001924) (cited on pages 2, 3).
- [13] D. Bedeaux and J. Vlieger. *Optical properties of surfaces*. Imperial College Press, London, 2nd edition, 2004. 450 pages. ISBN: 978-1-86094-450-5 (cited on pages 2, 3, 61, 81).
- [14] R. G. Barrera, M. del Castillo-Mussot, G. Monsivais, P. Villaseor, and W. L. Mochán. Optical properties of two-dimensional disordered systems on a substrate. *Phys. Rev. B*, **43**(17):13819–13826, 1991. DOI: [10.1103/PhysRevB.43.13819](https://doi.org/10.1103/PhysRevB.43.13819) (cited on pages 2, 3, 50, 61, 81).
- [15] A. Sihvola. *Electromagnetic Mixing Formulas and Applications*. Electronic Waves. The Institution of Engineering and Technology, 2008. ISBN: 978-0-85296-772-0 (cited on pages 2, 61, 81).
- [16] T. Oates, H. Wormeester, and H. Arwin. Characterization of plasmonic effects in thin films and metamaterials using spectroscopic ellipsometry. *Progress in Surface Science*, **86**(11):328–376, 2011. DOI: [10.1016/j.progsurf.2011.08.004](https://doi.org/10.1016/j.progsurf.2011.08.004) (cited on page 2).
- [17] R. S. Moirangthem, M. T. Yaseen, P.-K. Wei, J.-Y. Cheng, and Y.-C. Chang. Enhanced localized plasmonic detections using partially-embedded gold nanoparticles and ellipsometric measurements. *Biomedical Optics Express*, **3**(5):899, 2012. DOI: [10.1364/BOE.3.000899](https://doi.org/10.1364/BOE.3.000899) (cited on pages 2, 3, 5, 61).
- [18] G. Mie. Beiträge zur Optik trüber Medien, speziell kolloidaler Metallösungen. *Annalen der Physik*, **330**(3):377–445, 1908. DOI: [10.1002/andp.19083300302](https://doi.org/10.1002/andp.19083300302). Number: 3 (cited on page 5).
- [19] H. Horvath. Gustav Mie and the scattering and absorption of light by particles: Historic developments and basics. *Journal of Quantitative Spectroscopy and Radiative Transfer*, **110**(11):787–799, 2009. DOI: [10.1016/j.jqsrt.2009.02.022](https://doi.org/10.1016/j.jqsrt.2009.02.022). Number: 11 (cited on page 5).
- [20] C. F. Bohren and D. R. Huffman. *Absorption and Scattering of Light by Small Particles*. Wiley Science Paperbak Series. John Wiley & Sons, 1st edition, 1983. ISBN: 0-471-029340-7 (cited on pages 5, 7–11, 13–15, 18, 55).
- [21] L. Tsang, J. A. Kong, and K.-H. Ding. *Scattering of Electromagnetic Waves: Theories and Applications*. John Wiley & Sons, Inc., New York, USA, 2000. ISBN: 978-0-471-22428-0 978-0-471-38799-2. DOI: [10.1002/0471224286](https://doi.org/10.1002/0471224286) (cited on pages 5, 6, 8, 9).
- [22] J. D. Jackson. *Classical electrodynamics*. Wiley, New York, 3rd edition, 1999. ISBN: 978-0-471-30932-1 (cited on pages 8, 30, 34, 35, 37).
- [23] M. Pellarin, C. Bonnet, J. Lermé, F. Perrier, J. Laverdant, M.-A. Lebeault, S. Hermelin, M. Hillenkamp, M. Broyer, and E. Cottancin. Forward and Backward Extinction Measurements on a Single Supported Nanoparticle: Implications of the Generalized Optical Theorem. *The Journal of Physical Chemistry C*, **123**(24):15217–15229, 2019. DOI: [10.1021/acs.jpcc.9b03245](https://doi.org/10.1021/acs.jpcc.9b03245) (cited on page 8).
- [24] R. G. Newton. Optical theorem and beyond. *American Journal of Physics*, **44**(7):639–642, 1976. DOI: [10.1119/1.10324](https://doi.org/10.1119/1.10324) (cited on pages 8, 9).
- [25] A. V. Krasavin, P. Segovia, R. Dubrovka, N. Olivier, G. A. Wurtz, P. Ginzburg, and A. V. Zayats. Generalization of the optical theorem: experimental proof for radially polarized

BIBLIOGRAPHY

- beams. *Light: Science & Applications*, **7**(1):36, 2018. doi: [10.1038/s41377-018-0025-x](https://doi.org/10.1038/s41377-018-0025-x) (cited on page 9).
- [26] M. Born and W. Emil. *Principle of Optics: Electromagnetic Theory of Propagation, Interference and Diffraction of Light*. Cambridge University Press, New York, USA, 7th edition, 1999. ISBN: 0-521-64222-1 (cited on pages 9, 54, 55).
- [27] A. Zangwill. *Modern Electrodynamics*. Cambridge University Press, Cambridge, 2013. ISBN: 978-0-521-89697-9 (cited on pages 9, 11, 34, 35).
- [28] J. A. Stratton. *Electromagnetic theory*. McGraw-Hill, New York, 2012. ISBN: 978-1-4437-3054-9 (cited on pages 10, 12).
- [29] R. G. Barrera, G. A. Estevez, and J. Giraldo. Vector spherical harmonics and their application to magnetostatics. *European Journal of Physics*, **6**(4):287–294, 1985. doi: [10.1088/0143-0807/6/4/014](https://doi.org/10.1088/0143-0807/6/4/014) (cited on page 12).
- [30] C. Maciel Escudero. *Linear Momentum Transfer from Swift Electrons to Small Metallic Nanoparticles: Dipole Approximation*. Master's thesis, UNAM, Mexico City, Mexico, 2017 (cited on page 18).
- [31] P. B. Johnson and R. W. Christy. Optical Constants of the Noble Metals. *Physical Review B*, **6**(12):4370–4379, 1972. doi: [10.1103/PhysRevB.6.4370](https://doi.org/10.1103/PhysRevB.6.4370) (cited on pages 18–22, 48, 88, 89).
- [32] C. Noguez. Surface Plasmons on Metal Nanoparticles: The Influence of Shape and Physical Environment. *The Journal of Physical Chemistry C*, **111**(10):3806–3819, 2007. doi: [10.1021/jp066539m](https://doi.org/10.1021/jp066539m) (cited on pages 18, 87).
- [33] L. Novotný and B. Hecht. *Principles of nano-optics*. Cambridge Univ. Press, Cambridge, 1st edition, 2011. 539 pages. ISBN: 978-0-521-53988-3 978-0-521-83224-3 (cited on page 19).
- [34] H. Ibach and H. Lüth. *Solid-State Physics*. Springer Berlin Heidelberg, Berlin, Heidelberg, 2009. ISBN: 978-3-540-93803-3 978-3-540-93804-0. doi: [10.1007/978-3-540-93804-0](https://doi.org/10.1007/978-3-540-93804-0) (cited on page 21).
- [35] G. Dhatt, G. Touzot, and E. Lefrançois. *Finite element method*. Numerical methods series. ISTE ; Wiley, London : Hoboken, N.J, 2012. ISBN: 978-1-84821-368-5 (cited on pages 23–29).
- [36] M. G. Larson and F. Bengzon. *The Finite Element Method: Theory, Implementation, and Applications*, volume 10 of *Texts in Computational Science and Engineering*. Springer Berlin Heidelberg, Berlin, Heidelberg, 2013. ISBN: 978-3-642-33286-9 978-3-642-33287-6. doi: [10.1007/978-3-642-33287-6](https://doi.org/10.1007/978-3-642-33287-6) (cited on pages 24, 25, 27–33).
- [37] C. A. J. Fletcher. *Computational Galerkin Methods*. Springer Berlin Heidelberg, Berlin, Heidelberg, 1984. ISBN: 978-3-642-85951-9 978-3-642-85949-6. doi: [10.1007/978-3-642-85949-6](https://doi.org/10.1007/978-3-642-85949-6) (cited on pages 24–29).
- [38] J.-M. Jin. *Theory and Computation of Electromagnetic Fields*. Wiley & Sons, 2010. ISBN: 978-0-470-53359-8 (cited on pages 25, 30–39).
- [39] A. Bondeson, T. Rylander, and P. Ingelström. *Computational electromagnetics*. Springer, New York, N.Y, 2005. ISBN: 978-0-387-26158-4 978-0-387-26160-7 (cited on pages 30–32, 34–36, 38, 39).
- [40] M. Bergot and P. Lacoste. Generation of higher-order polynomial basis of Nédélec $H(\text{curl})$ finite elements for Maxwell's equations. *Journal of Computational and Applied Mathematics*, **234**(6):1937–1944, 2010. doi: [10.1016/j.cam.2009.08.044](https://doi.org/10.1016/j.cam.2009.08.044) (cited on pages 32, 33).
- [41] W. C. Chew, J. M. Jin, and E. Michielssen. Complex coordinate stretching as a generalized absorbing boundary condition. *Microwave and Optical Technology Letters*, **15**(6):363–369,

BIBLIOGRAPHY

1997. DOI: [10.1002/\(SICI\)1098-2760\(19970820\)15:6<363::AID-MOP8>3.0.CO;2-C](https://doi.org/10.1002/(SICI)1098-2760(19970820)15:6<363::AID-MOP8>3.0.CO;2-C) (cited on pages 34, 36–39).
- [42] S. H. Schot. Eighty years of Sommerfeld’s radiation condition. *Historia Mathematica*, **19**(4):385–401, 1992. DOI: [10.1016/0315-0860\(92\)90004-U](https://doi.org/10.1016/0315-0860(92)90004-U) (cited on pages 34, 36).
- [43] J. A. Stratton and L. J. Chu. Diffraction theory of electromagnetic waves. *Physical Review*, **56**(1):99–107, 1939. DOI: [10.1103/PhysRev.56.99](https://doi.org/10.1103/PhysRev.56.99) (cited on pages 34, 51).
- [44] S. Silver. *Microwave Antenna Theory and Design*. The Institution of Engineering and Technology, 1984. 640 pages. ISBN: 978-0-86341-017-8 (cited on pages 34, 36).
- [45] D. Colton and R. Kress. *Inverse Acoustic and Electromagnetic Scattering Theory*, volume 93 of *Applied Mathematical Sciences*. Springer International Publishing, Cham, 2019. ISBN: 978-3-030-30350-1 978-3-030-30351-8. DOI: [10.1007/978-3-030-30351-8](https://doi.org/10.1007/978-3-030-30351-8) (cited on pages 34, 36).
- [46] J.-P. Berenger. A perfectly matched layer for the absorption of electromagnetic waves. *Journal of Computational Physics*, **114**(2):185–200, 1994. DOI: [10.1006/jcph.1994.1159](https://doi.org/10.1006/jcph.1994.1159). (Visited on 06/02/2022) (cited on page 36).
- [47] G. B. Arfken and H.-J. Weber. *Mathematical methods for physicists*. Harcourt/Academic Press, San Diego, 5th edition, 2001. ISBN: 978-0-12-059825-0 (cited on pages 37, 84).
- [48] COMSOL Multiphysics™ Ver. 6.0. *COMSOL Documentation*. <https://doc.comsol.com/>. COMSOL AB. Stockholm, Sweden., 2021 (cited on pages 39–41, 44, 96).
- [49] COMSOL Multiphysics™ Ver. 6.0. *Wave Optics Module User’s Guide*. <https://doc.comsol.com/5.4/doc/com.comsol.help.woptics/WaveOpticsModuleUsersGuide.pdf>. COMSOL AB. Stockholm, Sweden., 2021 (cited on pages 40, 41, 51, 95).
- [50] N. V. Anyutin, K. I. Kurbatov, I. M. Malay, and M. A. Ozerov. Algorithm for transforming antenna electromagnetic near-field measured on spherical surface into far-field based on direct calculation of Stratton and Chu formulas. *Radioelectronics and Communications Systems*, **62**(3):109–118, 2019. DOI: [10.3103/S0735272719030026](https://doi.org/10.3103/S0735272719030026) (cited on page 51).
- [51] D. J. Griffiths. *Introduction to electrodynamics*. Pearson, 4th edition, 2013 (cited on page 58).
- [52] H. C. v. d. Hulst. *Light scattering by small particles*. Dover Publications, New York, 1981. 470 pages. ISBN: 978-0-486-64228-4 (cited on page 61).
- [53] A. García-Valenzuela, E. Gutiérrez-Reyes, and R. G. Barrera. Multiple-scattering model for the coherent reflection and transmission of light from a disordered monolayer of particles. *JOSA A*, **29**(6):1161–1179, 2012. DOI: <https://doi.org/10.1364/JOSAA.29.001161> (cited on page 61).
- [54] A. Reyes-Coronado, G. Pirruccio, A. K. González-Alcalde, J. A. Urrutia-Anguiano, A. J. Polanco-Mendoza, G. Morales-Luna, O. Vázquez-Estrada, A. Rodríguez-Gómez, A. Issa, S. Jradi, et al. Enhancement of light absorption by leaky modes in a random plasmonic metasurface. *The Journal of Physical Chemistry C*, **126**(6):3163–3170, 2022. DOI: <https://doi.org/10.1021/acs.jpcc.1c08325> (cited on page 61).
- [55] M. Abramowitz and I. A. Stegun. *Handbook of mathematical functions: with formulas, graphs, and mathematical tables*. Dover, New York, NY, 9th edition, 2013. 1046 pages. ISBN: 978-0-486-61272-0 (cited on page 83).
- [56] L. J. Mendoza Herrera, D. M. Arboleda, D. C. Schinca, and L. B. Sccaffardi. Determination of plasma frequency, damping constant, and size distribution from the complex dielectric function of noble metal nanoparticles. *Journal of Applied Physics*, **116**(23):233105, 2014. DOI: [10.1063/1.4904349](https://doi.org/10.1063/1.4904349) (cited on page 88).

Index

- Absorption
 - Cross Section, 8, 20
- Approximation
 - Finite Element, 26
 - Nodal, 25
 - Vectorial, 32
- Bessel
 - Spherical Functions $j_\ell(\rho)$ and $y_\ell(\rho)$, 11, 83
- Boundary Conditions
 - Absorbing, 34
 - Maxwell Eigenvalue Problem, 31
 - Mie Problem, 12
 - Open, 34
 - Perfectly Matching Layer (PML), 36
 - Sommerfeld's Radiation Condition, 34
- Coordinate System
 - Relative to Scattering Plane, 6
 - Stretched, 37
- Cross Section
 - Scattering C_{abs} , 8, 20
 - Extinction, 8, 20
 - Scattering C_{sca} , 7
- Dipole
 - Image
 - Strength, 50
- Extinction
 - Cross Section, 8, 20
- Faraday-Lenz's Law, 6
- Finite Element
- Approximation, 26
- Definition of, 26
- Lagrange, 28
- Linear Functional, 26
 - Hermite, 28
 - Lagrange, 28
 - Nédélec, 32
- Method, 24
 - Interpolating Function ϕ , 25
 - Trial Function ψ , 24
- Order, 27
 - Real-space, 27
 - Reference, 27
- Functions
 - Interpolating η , 32
 - Interpolating ϕ , 25
 - Lagrange, 28, 32
- Legendre Associated, 11, 84
- Spherical Bessel $j_\ell(\rho)$ and $y_\ell(\rho)$, 11, 83
- Spherical Hankel $h_\ell^{(1)}(\rho)$ and $h_\ell^{(2)}(\rho)$, 11, 83
 - Asymptotic Limit, 11, 15
- Trial ψ , 24
- Gauge
 - Lorenz, 35
- Gauss
 - Theorem, 24
- Green
 - First Identity, 24
 - Function
 - to Scalar Helmholtz Equation, 34
 - Second Identity, 34
- Hankel

INDEX

- Spherical Functions $h_\ell^{(1)}(\rho)$ and $h_\ell^{(2)}(\rho)$, 11, 83
Asymptotic Limit, 11
- Helmholtz
Equation
Scalar, 10
Vectorial, 9, 30
- Joule
Heating Law, 8
- Law
Faraday-Lenz's, 6
Joule Heating, 8
Ohm, 8
- Legendre
Associated Functions $P_\ell^m(\mu)$, 11, 84
- Lorenz
Gauge, 35
- Maxwell Equations
Harmonic Time Dependent, 30
Electric and Magnetic Contributions, 35
Stretched Coordinate System, 38
- Method
Finite Element, 24, 26
Galerkin, 25
Weighted Residual, 25
- Ohm
Law, 8
- Optical
Theorem, 8, 20
- Partial Differential Equation (PDE)
Boundary Conditions, 23
Absorbing, 34
Open, 34
Maxwell Eigenvalue Problem
Strong Formulation, 31
Weak Formulation, 31
Nodal Approximation, 25
Interpolating Function ϕ , 25
Vectorial, 32
Strong Formulation, 23
Trial Function ψ , 24
- Plane
Scattering
- Coordinate System, 6
Wave, 5
Irradiance, 7
- Plasmon
Localized Surface Plasmon Resonance (LSPR), 5
- Scattering
Amplitude Matrix \mathbb{F} , 6
for Spherical Particles, 15
Cross Section, 7
Mie, 9
Angular Functions π and τ , 13, 84
Angular Functions π_ℓ and τ_ℓ , 84
Coefficients, 13, 14
- Pattern, 22
- Plane
Coordinate System, 6
Unit Vector System, 6
- Problem
Strong Formulation, 31
Weak Formulation, 31
Rayleigh, 9
Thompson, 9
- Sommerfeld
Radiation Condition
Scalar, 34
Vectorial, 36
- Theorem
Gauss', 24
Optical, 8, 20
- Vector
Spherical Harmonics, 9
Generating Function ψ , 10, 11
Orthogonality, 86
Spherical Coordinates, 11
Spherical Harmonics $\{\mathbf{L}^{(1)}, \mathbf{M}^{(1)}, \mathbf{N}^{(1)}\}$, 11
Spherical Harmonics $\{\mathbf{L}^{(3)}, \mathbf{M}^{(3)}, \mathbf{N}^{(3)}\}$, 11
Averaged Poynting $\langle \mathbf{S} \rangle_t$, 6
- Wave
Plane, 5, 11
Dispersion Relation, 36
Spherical, 11, 15